THESIS FOR THE DEGREE OF DOCTOR OF PHILOSOPHY

Steady state analysis of HVDC grid with wind power plants

Kalid Yunus

Department of Energy and Environment
Division of Electric Power Engineering
CHALMERS UNIVERSITY OF TECHNOLOGY
Göteborg, Sweden 2017

Steady state analysis of HVDC grid with wind power plants
KALID YUNUS
ISBN: 978-91-7597-536-8

KALID YUNUS

Doktorsavhandlingar vid Chalmers Tekniska Hogskola
Ny serrie nr 4217
ISSN 0346-718X

Department of Energy and Environment
Division of Electric Power Engineering
SE-412 96 Göteborg
Sweden
Telephone +46(0)31-772 1000

Chalmers Bibliotek, Reproservice
Göteborg, Sweden 2017

Alhamdulillah!

Steady state analysis of HVDC grid with wind power plants
KALID YUNUS
Department of Energy and Environment
Chalmers University of Technology

Abstract

The idea of building a multi-terminal, even a meshed HVDC grid in the North Sea, that can inter-connect surrounding nations, is being discussed widely. Such a system is expected to be realised in steps through the interconnection of wind power plants and electricity markets. Hence, the aim of this work is to accomplish steps to realise the idea through modelling, investigating and quantifying economical and the technical aspects of building the grid. Particular attention is placed on quantifying economically optimum sizing of system components and establishing economic connection requirements of the markets.

In order to fulfil part of the aim, wind speed modelling procedures, that can be used to simulate temporally and specially correlated time series wind speed, are proposed. A special contribution in one of the modelling procedures is the introduction of frequency decomposition in the procedure. The procedures are later used as inputs to simulate time series wind power which is used in the economical analysis of building the grid in steps. In addition, a steady state model of a control strategy, which is based on local primary controllers and a central secondary controller, is also presented.

Moreover, based on the investigated cases, it is verified that the optimum size of a VSC HVDC transmission system, connecting two electricity markets having a pre-defined exchange power data, is approximately equal to the absolute mean of the exchange. The result is determined for a cable length of 300 km and the optimum cable size decreases by about 5% for every 300 km increases in cable length. Furthermore, it is quantified that the investment cost of a VSC HVDC transmission system is 3 €/MWh for a cable length of 300 km. For every 300 km increase in cable length, the investment cost increases by about 2 €/MWh.

Furthermore, a minimum slope difference requirement, between the marginal costs of markets, for an economical inter-connection, is established. The established requirement focuses on the cases where the net exchange power between the markets, during some time interval, is close to zero. Based on the studied cases, it is determined that, for a given distance between the markets, the minimum slope difference, that could make a feasible investment, decays exponentially as the size of the system increases. For example, for two markets which are 300 km apart and have a maximum demand of 20 GW each, the minimum angle between the markets should be 0.006. For 100% increase in cable length, the minimum angle also increases by the same percentage.

Index Terms: meshed HVDC grid, VSC HVDC, WPP, temporal and spatial correlation, wind speed modelling, electricity market, LRMC, SRMC, transmission tariff, electricity price, investment cost, primary controller, secondary/supervisory controller, ARIMA, PV.

Acknowledgements

This work was carried out at Chalmers University of Technology, Department of Energy and Environment, Electric Power Engineering Division. The financial support, provided by the Swedish Energy Agency (Energimyndigheten), is gratefully appreciated. My special thanks go to my main supervisor Prof. Torbjörn Thiringer for his immense support, critical comments and revising the thesis manuscript extensively at every stage to make it as awesome as it looks. I would also like to thank Prof. Thiringer for helping me all the way from master thesis to my PhD study, thank so much Torbjörn. I would also like to thank my examiner Prof. Ola Carlson for his support and guidance during my studies and his continued and useful contributions during the final writing of the thesis.

Furthermore, my appreciation and gratitude goes to my supervisor Dr. Peiyuan Chen for his excellent support in this work that enabled me generate a number of publications, thank you so much Dr. Peiyuan. Furthermore, I would to thank my supervisor, Dr. Tarik Abdulahovic, for his support during the follow up meetings. I would also like to appreciate the discussions I had with Dr. Tuan Le. during my studies and for his feedbacks on part of the thesis.

Moreover, I would like to thank the members of the reference group meeting Dr. Philip Kjær from Vestas, Dr. Aron Szucs and Dr. Tomas Jonsson, Dr. Luca Peretti, Dr. France Djikhuizen from ABB, Dr. Anders Holm and Dr. Urban Axelsson from Vattenfall for their comments and inputs during the reference group meetings, thank you all.

In addition, I would like to thank everyone at Electric Power and High Voltage Engineering division for making half of my adult life colourful. My special thanks go to my room mates Gustavo Pinares and Yasir Arafat for making the room an excellent place to be. 1000 tack boss.

Finally, I would like to express my at most gratitude to my family Destu Abdulkadir, Omar Kalid, Zikra Kalid and the one on the way; your unconditional patience, love and support during the difficult times has been the source of my strength. Love you all!

Kalid Yunus,
Göteborg,
March, 2017

List of Abbreviations

AC	Alternating Current
ACC	Auto Correlation Coefficient
AR	Auto Regressive
ARMA	Auto Regressive Moving Average
ARIMA	Auto Regressive Integrated Moving Average
ARIMA(p,d,q)	ARIMA model of order p, d and q
CCC	Cross Correlation Coefficient
CCU	Central Control Unit
CSC	Current Source Converter
CDF	Cumulative Distribution Function
CIGRE	International Council on Large Electric Systems
DC	Direct Current
DE	Germany
DK	Denmark
ENTSO-E	European Network of Transmission System Operators for Electricity
EWEA	European Wind Energy Association
HVDC	High Voltage Direct Current
HVAC	High Voltage Alternating Current
HF	High Frequency
LCU	Local Control Unit
LF	Low Frequency
LF	Low Frequency
LRMC	Short Run Marginal Cost
MA	Moving Average
MC	Marginal Cost
M€	Million Euro

MTHVDC	Multi Terminal High Voltage Direct Current
NL	Netherlands
NO	Norway
PV	Present Value
PAC	Partial Auto Correlation Coefficient
PCC	Point of Common Coupling
PDF	Probability Density Function
PLL	Phase Locked Loop
PSD	Power Spectral Density
Q-Q	Quantile-Quantile
SRMC	Short Run Marginal Cost
TSO	Transmission System Operator
UK	United Kingdom
VARMA	Vector Auto Regressive Moving Average
VSC	Voltage Source Converter
WPP	Wind Power Plant
WPPs	Wind Power Plant

List of Symbols

a_o^{cbl}, b_o^{cbl}	Constants used to calculate the cost of cables
a_o^{inst}, b_o^{inst}	Constants used to calculate the cost of installation
a_o^{vsc}, b_o^{vsc}	Constants used to calculate the cost of VSC
$a(t)$	Gaussian White Noise
A	Cable thickness in mm^2
A_p, B_p	Constants used to calculate cost of cable in SEK/km
B^i	Differencing factor of order i
BB	Buying Bid
BP	Bid Price
BQ	Bid Quantity
C_{sek}^{cabl}	Cost of cable in SEK/km
C^{bloss}	Cost of loss in social welfare
C^{ploss}	Cost of power loss
$C^{ttariff}$	Transmission tariff
C^{inv}	Investment cost
C^{cbl}	Cost of cable
C^{inst}	Cost of installation
C^{vsc}	Cost of VSC
C^{vsc}	Cost of VSC
C_u^{cabl}	Cost of cable in €/km
C_u^{inst}	Cost of installation in €/km
C_u^{vsc}	Cost of VSC in €/km
F_{cutoff}	Cut-off frequency
G_{ki}	Conductance of a cable between terminal k and i
i, j, t	Indexes
m	Gain of a droop controller
m_k	Gain of a droop controller at terminal k
m_{kj}	A measure the change in bus voltage at...
	terminal k due to the change in bus power terminal j
n	Investment period or life time in years, 30 years assumed unless specified
N	Number of terminals in a system

p	Order of Auto-Regression
P_{ij}	Branch power from terminal i to j
P_{ij}^{o}	Initial branch power from terminal i to j before control action
P_k	Bus power at terminal k
P_{k0}	Initial bus power at terminal k before control action
P_{ref}	Reference power at terminal k
$P_{t,i}^{Ex0}$	Predefined time series exchange power in a decentralized electricity market
$P_{t,i}^{Ex}$	Allowable time series exchange power resulting limitation
PV	Present Value Constant
q	Order of Moving Average
r	Interest or discount rate, 5% is assumed unless specified
SB	Selling Bid
S_n	Rated cable power
T	Length of time series data
T_{cutoff}	Cut-off Period
U_{k0}	Initial bus voltage at terminal k before control action
U_k	Bus Voltage at terminal k
U_{ref}	Bus Voltage at terminal k
$U_{t,i}$	Terminal voltage at a given time
v	Power transformation factor
$w(t)$	Wind speed time series
$y_{i,j}$	Conductance of the cable connecting terminal i and j
$y(t)$	Time series data
α	Transmission tariff
γ	Price of electrical energy in €/MWh
ϕ_i	Coefficient of Auto-Regression
θ	Angle between the MC curves of two markets
θ_{min}	A minimum angle required for economical interconnection of two markets
θ_o	A constant in ARMA model
θ_i	Coefficient of Moving Average
μ_s^p	Mean value time series data during p time interval at site s
δ_s^p	Standard deviation of time series data during p time interval at site s

Contents

Chapter 1

Introduction

1.1 Background

In 2009, the EU and the G8 Heads of governments committed their countries to an 80% reduction in GHG (Green House Gas) emissions by 2050 [1]. Another example is the EU 20-20-20 target which aims to reduce emission, increase efficiency and renewable energy all by 20% [1], [2]. Wind is considered to be an important source of renewable energy to help achieve the objective. In Europe, offshore wind constitutes a significant percentage of the renewable energy and the current (2016) offshore wind capacity in Europe is 11,027 MW and it is expected to reach 150,000 MW in 2030 [3], [4].

The majority of the sites considered for offshore wind energy projects are situated close to the coasts (up to few hundred kilometres). However, exploiting the vast wind energy resources in the offshore areas means moving much further out in to the sea. Hence, it is expected that WPPs (Wind Power Plants) in the GW scale will be installed hundreds of kilometres from the shore and over large areas where good wind conditions are available [5], [6]. The increased penetration level of wind energy and the distance in question of course result in techno-economic challenges [7], [8], [9], [10].

To overcome some of the challenges, the building of a meshed transmission grid in Europe is widely discussed. An example is the meshed North Sea transmission grid. The transmission grid in the region can enable wind power in the GW scale to be transported to the external AC grid. The interconnection of wind power over large geographical areas through the meshed grid results in smoothing effect which can reduce wind power variability which in turn can reduce required operational reserves. In addition, the grid can enhance the security of power supply and facilitate competition of electricity trade among countries. The NSCOGI (North Seas Countries Offshore Grid Initiative) describes the advantages of such an offshore grid as providing security of power supply, competition of electricity markets and integration of offshore renewable energy resources [11], [12], [13]. Due to the wide geographical area and the distance in question, an HVDC (High Voltage DC) technology could be used to build the meshed grid. The choice of an HVDC over an HVAC technology for this application is mainly due to the techno-economic reasons [6], [14], [15].

1.2 Problem description

A meshed HVDC grid does not exist anywhere in the world today. Taking the North Sea region as an example, there are a number of existing and planned point to point HVDC transmission systems [16], [17]. For example, Skagerrak 4 is a point to point VSC(Voltage Source Converter) HVDC transmission system connecting power systems in Norway and Denmark. The system is built to increase the power exchange capacity between the two countries which in turn facilitates greater levels of wind energy into the Danish power system by allowing potential intermittency issues to be mitigated by the Norwegian hydro power. Another example of a point to point VSC HVDC transmission system is BorWinn1 [18]. The system is used to connect an offshore wind farm to the main land grid in Germany. There are a number of other similar operational and planned HVDC transmission systems in the region which can be used for power exchange or to transport power from WPPs to the main land grids [16], [17], [19].

It is unlikely to build the future meshed HVDC grid at once. According to a working group in CIGRE, the first step towards a fully meshed HVDC grid is a simple non-meshed multi-terminal configuration [20]. This development could start from an inter-connector or from an offshore WPP (Wind Power Plant) connection. Figure 1.1 shows the building of an HVDC grid from existing inter-connectors and WPPs. A WPP is added onto the inter-connector and then additional inter-connectors are added on top of the resulting system. More inter-connectors and WPPs can be added onto this system to create a fully meshed HVDC grid with WPPs and interconnection with the external AC grids [20], [21].

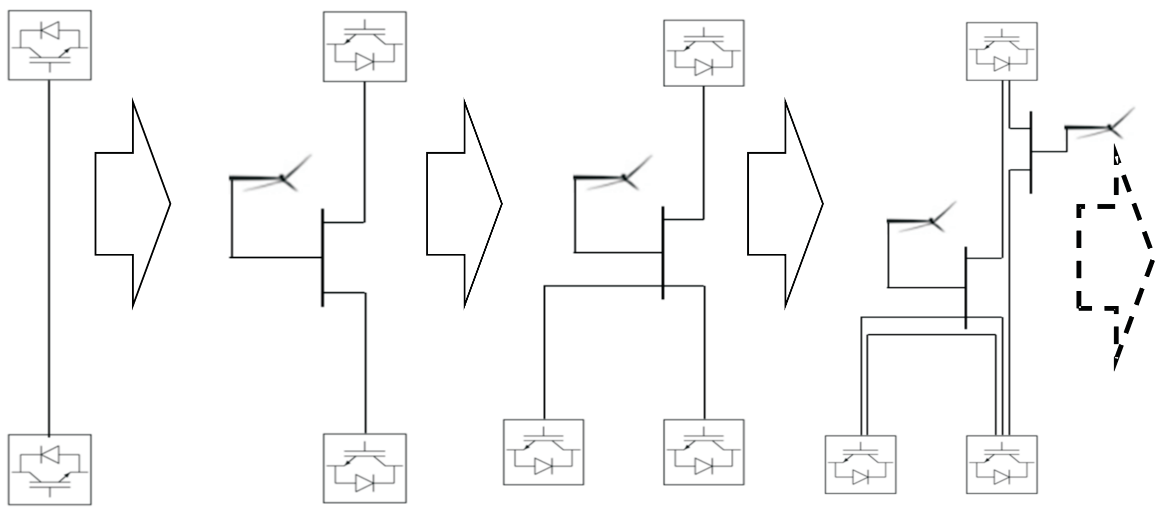

Figure 1.1: Building a meshed HVDC transmission grid in steps

There are a number of studies on HVDC grids in general and HVDC grid in the North Sea region in particular. For instance, in [22] the aim of the North Sea transnational grid research project was described. In [13] and [23], an overview of the possible technologies that can be used in the building of the grid in the North Sea area were described. In [24] an overview of the technical, economical and regulatory obstacles of building a European super grid was discussed. In [25], a bench mark test system for the offshore grid in the

North Sea was presented. In [26], an overview of a feasibility study of an offshore HVDC grid was made, where the focus is on the need for a highly reliable coordinated control function for the system and the need for a selective protection plan for a reliable operation of the system. In [27], steady state and dynamic modelling of a VSC HVDC systems for power system simulations were presented. A study on MTHVDC (Multi-Terminal HVDC) networks with a focus on system integration, dynamics and control was made in [28]. In [29], the control, dynamics and operation of VSC MTHVDC transmission system was studied. From an operation and a control point view, the main focus of the study in [29] was on a precise control of scheduled powers in a system operated by voltage droop controllers. In addition, the concept of a secondary control is also introduced where the main focus is on mitigating unintended deviations in the scheduled powers resulting from the actions of the short-term voltage droop controllers in the system. Many of the studies on HVDC grids consider a fixed system configuration. To the author's knowledge, there is a lack of publicly available studies that investigated and quantified economical and technical aspects of a stepwise building of an HVDC grid in general and the HVDC grid in the North Sea in particular.

1.3 Objectives

The overall objective of the thesis is to contribute with knowledge in the process towards obtaining a meshed or a multi-terminal HVDC networks in the North Sea. The resulting goals of the thesis are, therefore, to formulate, investigate and quantify economical and technical aspects of building such a network. Particular attention is paid to the optimum sizing of system components in building the grid. In addition, the objective is to establish the minimum slope difference requirements, between the MC curves of markets, for an economical interconnection of the markets through a VSC HVDC transmission technology. Furthermore, the thesis also aims in the mathematical tools that can be used in the studies of such a system expansion. Finally, an objective is to derive a large area wind power modelling suitable for studies of sea based HVDC networks consisting of WPPs distributed over a large area.

1.4 Thesis structure

In order to enhance knowledge in the stated objectives, the thesis is structure as follows. In Chapter 2, technical aspects of controlling a meshed HVDC transmission system at steady state are investigated and a steady state control strategy is developed. In addition, methods for estimating the costs of the components, that are used in the economic studies in the following chapters, are developed and discussed.

In Chapter 3, ARMA based models, that can be used to simulate temporally and spatially correlated wind power data, are developed. The results in this chapter are used to provide time series wind power data from WPPs, which are used in the economic analysis of WPP integration into existing systems.

In Chapter 4, the modelling and investigation of optimum sizing of VSC HVDC transmission system, based on a pre-defined exchange power, is presented. In Chapter 5, the modelling and investigation of optimum sizing of VSC HVDC transmission system expansion, based on a centrally operated energy brokerage market model, is discussed. In both Chapter 4 and 5, inputs from the previous chapters, mainly component cost estmation methods from Chapter 2 and wind power time series data from Chapter 3, are used.

1.5 Contributions

In general, the thesis has contributed with knowledge around the stated objectives; starting from the parametrization of the cost of VSC HVDC system components to the economic analysis of building a meshed VSC HVDC grid in steps out of which a number of publications are made. To sum up, the following are the main contributions of this study to the best knowledge of the author.

- Optimization models that can be used in the investigation of a stepwise building of a VSC HVDC transmission system, based on a predefined time series exchange data and centrally operated market structure, are developed.
- The per unit cost of a VSC HVDC transmission system (LRMC) is quantified from which the minimum transmission tariff, that makes the investment profitable, can be established.
- Minimum angle or slope difference requirements between the MC curves of electricity markets, for an economical interconnection of the markets, is established where particular attention is placed on cases where net exchange power within the markets is close to zero
- A modified ARMA based modelling procedure, that can be used to simulate temporally correlated time series wind speed and hence wind power, is another contribution. The most significant contribution in this part of the work is the introduction of frequency decomposition in the modelling procedure.
- A modified VARMA modelling procedure, that can be used to simulate not only temporally but also spatially correlated time series wind speed, is another contribution.
- And finally, a steady state control strategy which is based on local droop controllers (primary control) followed by a central secondary controller (supervisory control) is another contribution of the thesis.

1.6 Publications

The publications resulting from this thesis are listed as follow

I Kalid Yunus, Torbjörn Thiringer, and Peiyuan Chen. "ARIMA-Based Frequency-

Decomposed Modeling of Wind Speed Time Series." IEEE Transactions on Power Systems 31.4 (2016): 2546-2556.

II Kalid Yunus, Peiyuan Chen, and Torbjörn Thiringer. "Modelling spatially and temporally correlated wind speed time series over a large geographical area using VARMA." IET Renewable Power Generation (2016).

III Kalid Yunus, Peiyuan Chen, and Torbjörn Thiringer. "Economic analysis and optimum dimensioning of VSC HVDC transmission system." Submitted to EES Electric Power System Research (2016).

IV Kalid Yunus, and Torbjörn Thiringer. "Primary - Secondary control strategy for meshed HVDC transmission grids at steady state." Power and Energy Engineering Conference (APPEEC), 2015 IEEE PES Asia-Pacific. IEEE, 2015.

V K. Yunus, T. Thiringer, and O. Carlson, ”Steady state controll strategy for a meshed hvdc grid with wind power plants,” in 12th Wind Integration Workshop, International Workshop On Large Scale Integration of Wind Power into Power System as well as on Transmission Networks for Offshore Wind Power Plants; 22-24 October 2013, London UK.

VI K. Yunus, T. Thiringer, and O. Carlson, ”Droop based steady state control algorithm for a meshed hvdc grid,” in 2014 IEEE PES Transmission and Distribution Conference and Exposition; 15-17 April 2014 in Chicago, IL, USA, 2013.

VII K. Yunus”Steady state analysis of HVDC grid in the North Sea with offshore wind power plants”; Licentiate thesis, Chalmers University of Technology, 2014. - 130 s.

The author has also contributed to the following publications

I K. Yunus, H. De La Parra, and M. Reza, ”Distribution grid impact of plug-in electric vehicles charging at fast charging stations using stochastic charging model,” in Proceedings of the 2011-14th European Conference on Power Electronics and Applications (EPE 2011), 30 Aug - 01 Sep 2011, Birmingham, United Kingdom.

II K. J. Yunus, M. Reza, H. Zelaya-De La Parra, and K. Srivastava, ”Impacts of stochastic residential plug-in electric vehicle charging on distribution grid,” in Innovative Smart Grid Technologies (ISGT), 2012 IEEE PES, Jan. 2012, pp. 1-8.

III K. Yunus, G. Pinares, L. Tuan, and L. Bertling, ”A combined zone-3 relay blocking and sensitivity-based load shedding for voltage collapse prevention,” ISGT Europe, 2010 IEEE PES, 11 Oct - 13 Oct 2010, Chalmers Lindholmen Gothenburg, Sweden.

IV A. Marinopoulos, J. Pan, M. Zarghami, M. Reza, K. Yunus, C. Yue, and K. Srivastava, ”Investigating the impact of wake effect on wind farm aggregation,” in PowerTech, 2011 IEEE Trondheim, Jun. 2011, pp. 1-5.

Chapter 2

Building the future HVDC transmission grids

2.1 HVDC transmission system

In the history of electric power system, DC was the first type of transmission technology used. Although AC transmissions later on came to play important roles, the development of DC transmissions has continued [30]. Today, the need to transport bulk power over long distances, and in particular under the sea, has raised the interest in DC transmission system, which is referred to as HVDC due to the high voltage involved [17].

HVDC transmission systems can be classified into CSC (Current Source Converter) and VSC (Voltage Source Converter) based on the type of converter technology used in the system. CSC are still the most used for the application of bulk power transmission. However, VSC is becoming popular for HVDC transmission applications mainly because of its higher flexibility compared to the classical CSC [31],

There are different configurations of HVDC transmission systems. Figure 2.1 shows the main elements of a bipolar VSC HVDC transmission system. The system is composed of two VSCs and a transmission link connecting two converter stations. Each converter is connected to an AC grid through a phase reactor, a filter and a transformer [31].

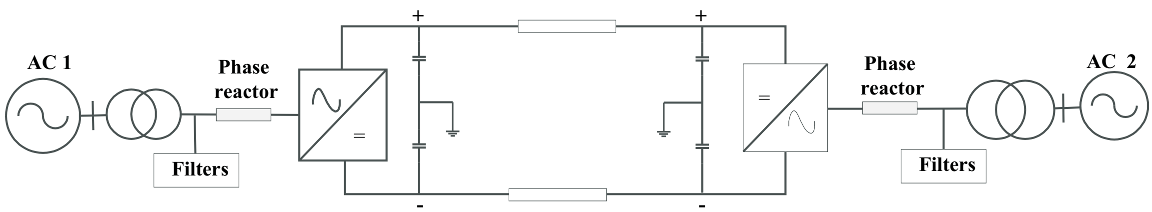

Figure 2.1: Typical configuration of bipolar VSC HVDC transmission system

A number of VSC HVDC transmission systems are commissioned worldwide and systems with power ratings from a few tenths of MW up to over 1000 MW are available [17]. Table 2.1 shows some of the existing VSC based HVDC transmission systems worldwide [31], [17]. As can be seen from the figure, all of the existing VSC HVDC transmission systems are point-to-point but meshed HVDC transmission systems do not exist today. According to the data in the table, the highest voltage and power in the installed systems are ±350 kV and 600 MW respectively

Table 2.1: Examples of VSC HVDC projects worldwide

Project	Capacity	Voltage	Distance	Cost	Year	-shore	Country(s)
Gotland HVDC LightÂ®	50MW/ ± 25MVar	± 80 kV	2 x 70 km		1999	Off	Sweden
Directlink	3 x 60 MW	± 80 kV	6 x 65 km		2000		Australia
Tjæreborg	8 MVA	± 9 kV	2 x 4.5km		2000	Off	Denmark
Eagle Pass	36 MVA	132 kV	Back2back		2000		US
MurrayLink	200 MW	± 150 kV	2 x 180 km		2002		Australia
Troll A	2 x 40 MW	± 60 kV	4 x 68 km		2005	Off	Norway
Estlink	350 MW	± 150 kV	2 x 105 km		2006		Finland
Valhall	78 MW	150 kV	300 km		2009		Norway
BorWin1	400 MW	± 150 kV	2 x 200 km		2009	Off	Germany
Caprivi Link	2 x 300 MW	± 350 kV	970 km		2009		Zam/Nam
SylWin1	864 MW	± 320 kV	205 km		2015	Off	Germany
Skagerrak 4	700 MW	500 kV			2015	Off	NO-DK
NordBalt	700 MW	300 kV	400 km		2016	Off	SE-LT

A meshed HVDC grid can be formed from point-to-point transmission systems where two or more branch cables share the same converter in the system. Similar to a point-to-point HVDC transmission system, there are different ways of configuring a meshed HVDC transmission system [31], [20]. Figure 2.2 shows a simplified single line diagram of a bi-

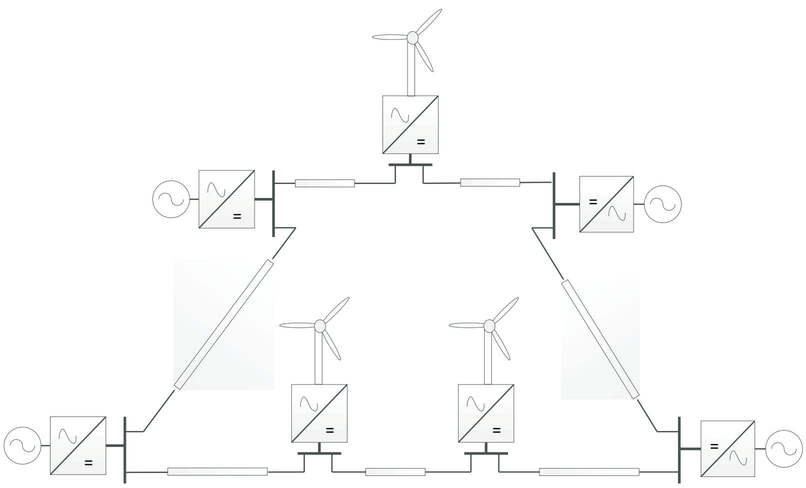

Figure 2.2: Seven terminal meshed VSC HVDC transmission grid connecting external AC grids and wind power plants

polar meshed VSC HVDC grid connecting four external AC systems and three wind power plants. Note that the phase reactors, the filters and the transformers are omitted from the circuit for the sake of simplicity.

2.1.1 Visions of HVDC grids

A meshed HVDC transmission grid does not exist today anywhere in the world. However, there are a number of point to point HVDC transmission systems which are already in operation and used for different purposes. Taking the North Sea region as an example, the NorNed is an HVDC transmission link which is used for power exchange by connecting the power systems in Norway and in the Netherlands [32]. Another example is the BorWin1 HVDC transmission system which is used to connect offshore wind farms to the shore in Germany. There are a number of other HVDC transmission systems in the area which are in operation.

Moreover, there is a growing interest to build a meshed HVDC grid in the North Sea area. There are a number of forces driving the idea of building the meshed HVDC grid in the area. One of the drivers is a market force; the desire to generate more revenue by transporting more exchange power over the meshed HVDC grid. Another driving force is the need to enhance security of power supply in the region by using interconnected systems. In addition, there is also a growing interest to integrate more and more WPPs into the main grid in the region, which is another driving force. Hence, there are a number of planned HVDC transmission projects in the area aiming to realise the future meshed HVDC grids.

As a result of the increasing interest to build an HVDC grid in the North Sea region, some stakeholders have already proposed the visions of a meshed HVDC grid in the region. The are a number of visions HVDC grid in the North Sea. The visions of HVDC grid in the North Sea from Examples of the visions of HVDC grid in the North Sea, the ones from EWEA (European Wind Energy Association); from Airtricity, an Irish wind farm developer and the visions from Sintef and Statnett are some of the examples [19], [33], [29].

As discussed in Section (1.2), a meshed HVDC grid does not exist today and it is unlikely to build it at once. The future HVDC grid can be built in steps and the first step towards a fully meshed HVDC grid is a simple non-meshed configuration. In order to justify the formation of a meshed HVDC grid from a simpler systems through interconnections, the resulting benefits of the interconnection need to be quantified. In order to quantify the benefits, is important to model the costs of the components of the system, the exchange profiles in the system, the spatially and temporally correlated wind power profiles from the Wind Power Plants (WPP) and other related parameters which are all discussed in the subsequent sections and chapters.

2.2 Power flow control

Similar to an AC system, the power flow in a DC system is governed by the voltage differences and system impedance [34], [27]. The power flow equation of a meshed HVDC grid is derived in Appendix B and is formulated as

$$P_k = \sum_{j=1}^{N} |U_k|\,|U_j|\,G_{kj} \tag{2.1}$$

where P_k is active power injected at bus k, U_k and U_j are DC voltages at bus k and j respectively, G_{kj} is conductance of the branch connecting bus k and bus j and N is the number of buses in a system. The power flow equation presented in (2.1) is non linear and requires a non-linear method to solve it. Hence, the NR (Newton-Raphson) method, presented in Appendix B, is used to solve the power flow equation in (2.1).

Observe that for a stable operation of a system, the magnitude of bus power injected into the system should be set in such a way that the bus voltages should be kept within the allowable margin and branch currents in the system should be kept within the ratings of cables in the branches. A disturbance in the system could disturb the stability of the system. Hence, there has to be controllers in the system that reacts to the disturbance and maintain the system parameters within the allowable range.

A power flow in an HVDC transmission system is the result of the actions of the controllers in the converter stations [35]. The objective of a power flow control in an HVDC transmission system is to control the DC voltage in the system within its limits and fulfilling the power input/output at the PCC (Point of Common Coupling) to the AC system without exceeding maximum currents through the valves, lines or cables [20]. Figure 2.3 shows a block diagram of a controller at one converter station in a point-to-point HVDC transmission system. As can be seen from the block diagram, the controller can be set in different

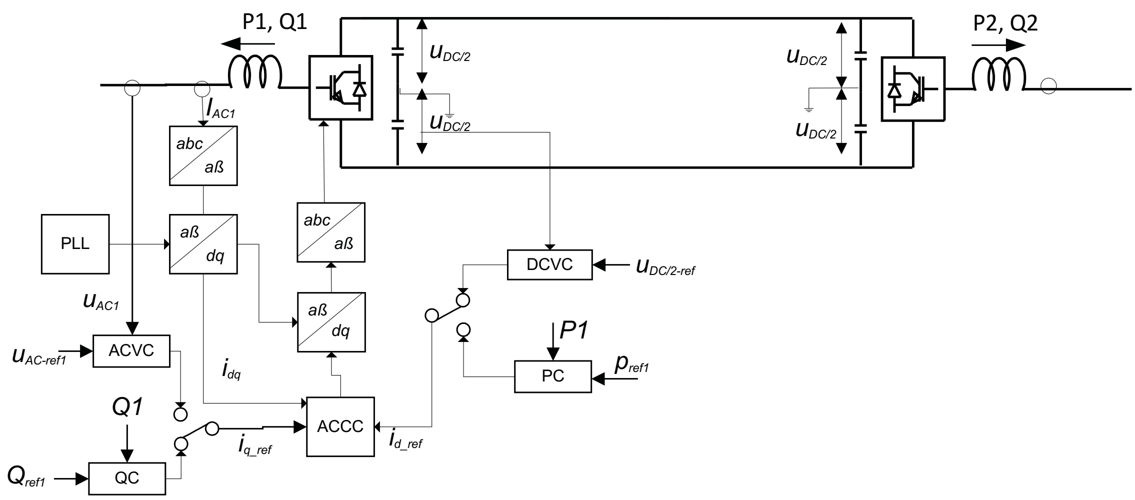

Figure 2.3: Control of a point-to-point HVDC transmission system

control modes. On the AC side of the converter, either AC voltage or reactive power can be controlled. On the DC side of the converter, either DC voltage or DC power can be controlled, which is the control mode relevant for the study in this thesis, since only the DC side of the grid is considered.

2.2.1 Local droop control

In a point-to-point HVDC transmission system, if one converter controls the DC voltage, the other converter controls DC power [29]. However, controlling a meshed HVDC grid is not as simple as controlling a point-to-point HVDC transmission system. Several methods are suggested in the literature to control a power flow in a meshed transmission grid [36], [29]. Among these methods, voltage droop control strategy is the most popular. The basic principle of voltage droop control in the DC system is similar to frequency droop control in an AC system. In an AC system, droop control is used as a primary control, using frequency as power balance signal, to share power deviation (resulting from disturbances in the system) among different generators in the system having the control capability [34].

However, in a DC grid, the power balance signals are system bus voltages. When there is less power injected into a DC grid, the system bus voltages decrease and vice versa. Hence, in a meshed HVDC grid with local droop controllers, when the system bus voltages decrease, the droop controllers react by injecting more power into the system. Similarly, when the system voltages increase, the droop controllers react by reducing the power injected into the system so that the system bus voltages decrease. Figure 2.4 shows an example of droop controller configuration and droop controller parameter characteristics. Figure 2.4(a) shows a droop controller configuration at a converter station. Observe that for a negative value of the droop characteristics (m), when the bus voltage (U) is less than the reference (U_{ref}), the reference power to the converter (P_{ref}) gets higher. Similarly, when the bus voltage is higher than the reference voltage, the reference power to the converter gets lower. The magnitude of the reaction of a local droop controller depends on the mag-

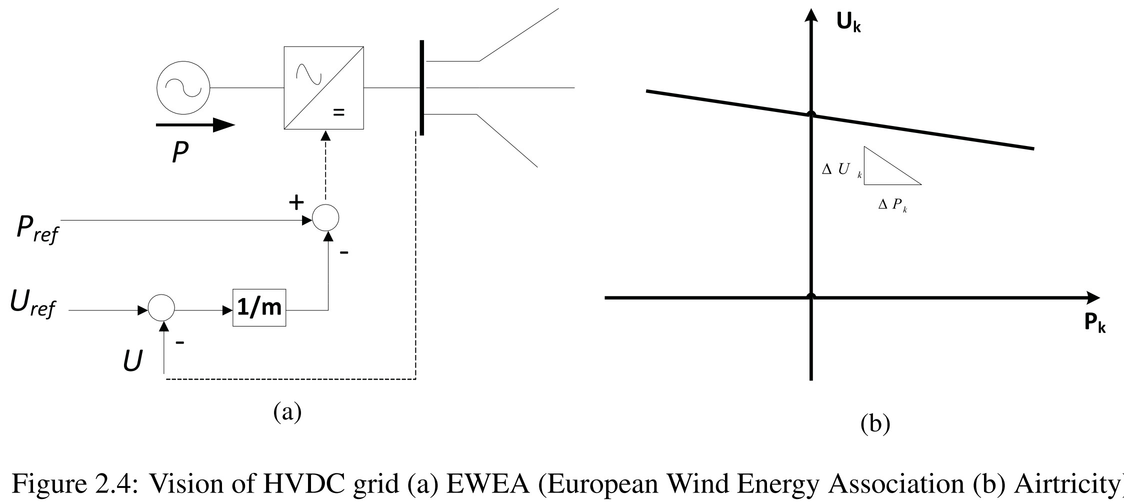

Figure 2.4: Vision of HVDC grid (a) EWEA (European Wind Energy Association (b) Airtricity)

nitude of the slope of the droop characteristics used in the controller (m). Figure 2.4(b) shows a voltage droop characteristic. It is a linear relationship defined by a voltage and a power of a bus in a system. For a given slope of the droop characteristics (m) used in a droop controller, the magnitude of the reaction of the droop controller can be calculated as

$$\frac{\Delta U_k}{\Delta P_k} = \frac{U_k - U_{k0}}{P_k - P_{k0}} = m_k ==> \Delta P_k = \frac{1}{m_k}\Delta U_k \tag{2.2}$$

The relation in (2.2) can be combined with the DC power flow equation in (2.1) to form a steady state model of the power flow equation with the local droop controllers. Assume that bus k has a droop control capability with a voltage droop characteristics having a slope m_k, and assume also that P_k is the scheduled or reference power injected at the same bus. If there is a deviation in voltage at bus k (ΔU_k) from the reference due to a disturbance; the reference power at the bus (P_k) is reduced by an amount ΔP_k, which is given in (2.2). The steady state model of the HVDC grid with droop controllers can then be formulated as

$$P_k - \Delta P_k = P_k - \frac{1}{m_k}\Delta U_k = U_k \sum_{j=1}^{n} G_{kj} U_j \tag{2.3}$$

where P_k is the scheduled or the reference power injected at bus k, ΔU_k is the change in voltage at bus k and m_k is the slope of the droop characteristics at bus k which must have a negative value.

In an HVDC grid, some buses in the system may not have droop control capability. Hence, in a system having n number of buses, if a converter at bus k does not have droop control capability, the value of the slope m_k in (2.2) is set to ∞ to represent this. If the value of m_k in (2.2) is ∞, ΔP_k will be zero, for any value of ΔU_k. From control a point of view, the controller at bus k controls the bus power to a fixed reference value, P_k. If the value of m_k is zero, it means that the bus k is a slack bus (the change in voltage at the bus is zero). In general a typical recommended value of the droop parameter, m_k, ranges from 3% to 4% [29].

A base system in Figure 2.5 is used to demonstrate the steady state operation of droop controllers, which is formulated in (2.3). The network parameters shown in Table 2.2 is used for the simulation. A 3% droop parameter is assumed for droop controllers. In addition, terminal powers of -0.72pu, -0.56pu and 1.29pu at bus 1, 2 and 3 respectively are considered as a reference case where a base power of 1033MW is considered (refer Appendix A for pu calculation). In the simulation, it is assumed that the controller at terminal 1 is used in voltage control mode ($slack - bus$), the one at terminal 2 is used in droop control mode and the controller at terminal 3 is used in power control mode. Note

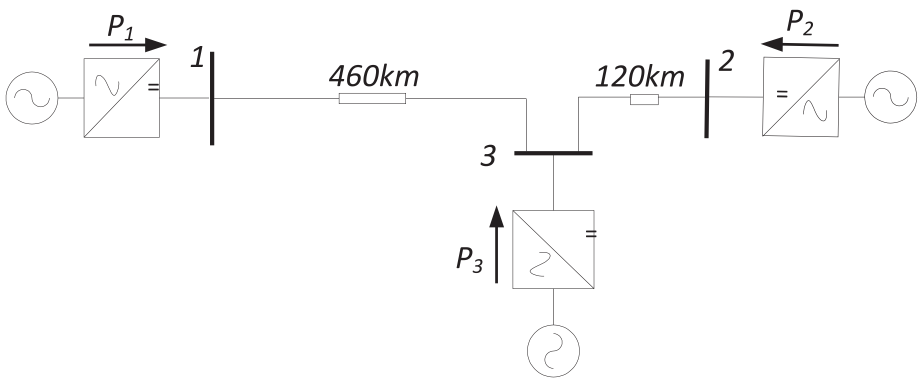

Figure 2.5: Topology of a three terminal HVDC transmission system

that the data in Table 2.2 is taken from the database of cable technologies presented in [17]. Note also that the transmission technology used is a bipolar VSC HVDC transmission

Table 2.2: Network data of the the three terminal system

From bus	To bus	R(ohm/km)	Power(MW)	Area(mm^2)
1	3	0.00755	943x1	1200x2
2	3	0.00755	943x1	1200x2

technology with a voltage level of ±320 kV, which is considered as a base value. Hence, the resistance and the power values presented in the tables are the total equivalent of the bipolar system, however, the areas are for a single cable in a pole.

Figure 2.6 shows simulation results of the system with the droop controller at terminal 3 when a 20% power step is introduced to the system through Bus 3. Note from Figure 2.6(a) that the disturbance is initiated at time t_1. The results in the figure shows an instant reduction of power at terminal 1 and 2 at the same time as a reaction to the increase in power at terminal 3. Figure 2.6(b) shows an increased branch power flows after the disturbance which are all within limits. Observe that the branch power flows in Figure 2.6(b) are normalized values which are determined by dividing the actual branch power flows by the ratings of the individual cables. Other per unit values are calculated by using a base power and voltage of 1033MW and 640kV respectively.

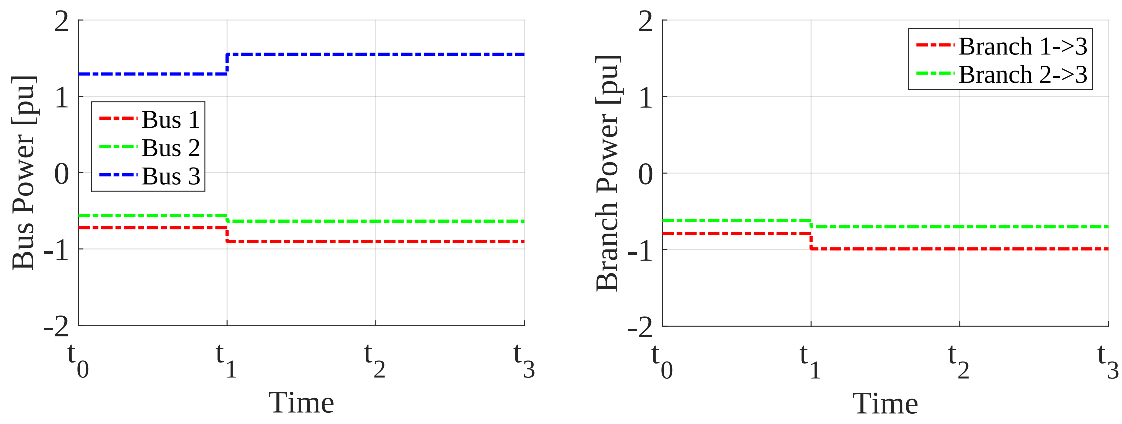

(a) (b)

Figure 2.6: Simulation results of the 3 terminal system with the droop controller for a 20% power step at terminal 3 (at time t_1)

Figure 2.7 shows the simulation results when the disturbance at terminal 3 is 40%. Similar to the case in Figure 2.6, the power step is initiated at time t_1. At the same time, the droop controller reacts to the disturbance and increases the bus powers at terminal 1 and 2 as can be seen in Figure 2.7(a). The result of this is an increase in branch power flows as can be seen in Figure 2.7(b). Note from the results in Figure 2.7(b) that the power flow on branch $1- > 3$ exceeds the rating of the cable. This indicates that local droop controllers, which is referred to as primary controllers, do not guarantee that the branch power flow limits are maintained. In order to avoid this problem, it is important to have a centralised supervisory controller secondary controller that could be activated when there are limit violations in the system. In the following section, a proposed control strategy that consists of local droop controllers (primary controllers) and central supervisory controller (secondary controller) is discussed.

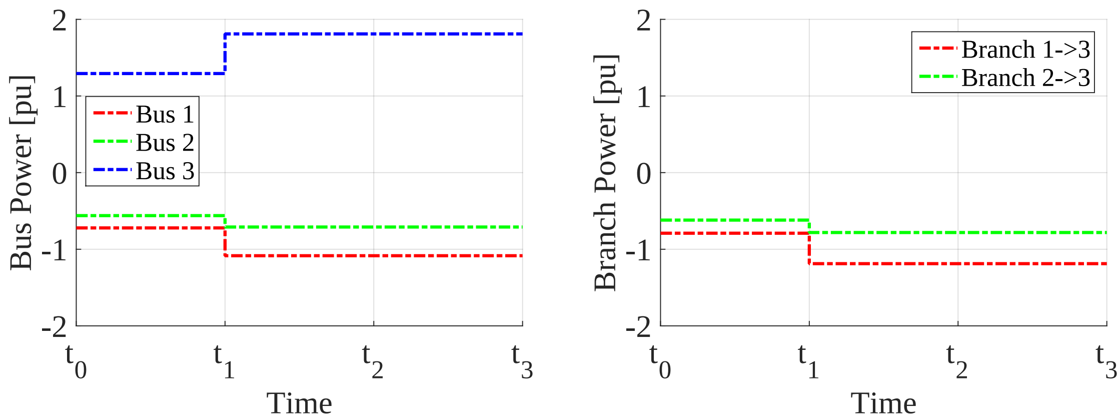

(a)

(b)

Figure 2.7: Simulation results of the 3 terminal system with the droop controller for a 40% power step at terminal 3 (at time t_1)

2.2.2 Supervisory control

As indicated in Section 2.2.1, the local droop controllers or primary controllers do not guarantee that the branch power flows are maintained within limiting values after the actions of the primary controllers. This is the basis to justify the need for a centralized supervisory controller. The action of the centralized supervisory controller is needed only when there is/are branch power flow limit violation(s). The role of the supervisory controller is to update the reference power and voltage of the local droop controllers, when required, such that the limit violations could be avoided.

The supervisory control model proposed in this thesis is established by relating the required change in bus power to the desired change in branch power flow. The branch power flow from bus i to bus j, P_{ij}, can be formulated as

$$P_{ij} = U_i \left(U_i - U_j\right) G_{ij} \tag{2.4}$$

where U_i is the voltage at bus i, U_j is the voltage at bus j and G_{ij} is the branch conductance. Suppose a change in the branch power flow from P_{ij}^0 to P_{ij} is of interest, the desired change in branch power flow, ΔP_{ij}, can be formulated as

$$\begin{aligned} \Delta P_{ij} &= P_{ij} - P_{ij}^0 \\ &= U_i G_{ij} \left(U_i - U_j\right) - U_i^0 G_{ij} \left(U_i^0 - U_j^0\right) \end{aligned} \tag{2.5}$$

where U_0 and U_i are the initial and the desired bus voltages respectively. The change in bus voltage, compared with the magnitude of the bus voltage, is significantly small. Hence, the approximation, $U_i \cong U_{i0}$, can be considered valid and equation (2.5) can then be simplified into

$$\begin{aligned} \Delta P_{ij} &\cong U_i G_{ij} \left((U_i - U_i^0) - (U_j - U_j^0)\right) \\ &= U_i G_{ij} \left(\Delta U_i - \Delta U_j\right) \end{aligned} \tag{2.6}$$

For the three bus system in Figure 2.5, ΔP_{ij} and $\Delta U_i/\Delta U_j$ can be related as

$$\begin{aligned} \Delta P_{12} &= U_1 G_{12} \Delta U_1 - U_1 G_{12} \Delta U_2 \\ \Delta P_{23} &= U_2 G_{23} \Delta U_2 - U_2 G_{23} \Delta U_3 \end{aligned} \tag{2.7}$$

Assuming that $\Delta U_1 = 0$, (2.7) can be reformulated as

$$\begin{bmatrix} \Delta P_{12} \\ \Delta P_{23} \end{bmatrix} = \begin{bmatrix} -U_1 G_{12} & 0 \\ U_2 G_{23} & -U_2 G_{23} \end{bmatrix} \begin{bmatrix} \Delta U_2 \\ \Delta U_3 \end{bmatrix} \tag{2.8}$$

Note from (2.8) that for the desired change in branch power flow, the required change in voltage can be calculated. One way to affect the change in bus voltages is by using DC/DC converters in the system. The use of DC/DC converters in an HVDC grid could be limited due to techno-economic challenges. Achieving the change in bus voltages, and hence the change in branch power flow without using DC/DC converters, is therefore of great importance, which is the main focus of this section.

A change in bus voltages in a system can be related to the change in bus powers in the system. The change in power at bus j results in a change in voltage at bus k which is linearly related as

$$m_{kj} = \frac{\Delta U_k}{\Delta P_j} \tag{2.9}$$

where m_{kj} is the slope of a line produced by the variation of voltages at bus k resulting from the variation of power at bus j, when the power at the rest of the system buses are kept constant. In a similar way, the change in bus voltages resulting from the change in bus powers in the system can be formulated as

$$\begin{aligned} &\begin{bmatrix} \Delta U_1 \\ \Delta U_2 \\ \cdot \\ \cdot \\ \cdot \\ \Delta U_N \end{bmatrix} = \begin{bmatrix} m_{11} & m_{12} & . & . & . & m_{1N} \\ m_{21} & m_{22} & . & . & . & m_{2N} \\ \cdot & \cdot & \cdot & \cdot & \cdot & \cdot \\ \cdot & \cdot & \cdot & \cdot & \cdot & \cdot \\ \cdot & \cdot & \cdot & \cdot & \cdot & \cdot \\ m_{N1} & m_{N2} & . & . & . & m_{NN} \end{bmatrix} \begin{bmatrix} \Delta P_1 \\ \Delta P_2 \\ \cdot \\ \cdot \\ \cdot \\ \Delta P_N \end{bmatrix} \\ &==> [\Delta U] = [M]\,[\Delta P] \end{aligned} \tag{2.10}$$

where ΔU_i is the change in voltage at bus i, ΔP_j is the change in power at buses j, m_{ij} is calculated as in (2.9). For the system in Figure 2.5, (2.10) is reduced into

$$\begin{bmatrix} \Delta U_1 \\ \Delta U_2 \\ \Delta U_3 \end{bmatrix} = \begin{bmatrix} m_{11} & m_{12} & m_{13} \\ m_{21} & m_{22} & m_{23} \\ m_{31} & m_{32} & m_{33} \end{bmatrix} \begin{bmatrix} \Delta P_1 \\ \Delta P_2 \\ \Delta P_3 \end{bmatrix} \tag{2.11}$$

Assuming that the voltage at bus 1 is fixed irrespective of the change in bus power in the system, (2.11) can be reduced into

$$\begin{bmatrix} \Delta U_2 \\ \Delta U_3 \end{bmatrix} = \begin{bmatrix} m_{22} & m_{23} \\ m_{32} & m_{33} \end{bmatrix} \begin{bmatrix} \Delta P_2 \\ \Delta P_3 \end{bmatrix} \tag{2.12}$$

Combining (2.8) and (2.12), the desired change in branch power can be related to the required change in bus power as

$$\begin{bmatrix} \Delta P_{12} \\ \Delta P_{23} \end{bmatrix} = \begin{bmatrix} -U_1 G_{12} & 0 \\ U_2 G_{23} & -U_2 G_{23} \end{bmatrix} \begin{bmatrix} m_{22} & m_{23} \\ m_{32} & m_{33} \end{bmatrix} \begin{bmatrix} \Delta P_2 \\ \Delta P_3 \end{bmatrix} \tag{2.13}$$

The same procedure can be used to develop the relation in (2.13) for systems with more terminals and different topologies. Different network topologies and multi terminal systems are investigated in Paper IV, V and VI.

In Figure 2.7, it is shown that when the step power (disturbance) at terminal 3 is 40%, the power flow on branch $1- > 3$ exceeds the cable rating after the action of the local droop controller (primary controller). Hence, as can be seen from the results in Figure 2.8, the supervisory or the secondary controller steps in at time t_2 to limit the power flow on branch $1- > 3$ to its rated value, as can be seen in Figure 2.8(a). This is achieved by re-setting the reference voltage and power to the droop controller by using (2.13), as can be seen in Figure 2.8(b).

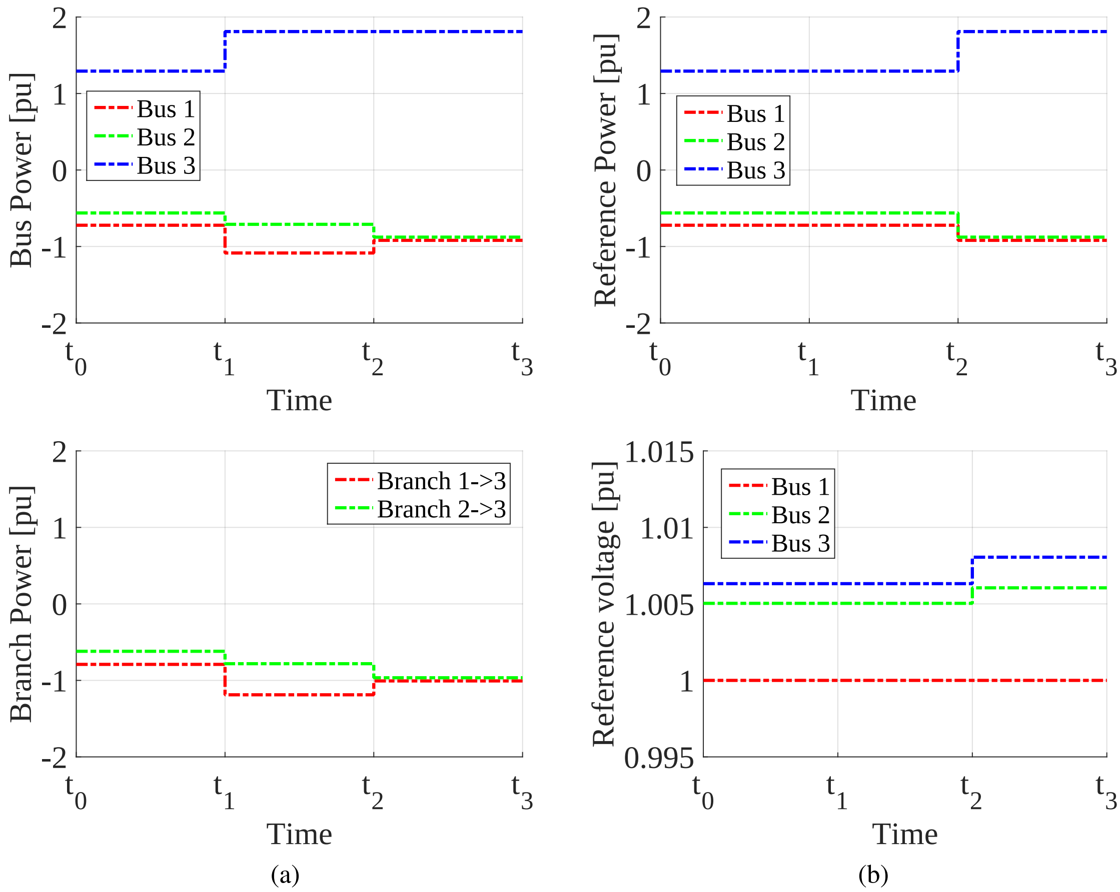

Figure 2.8: Simulation results of the 3 terminal system with the local droop controller followed by a centralized supervisory controller for a 40% power step at terminal 3 (at time t_1)

Observe that in order to produce the results in Figure 2.8, it is assumed that we cannot control the power at terminal 3 ($\Delta P_3 = 0$ in (2.13)) since it is where the disturbance (power step in this case) is located. Hence, for the desired change in branch power flow, the only controllable bus power is ΔP_2. This means that we can control the power flow on only one branch. This is one of the limitations in the proposed control strategy. Figure 2.9 shows the simulation results when the disturbance is 60%. Note that before the action of the secondary controller, the violation is only on branch $1->3$. Hence, the controller chooses branch $1->3$ to control the power flow to its rated value. As can be seen from the results in Figure 2.9(a), the secondary controller does indeed manage to bring the branch power flow back to the rated value. The result, however, is that the power flow on branch $2->3$ is violated after the action of the secondary controller. This is the limitation of the proposed control strategy. Generally, the proposed control strategy can control power flows on n branches if the power at n buses are controllable as can be seen from (2.13).

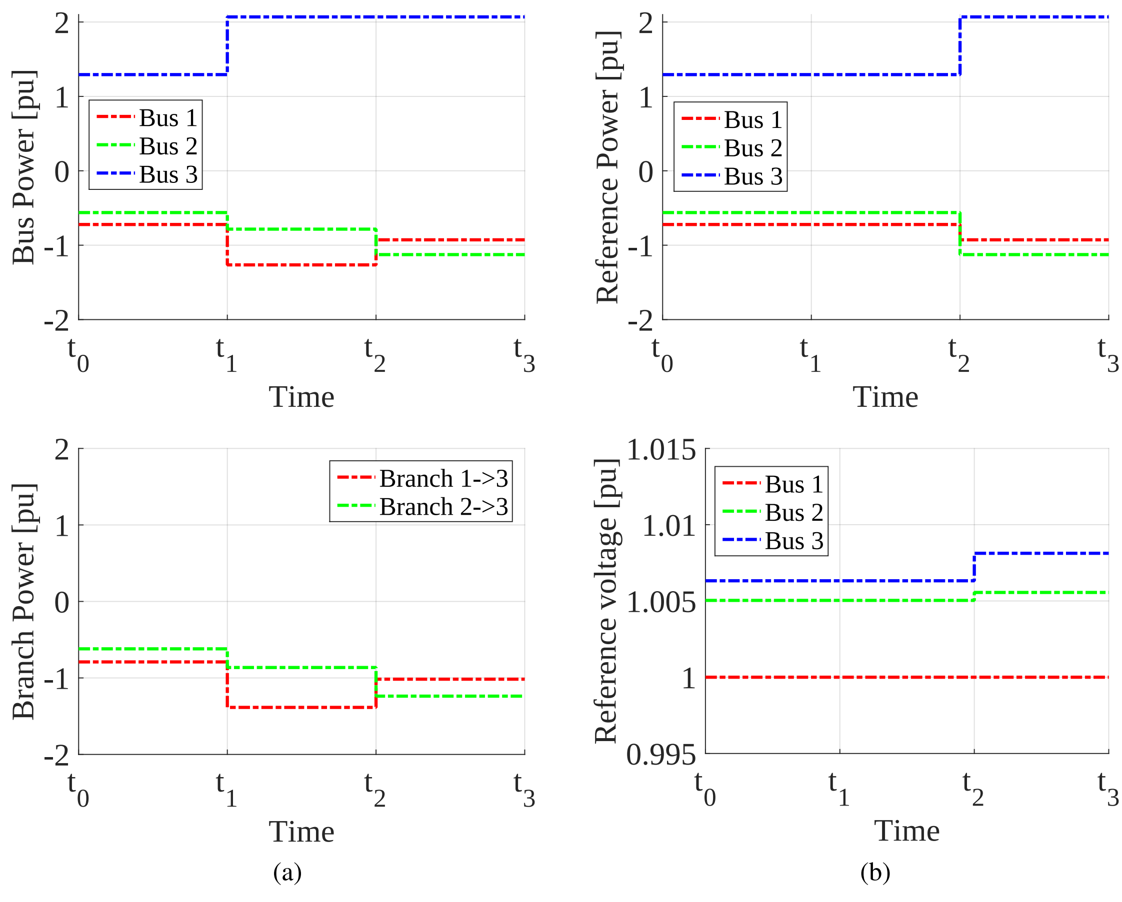

Figure 2.9: Simulation results of the 3 terminal system with the local droop controller followed by a centralized supervisory controller for a 60% power step at terminal 3 (at time t_1)

2.2.3 Architecture of the proposed control strategy

Observe that the proposed control strategy consists of not only the centralized secondary controller, but also the local primary controllers. Fig. 2.10 shows the architecture of the proposed control strategy with an HVDC grid interconnecting external AC transmission systems. In the example shown, every external grid is connected to the HVDC grid through a converter having a primary controller and a LCU (Local Control Unit). The LCU can measure bus power, bus voltage and local branch powers and provides the data to the CCU (Central Control Unit). When there is a disturbance in the system (at time t_1), the primary controllers in the system react to the disturbance according to their droop settings (at time t_2). The CCU takes in measurement data from the LCUs and provide new reference powers and voltages to the LCUs that can be used by the local droop controllers when there is branch power flow limit violations (at time t_3).

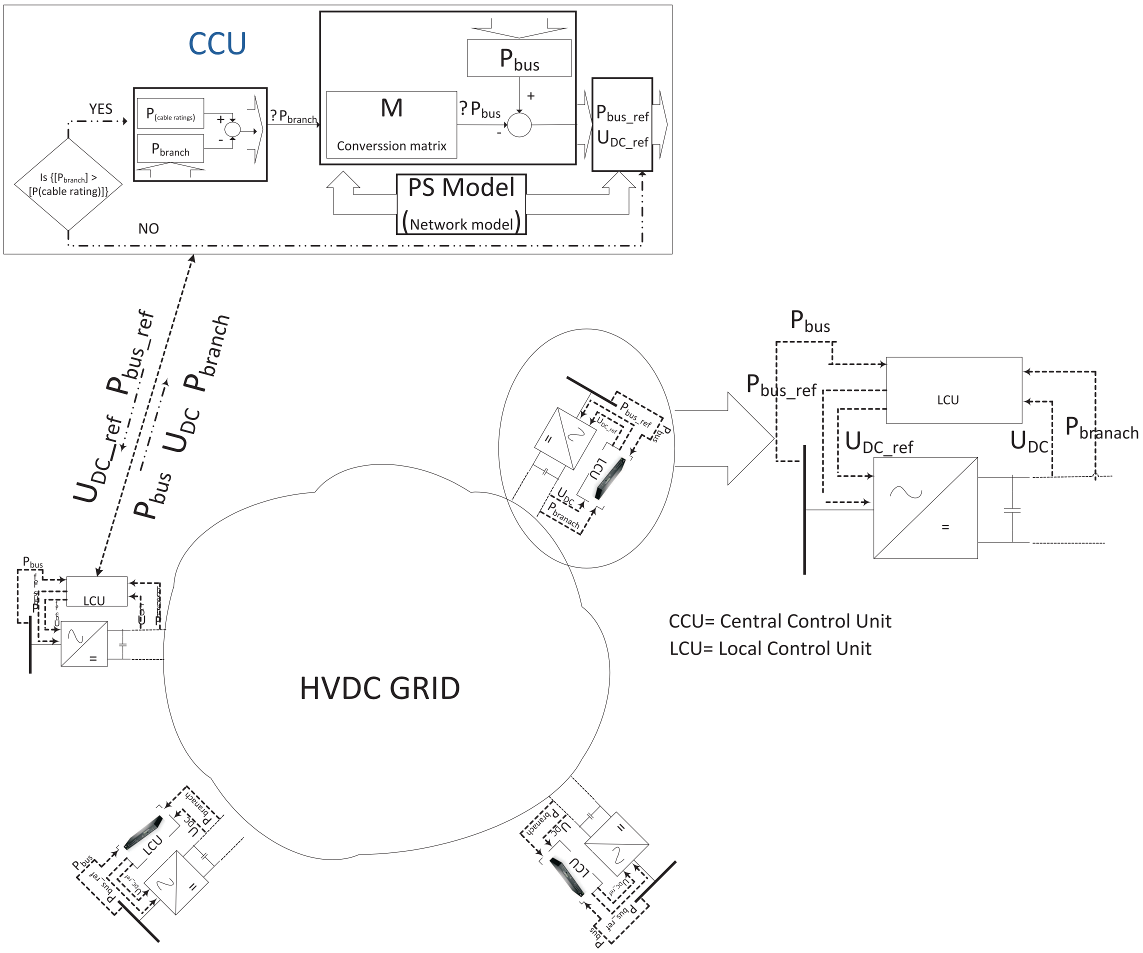

Figure 2.10: The architecture of the proposed control algorithm in a meshed HVDC grid; local primary controllers followed by the central secondary controller

2.3 Component cost estimation

Establishing a method to estimate the cost of components in a good way is crucial to quantify the values resulting from system expansion. The total cost of a VSC HVDC transmission system is mainly composed of the cost of transmission cables, the cost of VSC converters and installation cost [16], [37]. In this section, the methods used to estimate the components are established.

2.3.1 Cost of cables

Cost of cables constitute a major part of the total investment cost of an HVDC grid. ENTSO−E (European Network of Transmission System Operators for Electricity) has summarized different costs of HVDC transmission cables in one of its report [16]. Table 2.3 shows average costs of some of the subsea cables presented in the report. Note that the costs are in euro (€) per meter of cable supplied excluding installation cost.

Table 2.3: Cost of extruded subsea HVDC cable for 320 kV voltage level

Cross-sections Area (mm^2)	ENTSO−E Cost (€/m)
1200	345−518
1800	345−575
2000	403−660

It is often difficult to get the cost of cables used in a specific study. This is because cost data is often a sensitive information for an industry and it is often obtained from commissioned projects. This makes it important to develop an expression that can be used to estimate cost of a cable for a given voltage and power ratings. Such an expression to calculate the cost of an HVDC cable is developed in [38], [39], which is formulated as

$$C_{SEK}^{cbl} = A_p + B_p S_n \tag{2.14}$$

where $Cable\_Cost$ is the unit cost of a cable in a bi-pole configuration in SEK/km, S_n is the rated power of the bi-pole configuration in $watt$, and A_p, B_p are constants related to specific system voltage. For a voltage level of ±320 kV, the parameters are given as $A_p = 2x10^6$ and $B_p = 0.006$ [38], [39].

By using (2.14), the costs of some of the submarine cables presented in [17] are estimated. Table 2.4 shows the comparison of the costs of cables from the ENTSO−E report and the equivalent estimated cost of the cables from the report in [17] calculated using (2.14). The results in the table show that the relation in (2.14) can fairly be used to estimate the cost of HVDC transmission cables having a voltage rating of ±320kV. Note that the relation in (2.14) considers the cost of cables in SEK. To convert SEK into €, an exchange rate of 9.5 SEK per € is assumed, which is an average exchange rate during the year 2007 to 2016. Note also that while the power in the table is for bi-pole, the cable cost values are for one pole.

Table 2.4: Cost of extruded subsea HVDC cable for 320 kV voltage level

Cross-sections Area (m^2)	$S_n(Watt)$ (bi-pole set-up)	ENTSO−E cost (€/m)	Estimated cost (€/m)
1200	$943x10^6$	345−518	403
1800	$1190x10^6$	345−575	481
2000	$1272x10^6$	403−660	507

2.3.2 Cost of VSC

The cost of VSC is another important component of the total cost of an HVDC transmission system. The study made in one of the European Commission projects, called REALISEGRID [37], has developed a relationship between the cost of a VSC as a function of power rating as can be seen in Figure 2.11. The relationship in the figure is formulated as

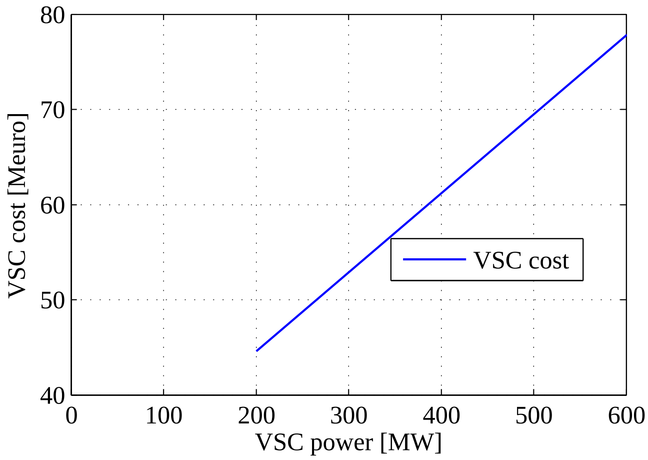

Figure 2.11: Cost of VSC converter as a function of power rating

$$C^{vsc}[Meuro] = 0.083P[MW] + 28 \tag{2.15}$$

where $Cost$ is the cost of the VSC in M€ and P is the rated power of the converter in MW [40]. Figure 2.11 shows how the cost of the VSC converter changes as a function of power.

In order to verify the validity of the VSC cost model in (2.15), the cost of a VSC presented in the ENTSO-E report are used [16]. The cost of VSCs presented in the report include the cost of AC switch yard stations excluding the cost of platforms [16]. Table 2.5 presents the comparison of the costs of VSC from ENTSO-E and the corresponding estimated costs of the VSC using the model in (2.15). The results show that the model can be used to make a good estimate of the cost of VSC especially when the voltage levels are above 320 kV. Hence, this relation can be used to fairly estimate the cost of the VSC considered in this study which have a voltage level of ±320 kV (640 kV).

Table 2.5: Comparison the cost of VSC from ENTSO-E and the corresponding cost estimated by the relation in (2.15)

Converter Technology	Power(MW)	Voltage(kV)	ENTSO-E cost (M€)	Estimated cost (M€) using (2.15)
VSC	500	300	$75 - 92$	69.5
VSC	850	320	$98 - 105$	98.55
VSC	1250	500	$121 - 150$	131.75
VSC	2000	500	$144 - 196$	194

2.3.3 Installation cost of the system

According to the report from ENTSO-E in [16], the cost of installation varies greatly in the range of 230 to 977.5€ per meter. Some of the factors affecting this price are the market conditions for specialist vessels, the location of cable installation relative to the supplier′s manufacturing facilities, the type of cable and its burial depth, the number of cables and the configuration and the rating of the cable and its size. In this thesis, an average installation cost of 604€ per meter is used.

2.3.4 Component cost as a function of cable thickness

In this thesis, a list of VSC HVDC cable data from a manufacturer data base is used. In Ref. [17], submarine cable data of different voltage levels (±80kV, ±150kV, ±320kV) are given. Table 2.6 shows the specification of submarine cable technologies suitable for a tropical climate for a voltage level of ±320kV.

Table 2.6: Bipolar VSC HVDC cable technologies for tropical climate at a voltage level of ±320kV

Area (mm^2) per pole	Resistance (Ω/km, 20^0C) per pole	Rated current(A) per pole	Rated power(MW) per bi-pole
95	0.193	338	216
120	0.153	387	248
150	0.124	436	279
185	0.0991	496	317
240	0.0754	580	371
300	0.0601	662	424
400	0.0470	765	490
500	0.0366	887	568
630	0.0283	1030	659
800	0.0221	1187	760
1000	0.0176	1355	867
1200	0.0151	1474	943
1400	0.0126	1614	1033
1600	0.0113	1745	1117
1800	0.0098	1860	1190
2000	0.0090	1987	1272
2200	0.0080	2086	1335
2400	0.0073	2198	1407

Note that the cable data given Table 2.6 are discrete values. In order to easily use the cable data in the analysis of different cases, it is useful to express the different parameters of the cable as a function of the cable thickness in a continuous form. For this purpose, a curve fitting technique is used to develop the relationship between the different parameters of the cable technologies and the corresponding thickness.

Figure 2.12 shows the result of curve fitting of the unit resistance of the cable data in Table 2.6 as a function cable thickness. Figure 2.12(a) shows the actual unit cable resistance and the estimated cable resistance using the power function shown in the figure. Figure 2.12(b) shows the residual error with no specific pattern indicating a good fit. Note that the residual error is calculated by dividing the difference between the actual and the estimated cable resistance with the standard deviation of the differences.

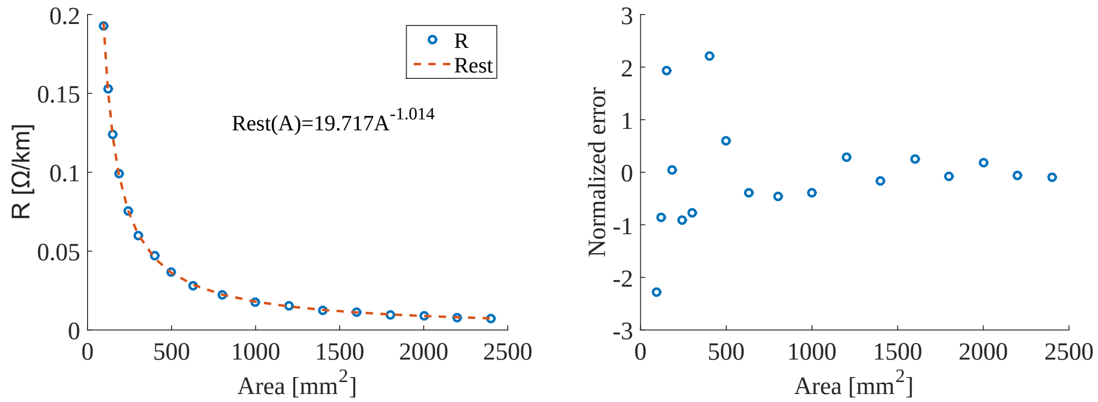

(a) (b)

Figure 2.12: Curving fitting of resistance as a function of cable thickness function (a) resistance and estimated resistance (b) normalized residual error

Figure 2.13 shows the curve fitting of the conductance of the cables. Note that the actual conductance values are calculated by taking the inverse of the unit resistances in Table 2.6. Figure 2.13(a) shows the actual unit resistance and the estimated unit resistance by using the linear function indicated in the figure. Figure 2.13(b) shows the residual showing no specific pattern indicating that the indicated linear fit is a good one. Observe that resistance in Figure 2.12 and the conductance in Figure 2.13 are for one pole in a the bipolar configuration.

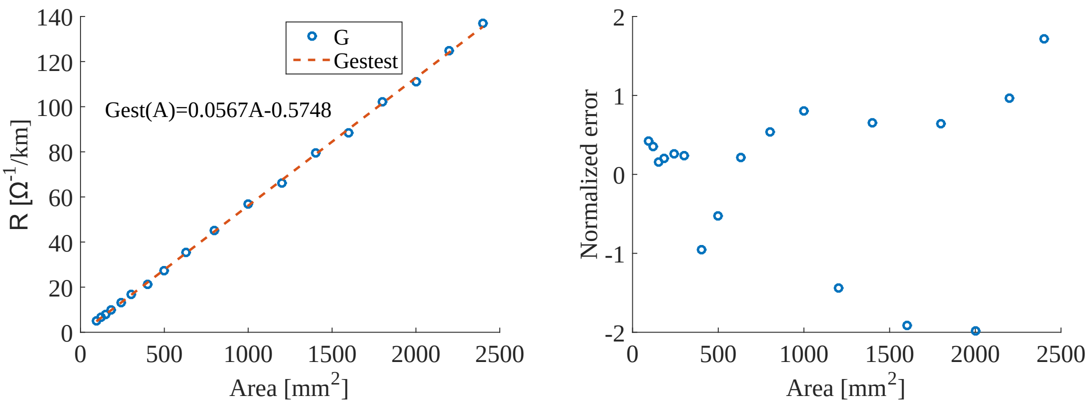

(a) (b)

Figure 2.13: Curving fitting of conductance as a function of cable thickness function (a) conductance and estimated conductance (b) normalized residual error

Similarly, curve fitting is used to express the rated current and power of the cables in Table 2.6 as a function of cable thickness. As can be seen from Figure 2.14, the power function result in a good fit. Figure 2.14(a) shows the actual and the estimated current rating of the cables as a function of cable thickness and Figure 2.14(b) shows the actual and the estimated power rating of the cables as a function of the cable thickness. Observe that current rating in Figure 2.14(a) is for one pole in the bipolar configuration whereas the rated power in Figure 2.14(b) is for the bi-pole configuration.

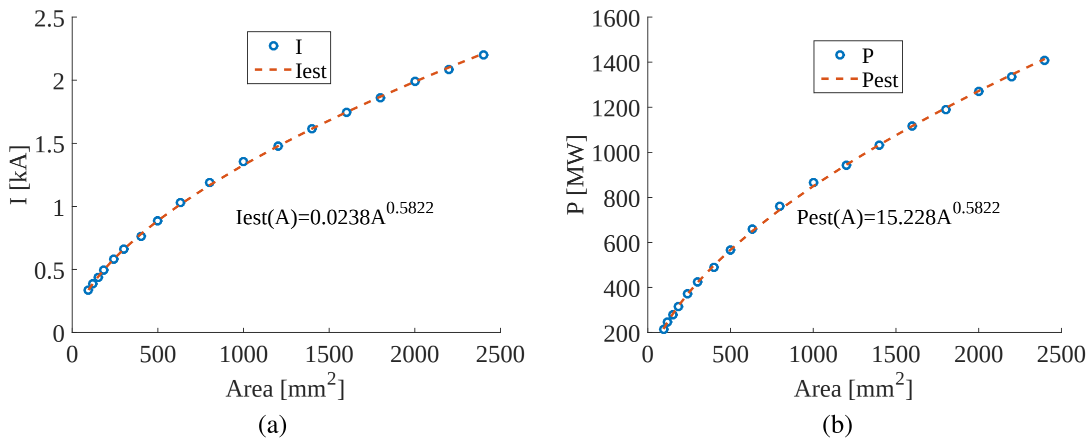

Figure 2.14: Curving fitting of (a) actual and estimated cable current (b) actual and estimated cable current ratings

Note from (2.14) that cable cost is expressed as a function of power. And in Figure 2.14(b) rated cable power is expressed as a function cable thickness. By relating the two, the cost of cable per km can be expressed as

$$C_u^{cbl} = a_0^{cbl} + c_0^{cbl} A^{a_0} \tag{2.16}$$

where $a_0^{cbl} = 0.22$ and $c_0^{cbl} = 0.01$ and $a_0^0 = 0.5822$. By using the information in Section 2.3.3, the cost of installation per km is expressed as a function of cable thickness which is formulated as

$$C_u^{inst} = a_0^{inst} + c_0^{inst} A^{a_0} \tag{2.17}$$

where $a_0^{isnt} = -0.135$ and $c_0^{cbl} = 0.013$ where the cable thickness is within the range presented in Table 2.6. Similarly, using the relation in (2.15) and the result in Figure 2.14(b), the cost of a VSC can be expressed as a function of cable thickness which is formulated as

$$C^{vsc} = a_0^{vsc} + c_0^{vsc} A^{a_0} \tag{2.18}$$

where $a_0^{vsc} = 28$ and $c_0^{vsc} = 1.26$ and $a_0^0 = 0.5822$.

Chapter 3

Modelling temporally and spatially correlated wind power

In this chapter, a summary of, ARMA based temporally and spatially correlated modelling of time series wind speed data is presented. First, the modelling and analysis of time series wind speed data at single site presented. This is followed by the modelling and analysis of wind speed time series over a large geographical area.

3.1 Background

3.1.1 Wind speed and wind power

Wind power is a function of wind speed. For a given wind speed at a WPP, the power output from the WPP is governed by a characteristic power curve of the WPP [41], [42], [43]. Figure 3.1 presents different power curve models developed by the TradeWind project [44].

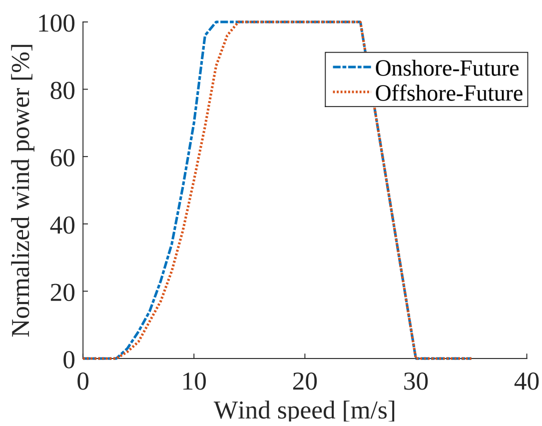

Figure 3.1: Future onshore and offshore power curve models

In the figure, turbine power curve models for future onshore and offshore application is presented. Since wind power is a function of wind speed, an important step to model wind power time series data is to model wind speed time series. Wind speed time series is stochastic in nature and some of its important characteristics are strong time correlation, periodicity and probability distribution.

There are different types of wind speed models. Some of these are the discrete Markov model [45], [46], [47] and ARMA based models [48], [41], [42], [49]. The discrete Markov model has three major problems; quantisation error, many model parameters and require a large set of time series data compared with the ARMA based model [43]. ARMA based wind speed model is a time series model which is easy to implement and does not have much of the problems of the Markov method [50], [51], [52]. In the following section, a summary of the standard ARMA based modelling procedure is presented.

3.2 Standard ARMA modelling procedure

3.2.1 Standard ARMA Model

In this section, a summary of the standard ARMA modelling procedure is presented. Interested readers are referred to [53], [54] for more detailed information. The standard ARMA model of a random process, $Y(t)$, is expressed as

$$\left(1-\sum_{i=1}^{p}\phi_i B^i\right)Y(t)=\theta_0+\left(1-\sum_{i=1}^{q}\theta_i B^i\right)a(t) \tag{3.1}$$

where p is the order and ϕ_i are the coefficients of the AR(Auto Regressive) components; B is a back shift operator where $B^iY(t)=Y(t-i)$; θ_0 is referred to as a deterministic trend term; q is the order and θ_i is the coefficient of the MA(Moving Average) component and $a(t)$ is a white Gaussian noise with zero mean and variance of σ_a^2 [53], [54].

The model in (3.1) is called the ARMA(p,p) model of order p and q. It has $p+q+2$ unknown variables; the deterministic trend term θ_0, the AR coefficients $\phi_1,\phi_2,...,\phi_p$, the MA coefficients $\theta_1,\theta_2,...,\theta_q$ and the variance of the white noise σ_a^2. The variables are calculated based on observed time series data to be modelled by using methods such as maximum likely hood estimator, a Yule-Walker estimator, a least square estimator [53], [54]. In (3.1), when $q=0$; the ARMA(p,p) model is reduced into an AR(p) model and when $p=0$; the ARMA(p,q) model is reduced into an MA(q) model.

3.2.2 Transformation

Differencing

Note that the standard ARMA model in (3.1) is developed for time series data resulting from a Gaussian and stationary process where the mean and variance of the data do not vary over time. However, time series data, such wind speed, are non-Gaussian and non-stationary in nature where the mean and variance of such data vary over time. In order to apply the standard ARMA model to a non-Gaussian and non-stationary time series data, the data has to be transformed into a Gaussian and a stationary time series data by using appropriate transformation techniques.

Let $y(1), y(2), ...y(N)$ be observed time series data originated from a non-stationary process. If the data is non-stationary; differencing could be used to transform the data into a stationary time series data. Differencing the data is formulated as

$$y'(t) = y(t) - y(t+1) \tag{3.2}$$

Note that (3.2) shows first order differencing of the data. If required, second or more orders of differencing could be used in the transformation process. The criteria for the selection of the order of differencing is trial and error.

Power transformation

For an observed time series data, $y(t)$, with a non-Gaussian distribution, the Box-Cox's power transformation can be used to stabilize the variance [53], [54]. The objective of the method is to find an appropriate transformation factor v that can transform the data to a time series data with a Gaussian distribution. The criteria for the selection of the power transformation factor is to find the value of v that minimizes the residual sum of squares which is calculated as

$$SS(v) = \sum_{t=1}^{N} \left(T(y(t)) - \widehat{m}_y \right)^2 \tag{3.3}$$

where $T(y(t))$ is a function of time and is calculated as

$$T(y(t)) = \frac{y^v(t) - 1}{vG^{v-1}} \tag{3.4}$$

and G is the geometric mean of the observed time series, which is a constant and can be calculated as

$$G = \left(\prod_{i=1}^{N} y(t) \right)^{1/N} \tag{3.5}$$

The power transformed data become $[y(t)]^v$. For a time data with non-stationary and non-Gaussian characteristics, the transformation of the data into a stationary and Gaussian time series data need be done at the same time. Since differencing can result in negative time series data, it is recommended to apply power transformation on the time series before differencing [53], [54].

Once the observed time series data is properly transformed into a stationary time series data; model identification and diagnostic checking can be applied to the stationary time series data to develop the corresponding ARMA model. The detailed procedure for model identification and diagnostic checking are discussed in [55] and [56]. Figure 3.2 shows the flow chart of the standard ARMA modelling procedure. The procedure starts by taking time series data as an input, which for instance can be wind speed. Then non-linear transformation followed by linear transformation is applied on the data (when necessary) to transform it into stationary and Gaussian time series data. Following this, the initial model identification is made for the transformed data which is followed by model parameter estimation. The first stage of diagnostic checking is made on the identified model. If the model is not ok, the model structure is updated using the information from the diagnostic checking and a new parameter estimation is made. The same process is repeated until the model is justified by the diagnostic checking.

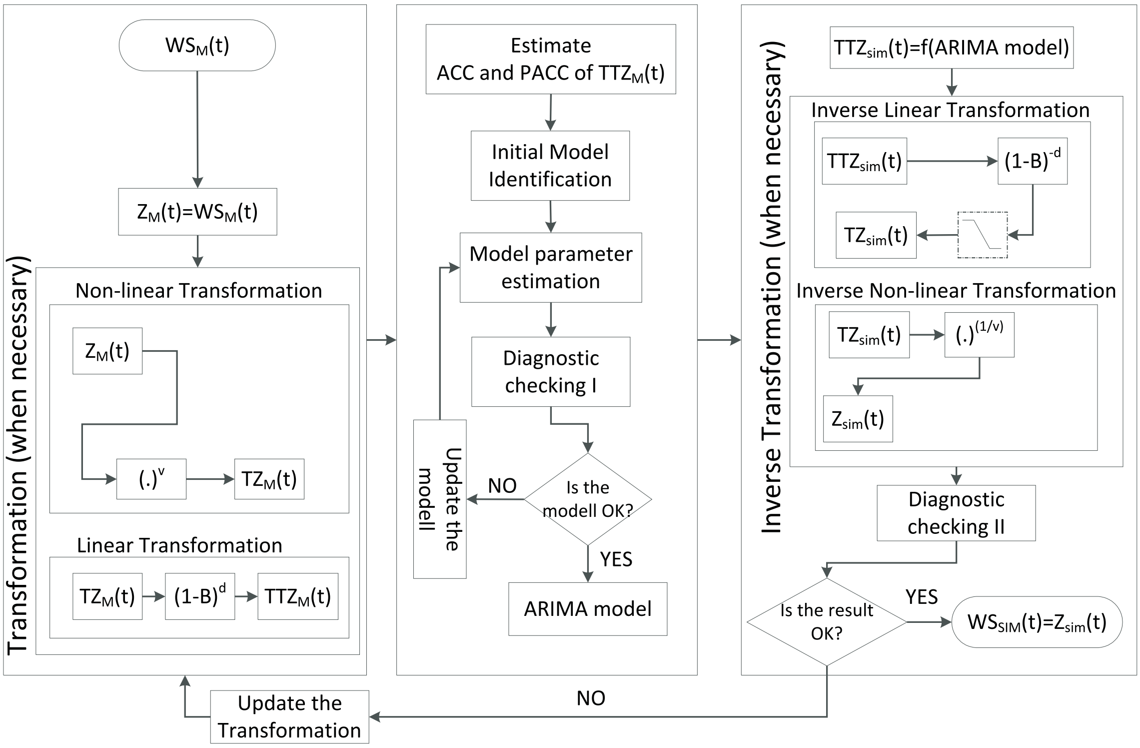

Figure 3.2: A flow chart of the standard LARIMA modelling procedure

If the model is ok, it is used to simulate time series data. The resulting time series data are inverse transformed to get the desired simulation result. The final diagnostic checking is made on the simulated time series data by comparing the simulated time series data against the measurement on the basis of the mean, variance, probability distribution and time correlation. If the comparison does not result in a good match, the process is repeated with updated values of transformation parameters and model structures until acceptable results are achieved.

3.2.3 Limitation of the standard ARMA modelling procedure

The standard ARMA modelling procedure discussed in Section (3.2.1) is used to model 10 minute average wind speed data shown in Figure 3.3. By following the standard modelling procedure step by step, it was was found that ARMA(2,2) is the model structure where the wind speed time series data is transformed using first order differencing and transformation factor of $v = 0.5$. Figure 3.4 shows some of the results generated by simulating the model. Figure 3.4(a) shows the Q-Q(Quantile-Quantile) plot of the measured and the simulated wind speed. Note that Q-Q plot is a measure of probability distribution. Figure 3.4(b) shows a comparison of the ACC(Auto Correlation Coefficient) of the measured and the simulated wind speed data. The results in Figure 3.4 clearly shows a mismatch in the characteristics of the measured and simulated wind speed data. As a result, it is concluded

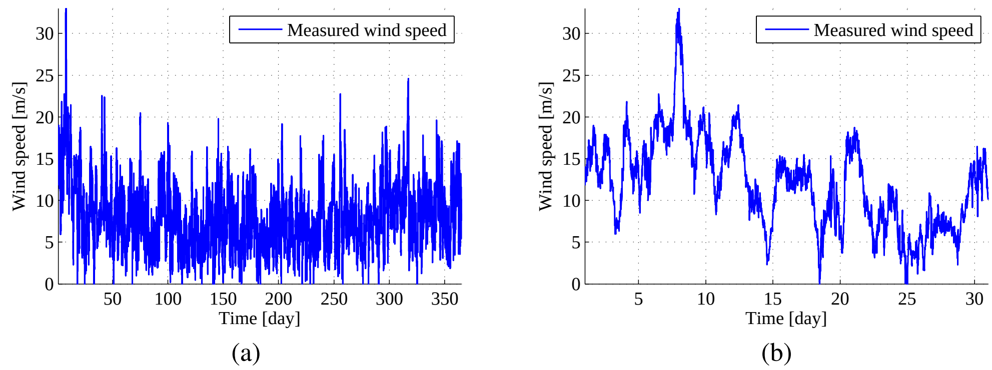

Figure 3.3: Measured 10 minute average wind speed data from Näsudden (a) Over a year (b) Over the first month of the year

in [55] and [56] that the standard ARMA modelling procedure cannot be used to model 10 minute average wind speed time series data. Hence, a modified ARMA based modelling procedure is proposed which is presented in the following section.

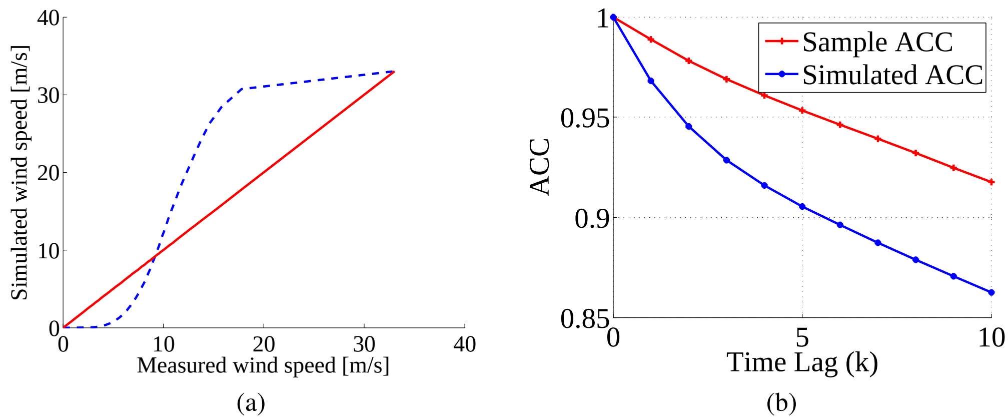

Figure 3.4: Comparison of measured simulated time series data for the verification process (a) Q-Q plot (b) ACC plot

3.3 Modified ARMA modelling procedure

3.3.1 Frequency decomposition

In order improve the limitation in the standard ARMA modelling, a modified procedure based on frequency decomposition is proposed. The proposed procedure involves first splitting the wind speed data into HF (High Frequency) and LF (Low Frequency) components. The process of frequency decomposition involves mainly four steps. The first step is determining the cut-off frequency (F_{cutoff}) which is used to split the observed wind speed data into HF and LF components. The second and the third steps are modelling the HF and LF components of the wind speed data. The final and the fourth step is combining the simulation results from the HF and LF models and comparing it with the observed wind speed data. Each of these steps are discussed in the following subsections.

Determining the cut-off frequency (F_{cutoff})

As stated before, wind speed time series data has non-Gaussian and non-stationary characteristics. According to the study in [57], the major contributor to the non-stationary characteristics of the wind speed data is the LF component of the wind speed. Based on this fact, the HF component of a wind speed data can be considered Gaussian and stationary. Hence, the F_{cutoff} can then be chosen in such a way that the HF component is Gaussian and stationary. Note that $F_{cutoff} = 1/T_{cutoff}$ where T_{cutoff} is the cutoff period.

For a time series data to be stationary, the ACC and PACC(Partial Auto Correlation Coefficient) of the residual data need to have the characteristics of a white noise; i.e. the ACC and PACC of the residual has to be within a critical limits for a large time lag greater than zero (refer to Paper I for details). Fig. 3.5 shows the ACC and PACC of the residual as a function of T_{cutoff} when the ARMA(2,0) model structure is used to model the HF component of the observed wind speed data where $v = 1$ and $d = 0$. Observe that the model structure is obtained by using the initial model identification procedure shown in Figure 3.2. As T_{cutoff} is increased from 1 day to 4 days, the ACC and PACC of the residual became closer and closer to the ACC and PACC of the white noise at higher time lags. At $T_{cutoff} = 4day$, the ACC and PACC of the residual are within the limiting values for larger time lags which indicates that the HF component at this T_{cutoff} can be assumed stationary. It is important to notice at this point that the cut-off time ($T_{cutoff} = 4day$) that emerged from this analysis is consistent with the result from the Van der Hoven spectrum [57].

Modelling the HF component

Note that at $T_{cutoff} = 4day$, the residual ACC and PACC in Fig. 3.5(b) at a lower time lag are not bounded within the limit. This indicates that the initially identified ARMA(2,0) model for the HF component needs to be modified. Following the diagnostic checking procedure described in Paper II and shown in Figure 3.2, the updated model structure for the HF components of the wind speed is found to be ARMA(6,0). Note that the residual,

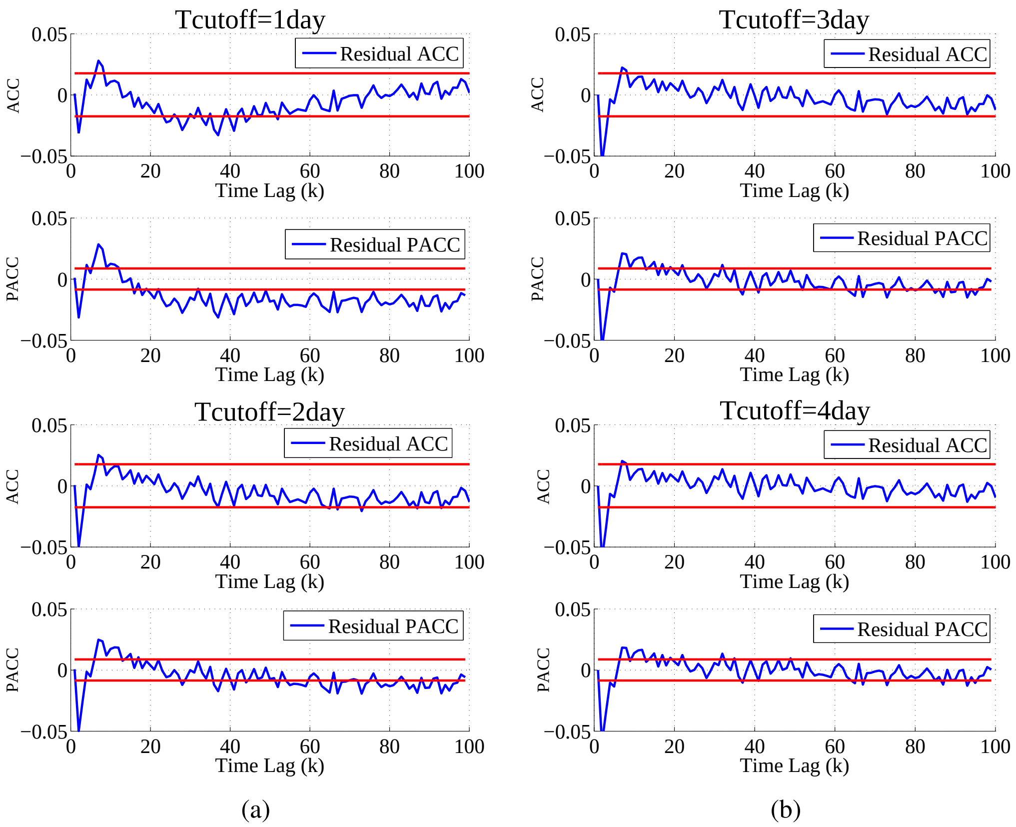

Figure 3.5: Residual ACC and PACC as a function of T_{cutoff} when an ARMA(2,0) model structure is used to model the HF component

when ARMA(6,0) is used to model the HF component, is a white noise. The result in Fig.

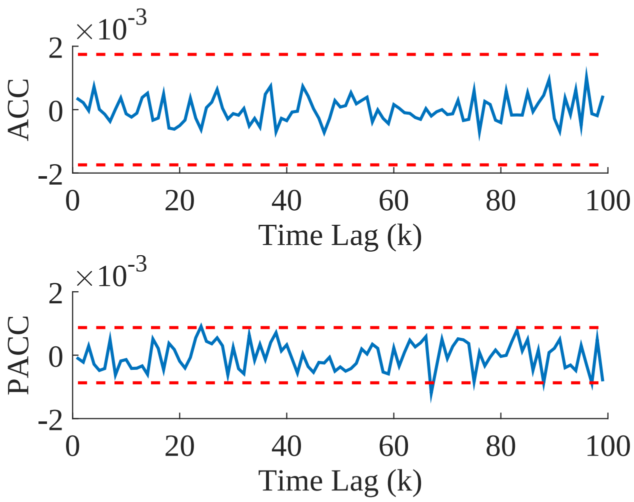

Figure 3.6: Residual ACC and PACC of the HF component when modelled using ARMA(6,0)

3.6 shows the ACC and PACC of the residual when ARMA(6,0) is used to model the HF component of the wind speed data. Note that the residuals are within the critical limits indicating the adequacy of the model.

Modelling the LF component

Once the HF component of the wind speed is determined using $T_{cutoff} = 4day$, the LF component can be determined by subtracting the HF component from the observed wind speed data. As expected, the resulting LF component is non-Gaussian and non-stationary and the corresponding ARMA model structure can be developed by following the model identification and diagnostic checking procedures described in Paper I and shown in Figure 3.2.

Before transforming and then modelling the LF component of the wind speed data, it is important to re-sample the data. Note that the sampling frequency (FS) of the measured wind speed is 144 samples per day ($FS = 144cycle/day$), which is too high compared with the maximum frequency (F_{max}) in the LF data which is 0.25 cycle per day. Note that F_{max} is the maximum frequency component in the LF data which is given by $F_{max} = F_{cutoff} = 1/T_{cutoff}$. This makes it difficult to see the temporal correlation of the data and hence the ACC and PACC of the data from which the initial model identification can be made. According to the Nyquist sampling criteria, reconstruction of a signal is possible when the sampling frequency is greater than twice the maximum frequency of the signal being sampled [58]. In order to choose the right value of the frequency to re-sample the LF component of the wind speed data, the effects of different re-sampling frequencies on the characteristics of the LF component are analysed. Hence, re-sampling frequencies of $2F_{max}$, $4F_{max}$, $6F_{max}$, $8F_{max}$ are considered in this case, which corresponds to $FS_r = 0.5cycle/day$, $FS_r = 1cycle/day$, $FS_r = 1.5cycle/day$, $FS_r = 2cycle/day$ respectively. Fig. 3.7 shows how different re-sampling frequencies alter the Q-Q plot of the LF component of the wind speed data. The results in the figure show that the re-sampled

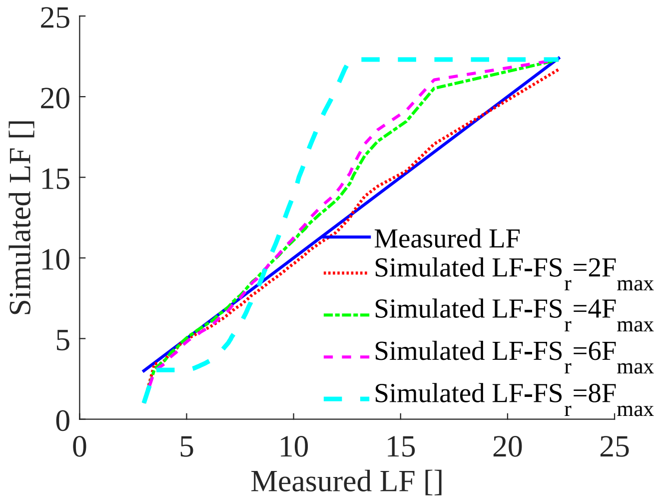

Figure 3.7: Effect of the choice of re-sampling frequency (FS_r) on the results of the LF component of the wind speed data

LF component with the re-sampling rate of $FS_r = 2 * F_{max}$ better matches the original LF component of the wind speed data.

The re-sampled LF component of the observed wind speed data is then transformed by using a transformation factor of $v = 0$ (logarithmic transformation) followed by one degree of differencing ($d = 1$). Using the modelling procedure described in Paper I and shown in Figure 3.2, the resulting model structure is identified to be ARMA(0,6). A lower order of the model introduces more error in the residual at a lower time lag (as shown in Figure 3.5 for HF modelling) and a higher order model introduces more parameters which are not desired.

Combining the results from HF and LF models to get the simulated wind speed data

Once the HF and LF components of the wind speed time series data are modelled separately, the last step is to combine the results from the two models to get the complete representation of the simulated wind speed data. Figure 3.8 shows the Q-Q plot and the ACC of the observed and the simulated wind speed time series data. Figure 3.8(a) shows the Q-Q plots and Figure 3.8(b) shows the ACC of the observed and the simulated wind speed data. The results show that the proposed ARMA modelling procedure produces simulation result with a tight match in ACC and Q-Q plot compared with the measurement. Note from Figure3.8(a) that the match in Q-Q plot (from ARMA simulation) is not tight at higher wind speed. This is because of the fact that there is little information regarding wind speeds higher that 20 m/s, as can be seen from Figure 3.3(a) to be captured by the model. Extreme wind conditions can be handled separately when needed [59]. The results in Figure 3.8 also show that the proposed modelling procedure produces much better results than the inverse PSD method, the claim which is also supported by study in the [60].

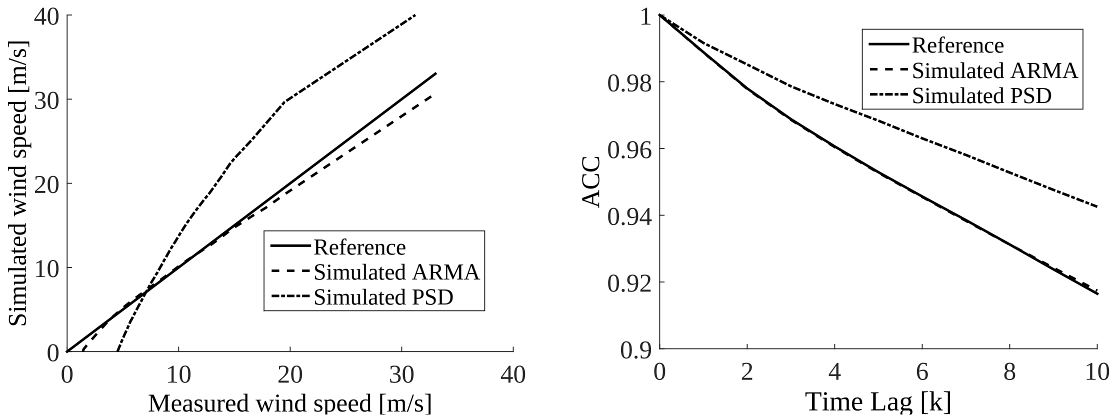

(a) (b)

Figure 3.8: Measured and simulation results of the wind speed time series data (a) Q-Q plots (b) ACC plots

Note from Figure 3.8(b) that ACC up to 10 time lag is presented, which corresponds to about 1.7 hours. Recall also that the ACC is closely related to periodic characteristics [53], [54]. Hence, from Figure 3.8(b), it is difficult to see if the proposed modelling procedure can capture the daily, monthly and seasonal characteristics of the observed wind speed data in some way. In order to show the characteristics of the ACC of the observed and the simulated wind speed data at higher time lags, the results are presented in a better way as can be seen in Figure 3.9. The results in the figure show the ACC and periodogram of the observed and the simulated wind speed. Figure 3.9(a) shows the ACC of the observed and the simulated wind speed data over a time lag of a month as a function of T_{cutoff}. As can be seen from the figure, the proposed model does capture the pattern of the observed ACC up to 500 time lags which corresponds to about 3 days. The values of ACC beyond 500 time lag are less significant since they are less than 0.2. Figure 3.9(a) also shows that the choice of T_{cutoff} affect the results and similar to the conclusion made above, the proposed method produce much better results at higher time lag compared with the spectral method.

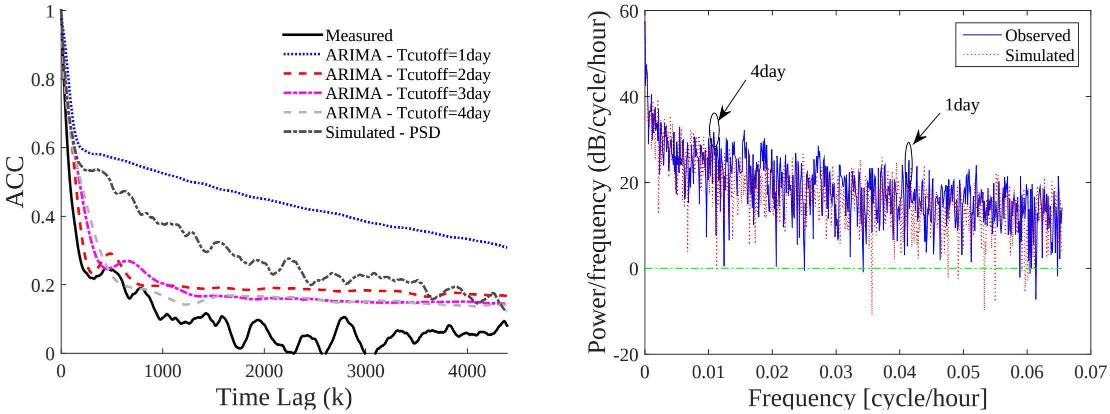

(a) (b)

Figure 3.9: Measured and simulation (a) ACC (b) periodogram

Although there is a relationship between the ACC and the periodicity of the time series data; Figure 3.9(a) shows it is difficult to see the significant periodic (daily, monthly, seasonal and so on) characteristics the time series data from the ACC alone. The best way to look at the general trend of the periodic characteristics of a time series data is to analyse the periodogram of the data. The periodogram is an estimate of the spectral density of a signal. Figure 3.9(b) shows the periodogram of the observed wind speed data and the simulated wind speed data when $T_{cutoff} = 4day$. The results in the figure show that the proposed modelling procedure can capture the general periodic characteristics of the observed wind speed data. Note from the figure that the dominant periodic characteristics of the wind speed data descends from higher to lower in a smooth way.

3.3.2 Shifting the wind speed data

Although not used in the modelling of the observed wind speed data presented in the preceding sections, shifting (adding a constant offset value to the signal) the observed time series data before transformation can sometimes improve results, as can be seen in Table 3.3.

3.3.3 Flow chart of the modified ARMA based wind speed modelling procedure

Figure 3.10 shows the flow chart of the modified ARMA based modelling procedure. This flow chart is similar to the flow chart in Figure 3.2. The only difference is the addition of the proposed transformation procedures (frequency decomposition and shifting) in Figure 3.10 in the first stage and the last stage.

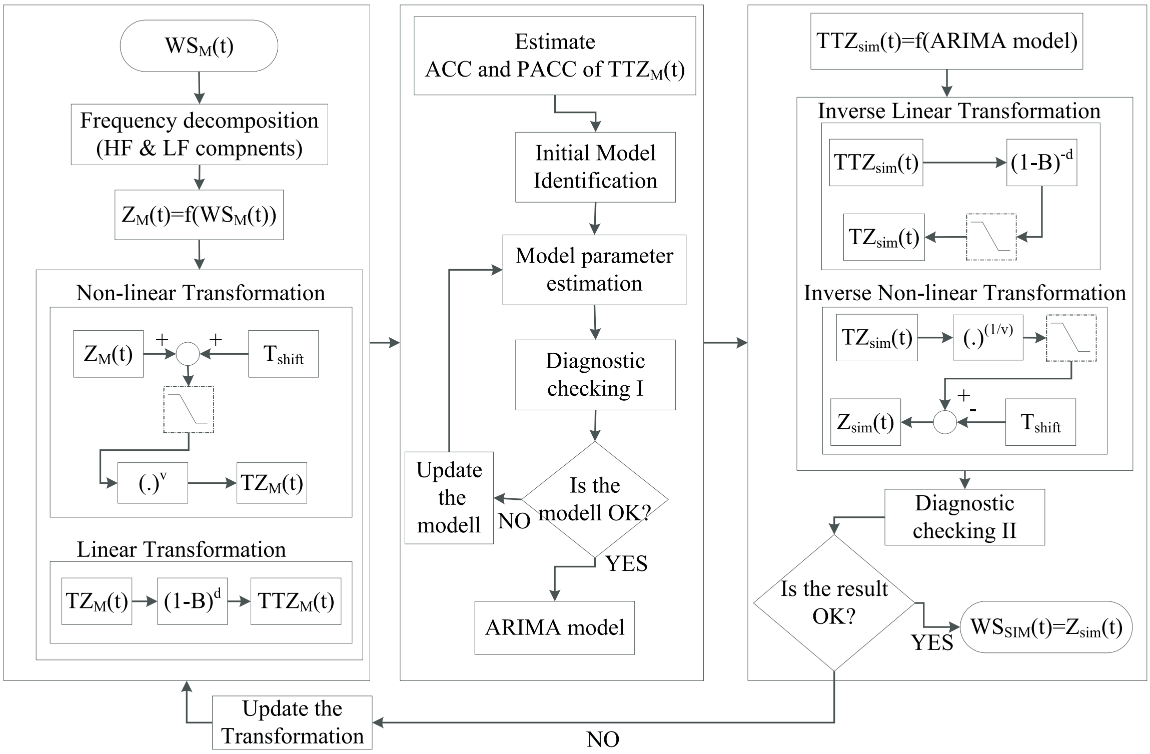

Figure 3.10: A flow chart of the modified ARIMA based modelling procedure

3.3.4 Application of the proposed modelling procedure

ARIMA(6,0,0) for HF and ARIMA(0,1,6) for LF component of observed wind speed data in the Baltic Sea area

To obtain an appropriate model structure for a given time series data is not an easy task. It requires that the procedures presented in Figure 3.10 are followed iteratively until acceptable results are achieved. Hence, it is of great importance to find a way that can be used to avoid the step to determine the model structure for a given time series data in a particular area. For this purpose, a detailed analysis of wind speed modelling at different locations over many years is made by using the proposed modelling procedure. In this analysis, some areas in the Baltic Sea region are considered.

Fig. 3.11 shows the geographical locations of the measured wind speed sites considered for analysis. The distance between the Utgrunden and the Näsudden wind site is about 150 km and the distance between Utgrunden and Tjaereborg is about 500 km. Different lengths of 10 minute average wind speed time series data are taken from each site. A five year wind speed time series, measured at a height of 100m was available at Näsudden. A three year wind speed time series, measured at a height of 38m was available from Utgrunden. A three year wind speed time series, measured at a height of 90m was available from Tjaereborg to make the analysis [61]. The average values of the wind speed data at each locations, over

Figure 3.11: Geographical locations of measured wind speed sites

the years, are given in Table 3.1.

Table 3.1: Average wind speed at different location and different years

Average wind speed [m/s]	Näsudden	Utgrunden	Tjaereborg
All year (average)	7.3116	7.4634	8.7548
Year 1	6.6068	7.2836	8.5854
Year 2	7.1334	7.787	8.8471
Year 3	7.3203	7.4938	8.8319
Year 4	7.9113		
Year 5	7.6855		

In order to show the possibility of using a generic model structure for a given wind speed time series data at a given area, the wind speed data in Year 1 from the three locations are investigated by using the proposed modelling procedure. The results from the investigation showed that the model structures ARMA(6,0) with $v = 1$, $d = 0$ and ARMA(0,6) with $v = 0$, $d = 1$ are sufficient to model the HF and LF components of the 10 minute average wind speed data from both locations. Table 3.2 presents the model parameters of the HF components of the observed wind speed data at each locations and Table 3.3 presents the model parameters of the LF components of the observed wind speed data at each locations. In the process of modelling the wind speed data from the three locations, it is observed that the use of shifting factors proved to be useful in improving the results and is considered as an added degree of freedom to be exploited in future works. Note that only positive values of the shift factors are considered in this study and the choice is made by trial and error. Note also that the model parameters in the tables are determined by following the modelling procedure presented in Figure 3.10

Table 3.2: HF model parameters of ARMA(6,0)

Data source	Model Parameters
Näsudden HF	$\theta_0 = -0.0001, T_{shift} = 0$ $\phi_1 = 0.9662, \phi_2 = -0.0571$ $\phi_3 = 0.0232\ \phi_4 = 0.0245,$ $\phi_5 = -0.0030, \phi_6 = 0.0210$
Utgrunden HF	$\theta_0 = -0.003, T_{shift} = 0$ $\phi_1 = 1.0350, \phi_2 = -0.1177$ $\phi_3 = 0.0352, \phi_4 = 0.0251$ $\phi_5 = 0.0058, \phi_6 = -0.0110$
Tjaereborg HF	$\theta_0 = -0.001, T_{shift} = 0$ $\phi_1 = 0.9227, \phi_2 = -0.0648$ $\phi_3 = 0.0659, \phi_4 = 0.0143$ $\phi_5 = 0.0149, \phi_6 = 0.0159$

Table 3.3: LF model parameters ARMA(0,6)

Data source	Model Parameters
Näsudden LF	$\theta_0 = -0.0025, T_{shift} = 5$ $\theta_1 = 0.3258, \theta_2 = 0.5157$ $\theta_3 = -0.0890, \theta_4 = 0.1951$ $\theta_5 = -0.0132, \theta_6 = -0.0520$
Utgrunden LF	$\theta_0 = 0.0003, T_{shift} = 10$ $\theta_1 = 0.4008, \theta_2 = 0.5747$ $\phi_3 = 0.0352, \phi_4 = 0.0251$ $, \phi_5 = 0.0058, \phi_6 = -0.0110$
Tjaereborg LF	$\theta_0 = 0.00025, T_{shift} = 5$ $\theta_1 = 0.2029, \theta_2 = 0.7413$ $\theta_3 = -0.0986, \theta_4 = 0.2570$ $\theta_5 = -0.0433, \theta_6 = -0.2016$

From the analysis made in this section, it can be concluded that, if one has a 10 minute average wind speed data from the Baltic Sea area (different from the ones considered above) and want to identify the model structure for the given wind speed data using the proposed modelling procedure, it could be sufficient to use the proposed model structures.

A common model to simulate wind speed at adjacent locations

The wind speed models developed so far involves measurements. However, measured wind speed data are not available at all places of interest. Hence, it is of great importance to develop a model that can be used to simulate wind speed data with *acceptable* properties at places where there are no measured wind speed time series data. The key to this is to define the term *acceptable* and in order to define it, it is important to study the variability of model parameters and relevant properties of measured wind speed data from place to place and from time to time.

In order to study the variability of the model parameters (both HF and LF model parameters) as a function of location and time, the wind speed time series data from Näsudden, Utgrunden and Tjaereborg are investigated, which are all located close to the Baltic Sea region. Note that the wind speed models developed so far are based on measured wind speed data over one year. To see the variability of the model parameters from year to year, wind speed data over many years are considered.

Fig. 3.12 shows the model parameters of the wind speed data from Utgrunden over different years. Fig. 3.12(a) shows the parameters of the HF components and Fig. 3.12(b) shows the parameters of the LF components. Note that there are similar patterns in both the HF and LF model parameters. For the HF components, the model parameters from year to year are almost the same. However, there is a slight variation in model parameters of the LF components from year to year. Although they are hundreds of kilometers apart,

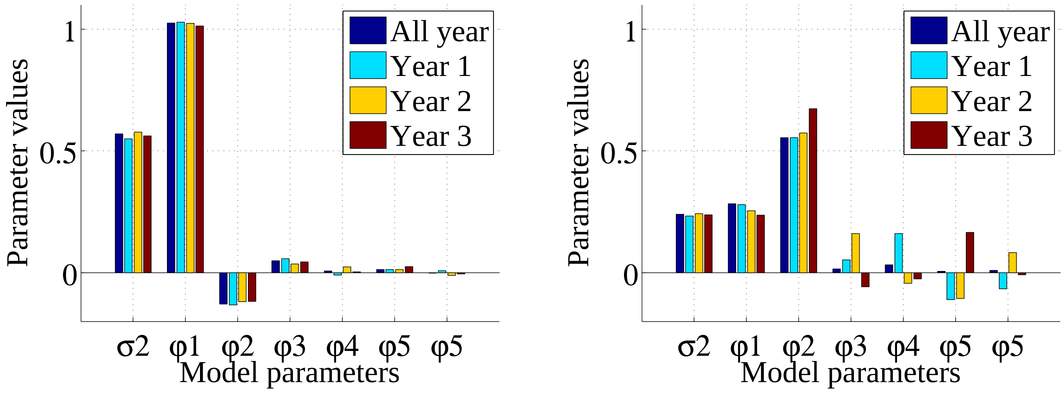

(a) (b)

Figure 3.12: Annual variability of model parameters when wind speed data from different year are considered at Utgrunden (a) HF (b) LF component

similar results are observed when analysing wind speed time series data at Näsudden and Tjaereborg, which are discussed in Paper I in details.

It is worth pointing out two important points from the above results. The first point is that the model parameters, especially that of the HF components, are not affected that much when measurement data changes from year to year at a given location. The second point is that by comparing the model parameters at Näsudden and Utgrunden, it is observed that there is a similar pattern in model parameters with a slight difference in the magnitude of the model parameters. This is an interesting observation and it can be used as a basis to use a model developed at one location to simulate wind speed time series at a nearby location. To develop the observation further, it is important to study the variability of wind speed characteristics from year to year. It is true that average values, variance, time correlation and probability distribution of wind speed time series data varies from year to year [47]. Hence, if a wind speed model developed at a given location can produce a simulated wind speed data at a nearby location with the expected annual variation at the nearby location, then it is fair to say that it is acceptable to use the wind speed model to simulate wind speed data at the nearby location.

Figure 3.13 shows the variation of the relevant characteristics of the measured wind speed data from year to year at Näsudden. Figure 3.13(a) shows the annual variation in ACC of the measured wind speed time series data and Figure 3.13(b) shows the annual variation in CDF of the measured wind speed time series data. This is the expected annual variation of the characteristics in this area and can be used as a basis to check if the simulated wind speed time series data at this location, by using the wind speed model at another location, is acceptable or not.

In order to show the possibility of simulating wind speed time series data at different locations in the Baltic Sea region using a model developed at a given location; the model and model parameters developed at Utgrunden, which are presented in Fig. 3.12, are used to

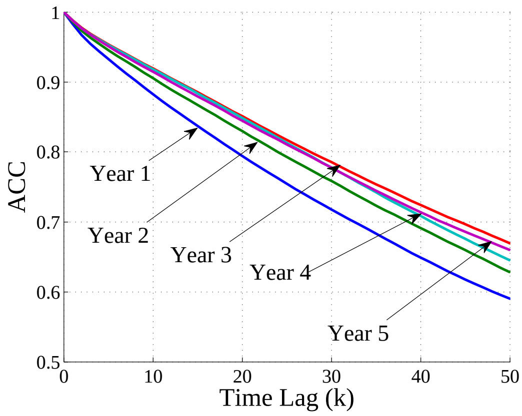

(a)

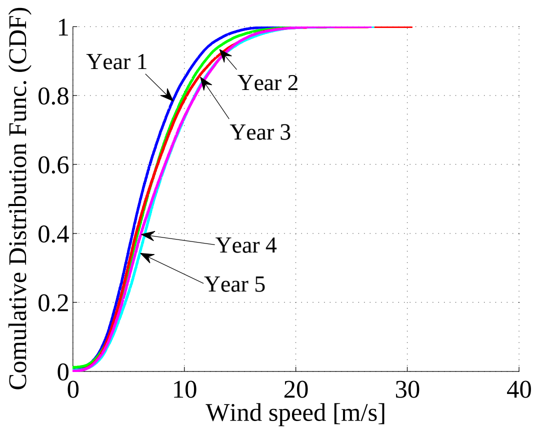

(b)

Figure 3.13: Annual variability of relevant characteristics of wind speed time series data (a) ACC (b) CDF

simulate the wind speed data at Näsudden. The actual values of the model parameters are given in Table 3.4 and 3.5. Model M1 stands for the model developed by using all year (three years) data at Utgrunden, similarly model M2 is associated with Year 1 data, M3 with Year 2 data and M4 with year 3 data. Table 3.4 shows the model parameters of the HF components of the wind speed data and Table 3.5 shows the model parameters of the LF components of the wind speed data at Utgrunden.

Table 3.4: LF model parameters

	M1	M2	M3	M4
σ^2	0.5697	0.5493	0.5776	0.5617
ϕ_1	1.0247	1.0288	1.0232	1.0132
ϕ_2	-0.1291	-0.1316	-0.1188	-0.1182
ϕ_3	0.0491	0.0576	0.0357	0.0448
ϕ_4	0.0069	-0.0098	0.0235	0.0029
ϕ_5	0.0136	0.0126	0.0128	0.0246
ϕ_6	-0.0013	0.0079	-0.0106	-0.0047

Table 3.5: LF model parameters

	M1	M2	M3	M4
σ^2	0.2395	0.2325	0.2425	0.2376
θ_1	0.2832	0.2795	0.2539	0.2362
θ_2	0.5549	0.5547	0.5736	0.6733
θ_3	0.0156	0.0525	0.1602	-0.0582
θ_4	0.0322	0.1603	-0.0429	-0.0254
θ_5	0.0064	-0.1111	-0.1061	0.1653
θ_6	0.0097	-0.0662	0.083	-0.0081

In order to simulate wind speed data at Näsudden by using the models developed at Utgrunden, it is assumed that the average wind speed at Näsudden is known or given. Fig. 3.14 shows the properties of the simulated wind speed data at Näsudden produced by using different models developed at Utgrunden. Note that, to produce the results presented in Fig. 3.14, T_{shift} and θ_0 are set to zero to simulate the HF components of the wind speed. Similarly, while simulating the LF components of the wind speed data, θ_0 is adjusted in such a way that the average wind speeds at Näsudden, presented in Table 3.1, are achieved. Fig. 3.14(a) shows the comparison of the measured wind speed data during Year 1 at Näsudden with the simulated data produced using different models developed at Utgrunden in terms of ACC and CDF. Similarly, Fig. 3.14(b) shows the comparison of the ACC and

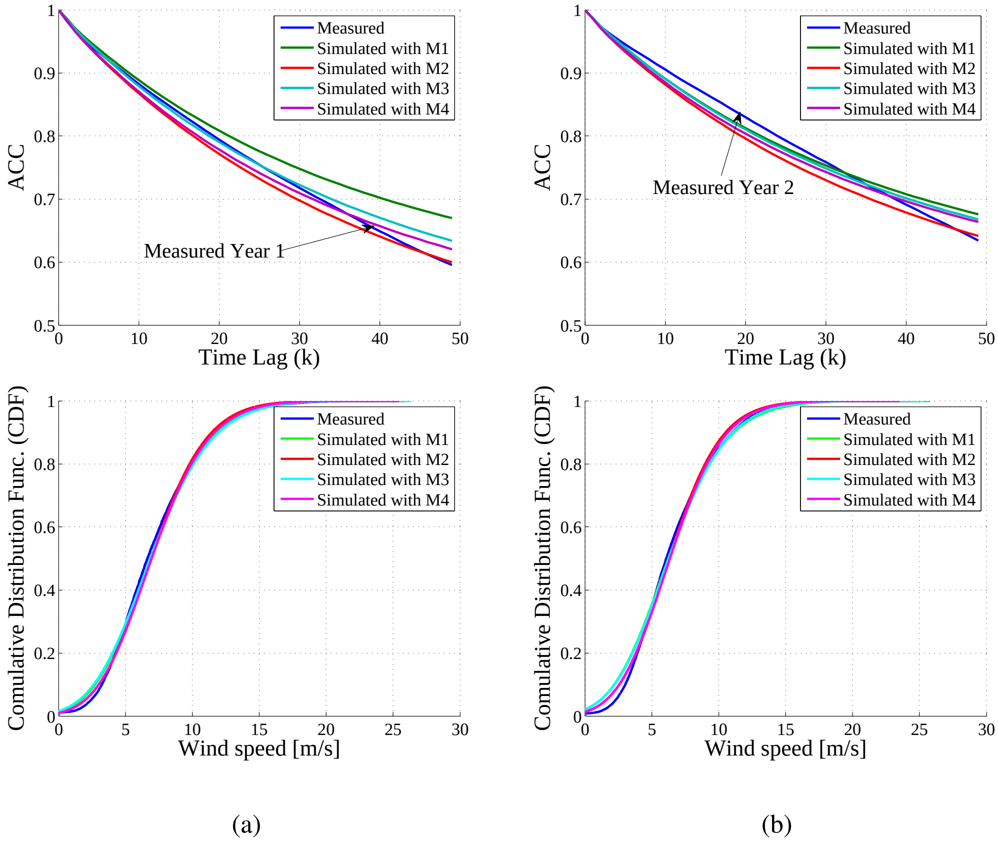

Figure 3.14: The deviation of the ACC and CDF of the simulated wind speed data from the measured wind speed (a) Näsudden Year 1 (b) Näsudden Year 2

CDF of the measured wind speed data during Year 2 at Näsudden and the ACC and CDF of the simulated wind speed data generated with different models from Utgrunden.

As can be seen from the results in Fig. 3.14, the variation of the characteristics of the simulated wind speed data around the measurement is within the expected range compared with the variation presented in Fig. 3.13. Similar result is observed when analysing Year 3, Year 4 and Year 5 wind speed data at Näsudden. From this, it can be concluded that, in places where there are no measured wind speed time series in the Baltic Sea region, one can consider to use the model parameters presented in Table 3.4 and 3.5 to simulate wind speed time series with the desired average wind speed.

3.4 Modified VARMA modelling procedure

Similar to the standard ARMA based modelling procedure which can be used to model a one dimensional data from a stationary and Gaussian process; the standard VARMA(Vector ARMA) modelling procedure can be used to model spatially and temporally correlated multi dimensional time series data originated from a stationary and Gaussian process. A detailed analysis of modelling and simulation of VARMA is presented in Paper II.

The standard VARMA modelling procedure is similar to the standard ARMA modelling procedure. Recall that the ARMA modelling procedure has three main stages. The first stage is the transformation stage where the observed input time series data is transformed into a stationary and Gaussian time series data. The second is model identification stage and the last stage is the diagnostic checking stage. As noted in the modified ARMA modelling procedure, the main challenge lies at the transformation stage. Recall that two main transformation techniques are presented in the standard ARMA modelling procedure; differencing and power transformation. Differencing is aimed at transforming a non-stationary time series data into a stationary time series data where as power transformation is aimed at transforming non-Gaussian time series data into a Gaussian time series data. It is concluded that differencing alone cannot be used to transform a 10 minute average wind speed data, which is non-stationary, into a stationary time series data. To overcome the challenge, frequency decomposition technique is introduced to form the modified ARMA modelling procedure.

Similar to the standard ARMA modelling procedure, the main tools of transformation in the standard VARMA modelling procedure are differencing and power transformation. However, for a multi dimensional hourly average data wind speed data considered in this study, it is observed that the attempt to apply differencing or frequency decomposition to transform the data into a stationary time series data proved to be unsuccessful. Hence, a transformation mechanism that removes the diurnal or seasonal characteristics from the wind speed data to form a stationary time series data is introduced in the modified VARMA modelling procedure.

Suppose a time series **y[t]** from K different sites (where **y[t]** $= [y_1[t], y_2[t], ...y_K[t]]^T$) has a non-Gaussian distribution; the Box-Cox's power transformation can be used to transform the data into a Gaussian time series data, which is given as **Ty[t]** $=$ (**y[t]**)^v [48].

Once the original non-Gaussian time series data, **y[t]**, is transformed into a Gaussian data, **Ty[t]**, the next step is to transform the resulting non-stationary time series data, **Ty[t]**, into a stationary time series data, **TTy[t]**. Recall that a time series data is non-stationary if the mean and variance of the data varies over time. Hence, the non-stationary time series data can be transformed into a stationary time series data by removing the diurnal and seasonal or any other periodic trends as

$$TTy_s[t] = \frac{Ty_s[t] - \mu_s^p}{\sigma_s^p} \tag{3.6}$$

where $TTy_s[t]$ is the resulting 'stationary' time series data at site s; $Ty_s[t]$ is the transformed Gaussian time series data at site s; μ_s^p and σ_s^p are the mean and standard deviation of the transformed time series data, $Ty_s[t]$, over a certain period p where p could be daily, weekly, monthly or any other periodic trend that can produce the desired results [62], [48].

The other difference in the VARMA modelling procedure, compared with the ARMA modelling procedure, is the use of Cross-Correlation Coefficient (CCC) in addition to ACC in model verification process. Details can be found in Paper II [63].

3.4.1 Applications of the modified VARMA

In this section, the application of the proposed VARMA based modelling procedure to model temporally and spatially correlated wind speed time series in the North Sea and the Baltic Sea area is discussed. Fig. 3.15 shows the geographical sites investigated. The chosen sites are located where there are either wind farms in operation or sites recognized as potential wind farm sites according to Ref. [64] and [65]. Since there is a limited access to time series wind speed data in the areas of interest, a synthetic wind speed data from NASA is used as an input to the modelling procedure [66]. The synthetic wind speed time series are hourly average values at a height of 50m. Note that this height is almost half of the height of the wind turbine expected in the area of interest. Hence, it is assumed that the corresponding wind speed time series at higher height can be calculated using the wind profile power low [67]. Table 3.6 shows the names of the sites and the corresponding

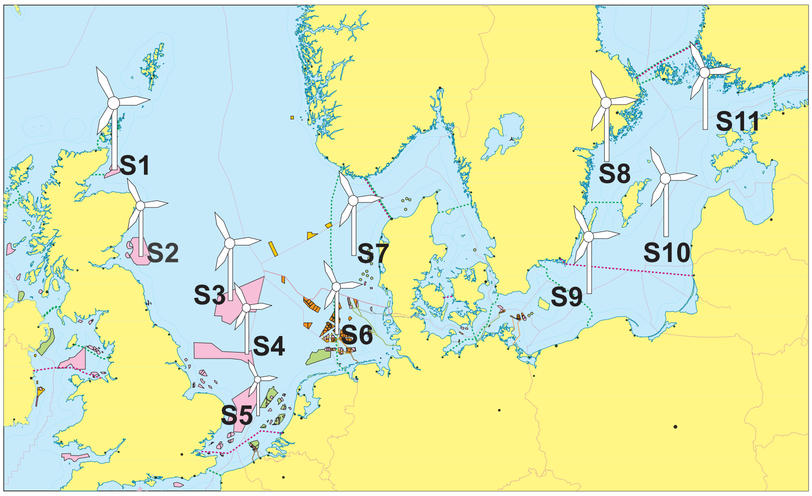

Figure 3.15: Wind speed sites in the North Sea and the Baltic Sea used for investigation

coordinates (Latitude,Longitude) pairs where the 'observed' wind speed time series are taken. The different wind speed sites presented in Fig. 3.15 and Table 3.6 are considered

Table 3.6: WInd speed sites in the North Sea and the Baltic Sea

Site	***Name***	***Coordinate (Latitude,Longitude)***
S1	Moray	(58^o,-2.6667^o)
S2	Seagreen	(56.5^o,-2^o)
S3	Dogger	(55^o,0^o)
S4	Hornsea	(53.5^o,1.3333^o)
S5	Anglia	(52.5^o,2.6667^o)
S6	German wind farms	(54.5^o,7^o)
S7	Horns Rev	(56.5^o,6.6667^o)
S8	Gustav Dahlen	(58.5^o,17.3333^o)
S9	Baltica	(55^o,15.3333^o)
S10	Baltic wind park	(56.5^o,20.6667^o)
S11	Baltic Blue	(59^o,22^o)

in this study in order to help draw a general conclusion in VARMA based wind speed modelling in the area.

Case 1 - VRAMA model of wind speed data from two sites: S1 and S2

In this section, a VARMA model structure and the corresponding model parameters of 'observed' wind speed data from two sites ($S1$ and $S2$) in the North Sea area are developed. The distance between the two sites is about 340km (1^o latitude corresponds to 111km and 1^o longitude corresponds to 63km). Fig. 3.16 shows the wind speed time series data from the two sites during a year in 2012. The average wind speed at **S1** and **S2** are about 8.5m/s and 8.1m/s respectively, and the variance of the wind speed at **S1** and **S2** are about 15.5 and 15.6 respectively.

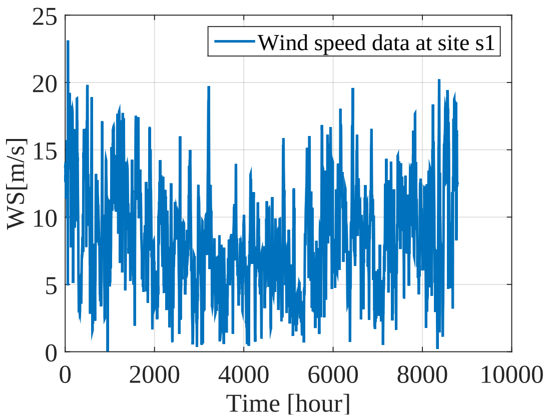

(a)

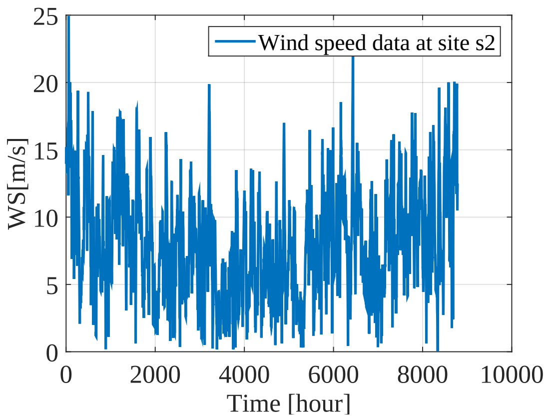

(b)

Figure 3.16: Observed wind speed time series data (a) Site **S1** (b) Site **S2**

Assume that the wind speed time series considered in this case is defined as **w[t]**=$[w_1[t], w_2[t]]$. The analysis made in Paper II shows that the transformation factor $v = 0.5$ results in the minimum residual error at both sites. Hence, the resulting transformed time series data is calculated as **Tw[t]** $= \sqrt{\textbf{w[t]}}$, which is a square root transformation.

Then the last step in the transformation procedure is to transform the non-stationary (but Gaussian time series data, **Tw[t]**) into a stationary time series data by removing the diurnal/seasonal patterns from **Tw[t]**. It is tricky to get the appropriate periodic pattern to be removed from a given time series so that the data is transformed into a stationary time series, **TTw[t]**. In this study, the choice of the periodic pattern is made based on how good the characteristics of the simulated wind speed time series (**W[t]**) are compared to the characteristics of the observed wind speed time series (**w[t]**) for the chosen periodic pattern. For this reason, a sensitivity analysis of the effect of the choice of the periodic pattern on the result is made, as can be seen in Fig. 3.17. The first row in Figure 3.17 shows the ACC and PACC of the transformed time series data (**TTw[t]**) when no periodic patterns are removed from **Tw[t]** time series. The second row in the figure shows the ACC and PACC of the time

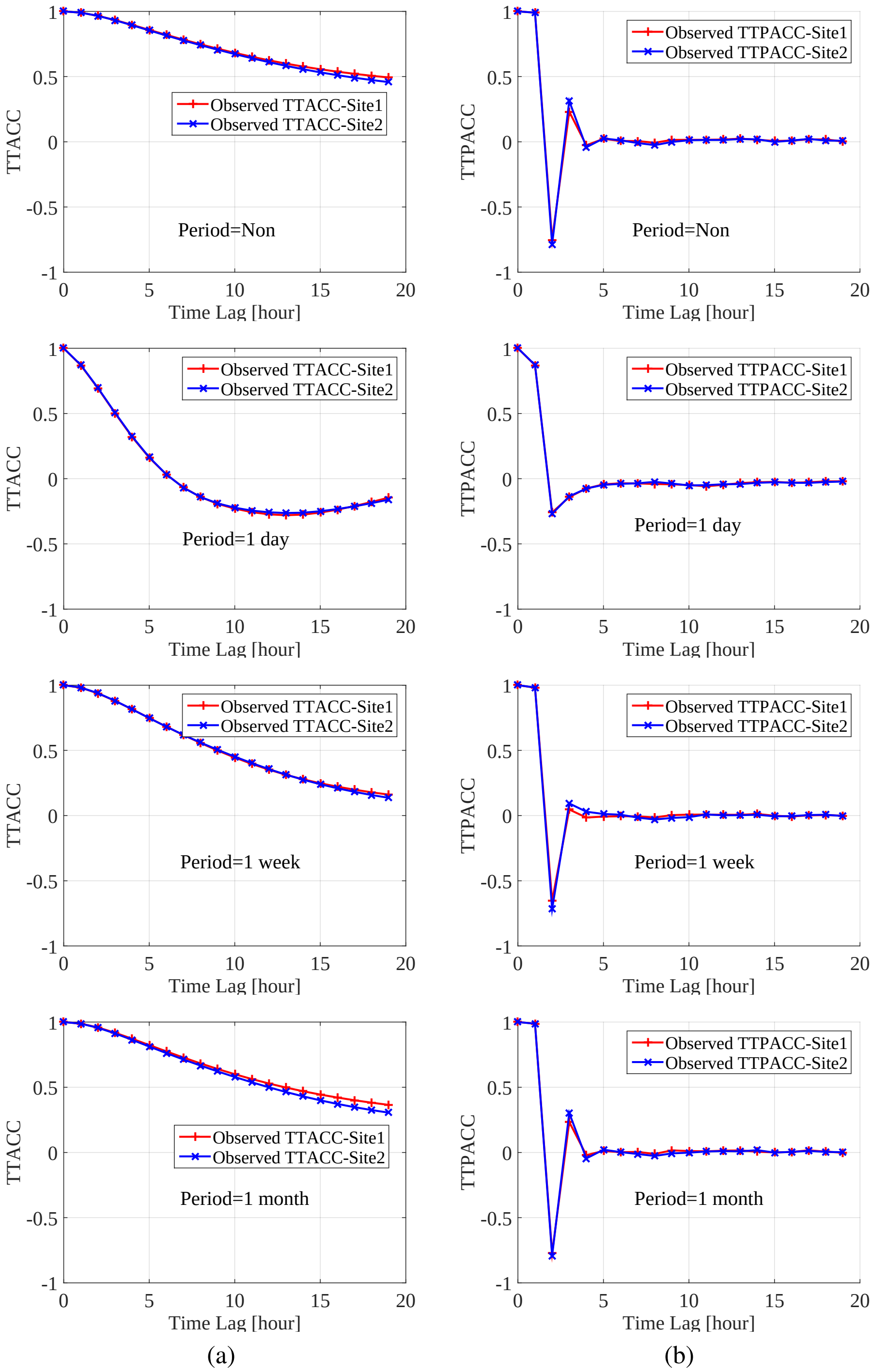

Figure 3.17: Effect of the choice of the periodic patterns on the time series data on (a) ACC and (b) PACC

series (**TTw[t]**) when the daily patterns from **Tw[t]** are removed according to the relation presented in (3.6). Similarly, the third row in Figure 3.17 shows the ACC and PACC of the transformed time series data (**TTw[t]**) when weekly periodic patterns are removed from **Tw[t]**. And finally, the fourth row in the figure shows the ACC and PACC of the transformed time series data (**TTw[t]**) when monthly periodic patterns are removed from **Tw[t]** time series according the relation presented in (3.6).

According to the model identification procedure in [53], [54], the results in Figure 3.17 suggest that the underlying VARMA model structure could be VARMA(3,0) where the order of the auto regressive coefficient (p) is 3 and the order of the moving average (q) is 0. In other words, the identified model is a vector auto-regressive model of order 3 (VAR(3)).

By using VAR(3), model parameters are estimated and the resulting model is simulated to generate time series up on which a residual test is made. Figure 3.18 shows the ACC of the residual at site 1 when different periodic patterns are considered. Similar results are observed at site 2 as well. The result on the top left of Figure 3.18 shows the ACC of the residual when no periodic patterns are removed from the transformed time series data, **Tw[t]**. This means that the **Tw[t]** and **TTw[t]** time series are the same. The results

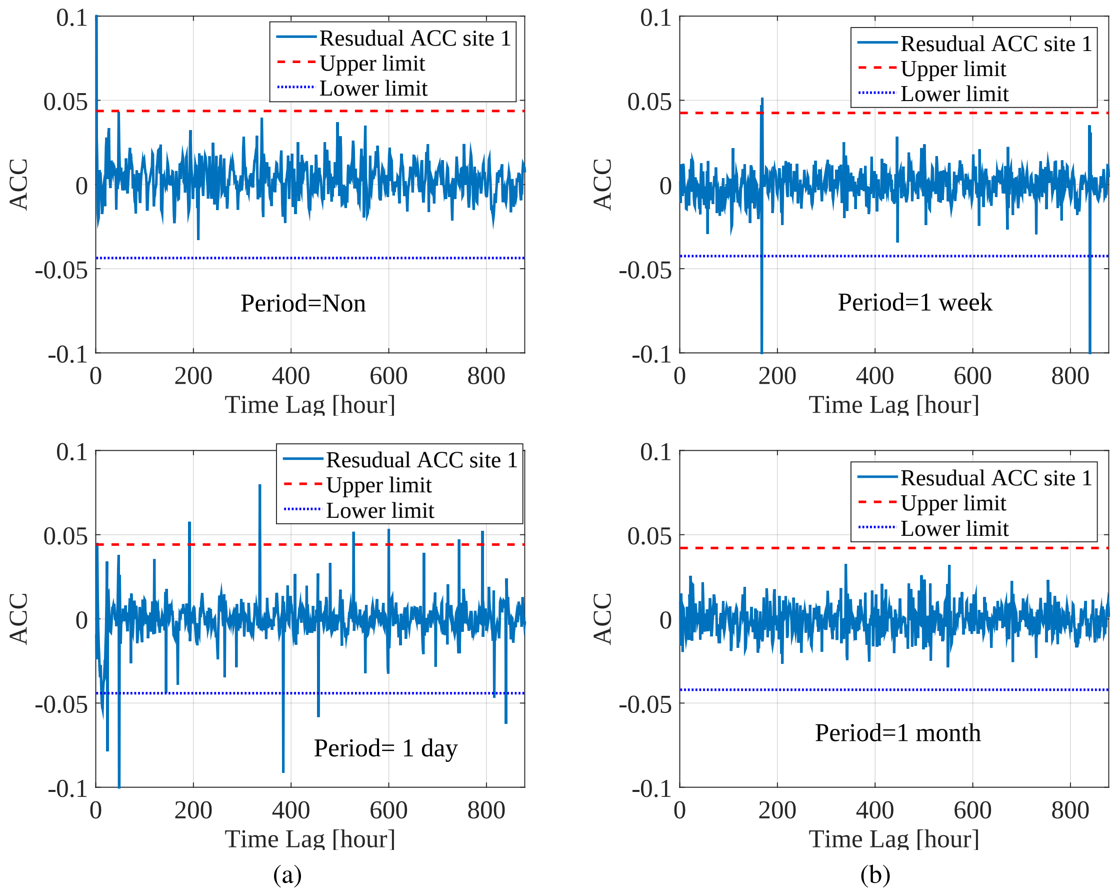

Figure 3.18: Effect of the choice of the periodic patterns on the ACC of the residual at site 1

in the bottom left, top right and bottom right of Figure 3.18 show the ACC of the residual when 1 day, 1 week and 1 month periodic patterns are removed from **Tw[t]** to form **TTw[t]**, respectively. From the results in the figure, it can be seen that better result is achieved when the monthly periodic patterns are removed from the **Tw[t]** to form **TTw[t]**.

To further justify the choice of the model structure (VAR(3)) and the periodic pattern, a diagnostic check is made on the ACC, PACC, CDF and CCC of the simulated time series data. Figure 3.19 shows the effect of the choice of periodic patterns on the ACC and PACC of the transformed time series (**TTw[t]** and **TTW[t]**, where **TTW[t]** is the transformed simulated time series data) for the identified model structure at site 1. The results in the

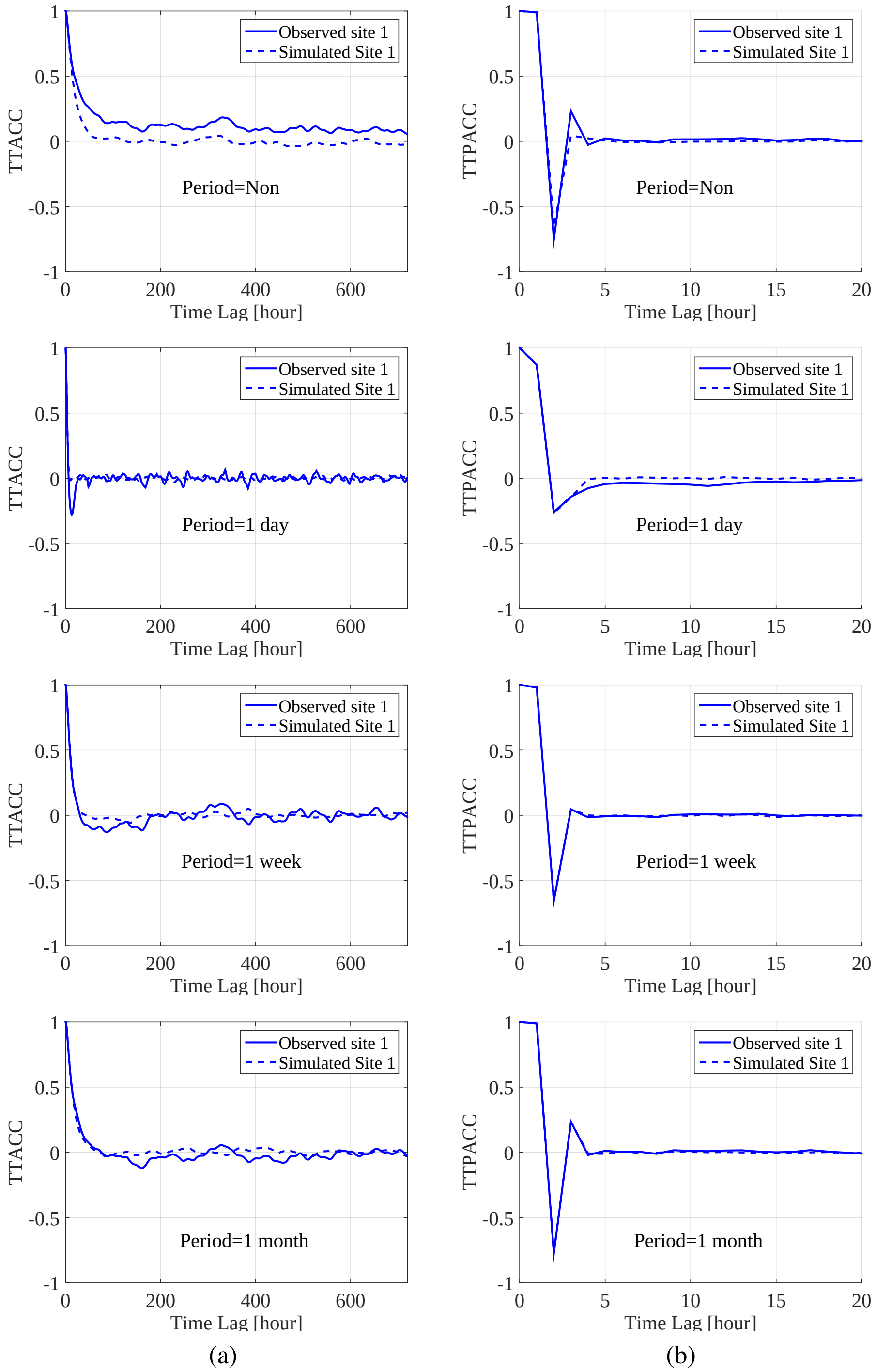

Figure 3.19: Effect of the choice of the periodic patterns in the time series on (a) ACC and (b) PACC of the transformed times series (**TTw[t]** and **TTW[t]**)

figure show that the use of 1 week and 1 month produce good results both in the transformed ACC and PACC at all time lags.

Note that the results in Figure 3.19 are the ACC and PACC of the transformed time series. Note also that **TTw[t]** and **TTW[t]** are not wind speed data, rather they are double transformed wind speed data. Hence, the real test of the goodness of the identified model

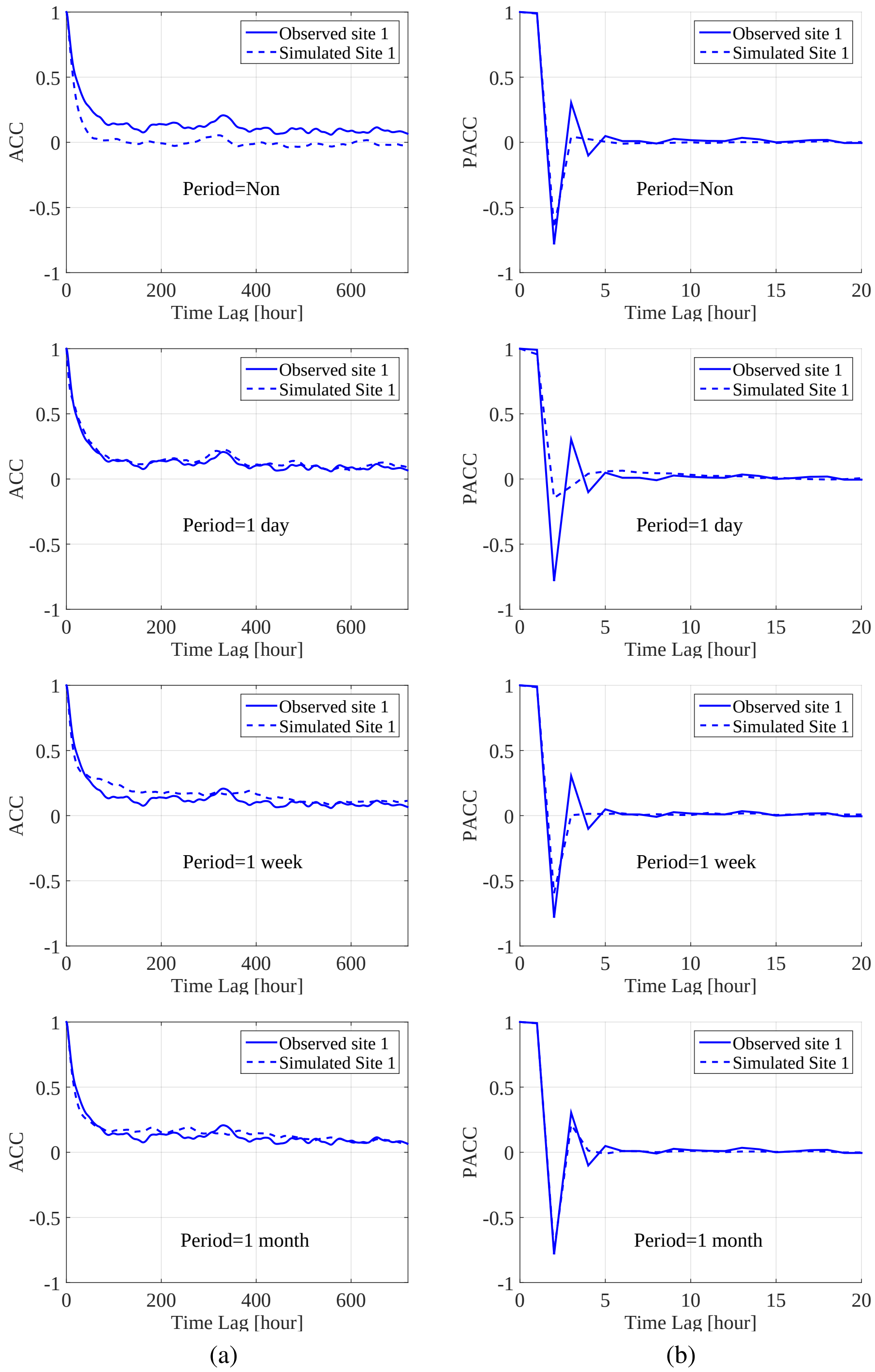

Figure 3.20: Effect of the choice of the periodic patterns in the time series on (a) ACC and (b) PACC on the wind speed data (**w[t]** and **W[t]**)

structure and the selected periodic pattern is based on a good match of the ACC and PACC of the inverse transformed **TTW[t]** (which is the simulated wind speed, **W[t]**) and observed wind speed time series data, **w[t]**. The simulated wind speed time series data at site s is calculated as $W_s[t] = (TW_s[t])^{1/v}$ where $TW_s[t] = TTW_s[t] * \sigma_s^p + \mu_s^p$ with σ_s^p and μ_s^p are the same values as the ones used in (3.6). Figure 3.20 shows the ACC and PACC of the observed and the simulated wind speed time series data, **w[t]** and **W[t]** respectively at site 1 where similar results are found at site 2 as well. The figure shows that, for the identified model structure (VAR(3)), the 1 month periodic pattern produces a much better result especially when considering the PACC which is a real measure of temporal correlation.

Apart from the good match in ACC and PACC, the identified model has to be able to produce a good match in probability distribution at each site and spatial correlation of wind speed data among multiple sites. The results in Figure 3.21 show that the choice of 1 day, 1 week and 1 month as a periodic pattern results in a good match in CDF and CCC at site 1 where similar results are found at site 2 as well. In general, the results in Figure 3.20 and Figure 3.21 show that the choice of 1 month as a periodic pattern along with the identified model structure (VAR(3) in this case) results in a good match in both the ACC, PACC, CDF and CCC.

Table 3.7 shows the model parameters of VAR(3) (Φ_1, Φ_2, Φ_3 and Θ_0) and the mean and variance of the simulated wind speed time series at both sites. From the table, it can be seen that the mean and variance of the observed wind speed at both sites are captured in a good way with a maximum percentage error of 1.5% in mean and a maximum percentage error of 5% in variance. Observe that the mean and variance in the table corresponds to the simulated wind speed time series over 5 years.

Table 3.7: Case 1: Model parameters of VAR(3) when monthly mean and variance are used in the transformation to remove the periodic patterns

Φ_1	Φ_2	Φ_3
$\begin{bmatrix} 1.9121 & 0.0366 \\ 0.0616 & 1.9822 \end{bmatrix}$	$\begin{bmatrix} -1.1827 & 0.0131 \\ -0.0324 & -1.3129 \end{bmatrix}$	$\begin{bmatrix} 0.2461 & -0.0382 \\ -0.0183 & 0.3069 \end{bmatrix}$
$\Theta_0 * 10^4$	μ_{sim}	σ^2_{sim}
$\begin{bmatrix} 0.145 \\ 0.1404 \end{bmatrix}$	$\begin{bmatrix} 8.62 \\ 8.20 \end{bmatrix}$	$\begin{bmatrix} 16.32 \\ 16.12 \end{bmatrix}$

Following the same procedure as in Case 1, three more cases (Case 2, Case 3 and Case 4), each of which consists of two wind sites, are investigated. Table 3.8 shows the distance between the sites, the mean and variance of the wind speed time series at each sites. Similar to the results in Case 1, the results of the investigations made on Case 2, Case 3 and Case 4 show that the VAR(3) model structure can be used to capture the main characteristics of the observed wind speed data, such as spatial correlation, temporal correlation and probability distribution in a good way, provided that monthly average and variance are used in the transformation to remove the periodic patterns from the time series data. Table 3.9 to Table 3.11 show the model parameters and the mean and variance of the simulated wind speed time series data for each case. Note that the mean and variance in the table corresponds to the simulated wind speed time series over 5 years. Note also that the model parameters presented in the table can be used to simulate wind speed time series according to the procedure discussed in Paper II from which the ACC, PACC, CCC and CDF can be

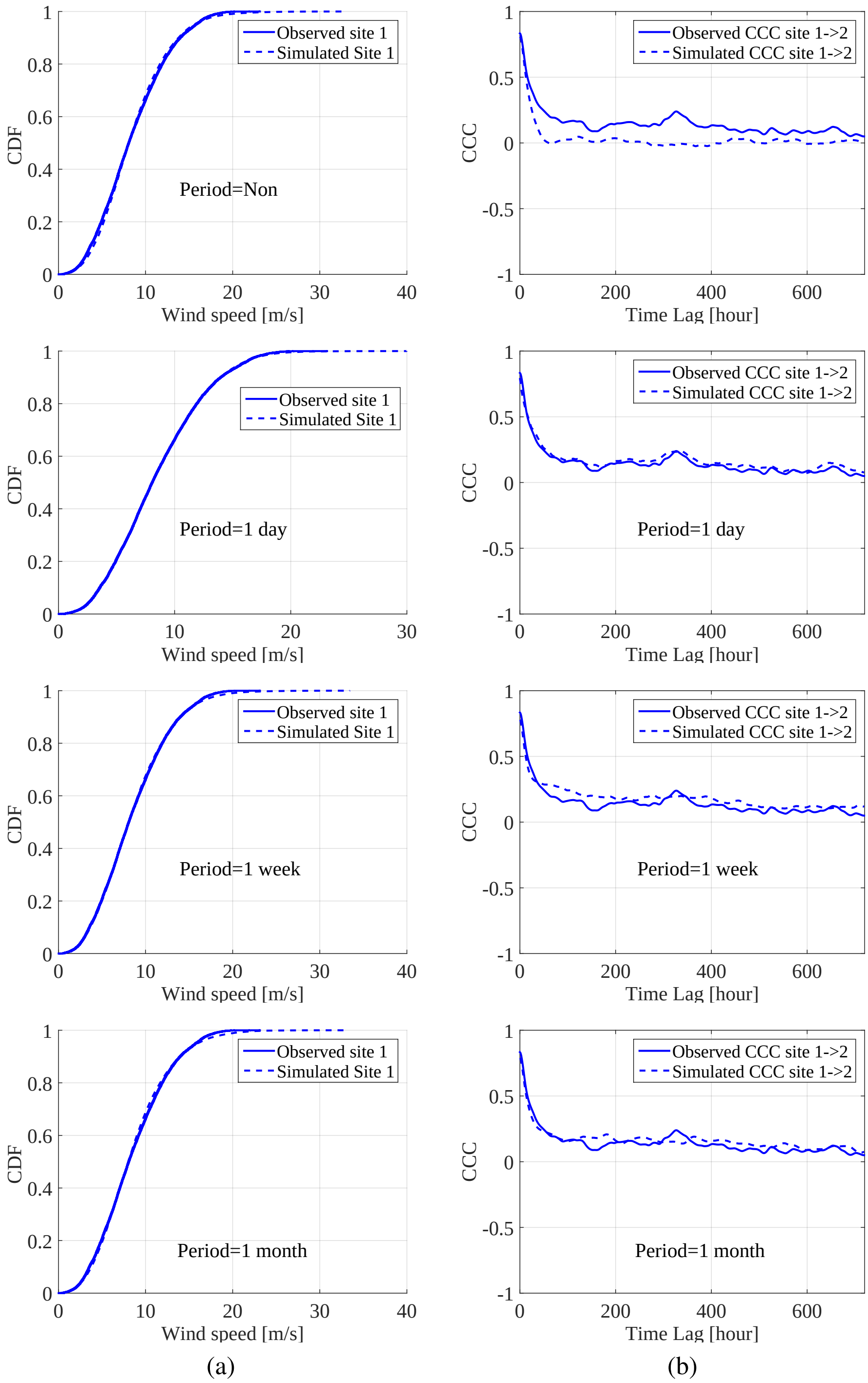

Figure 3.21: Effect of the choice of the periodic patterns on (a) CDF (Cumulative Distribution Function) and (b) CCC (Cross Correlation Coefficient)

calculated.

In Paper II, the application of the proposed modelling procedure is applied to model wind speed data from multiple sites. From the investigations made, it is concluded that VAR(6), Vector Auto Regressive model structure can be used to model spatially and temporally

Table 3.8: Wind speed sites, distance, mean and variance of observed wind speed at each sites associated with each case

Case	Site	Distance	$\mu_m(m/s)$	σ_m^2
Case 2	**S1-S3**	737km	$\begin{bmatrix} 8.49 \\ 8.49 \end{bmatrix}$	$\begin{bmatrix} 15.43 \\ 16.70 \end{bmatrix}$
Case 3	**S1-S7**	945km	$\begin{bmatrix} 8.49 \\ 9.48 \end{bmatrix}$	$\begin{bmatrix} 15.43 \\ 15.54 \end{bmatrix}$
Case 4	**S9-S11**	1126km	$\begin{bmatrix} 8.31 \\ 8.26 \end{bmatrix}$	$\begin{bmatrix} 13.29 \\ 13.00 \end{bmatrix}$

Table 3.9: Case 2: Model parameters of VAR(3) when monthly mean and variance are used in the transformation to remove the periodic patterns

Φ_1	Φ_2	Φ_3
$\begin{bmatrix} 1.9293 & 0.0289 \\ 0.0362 & 2.0231 \end{bmatrix}$	$\begin{bmatrix} -1.1846 & -0.0182 \\ -0.0158 & -1.3693 \end{bmatrix}$	$\begin{bmatrix} 0.2370 & -0.0064 \\ -0.0112 & 0.3261 \end{bmatrix}$
$\Theta_0 * 10^4$	μ_{sim}	σ_{sim}^2
$\begin{bmatrix} 0.1624 \\ 0.1024 \end{bmatrix}$	$\begin{bmatrix} 8.45 \\ 8.48 \end{bmatrix}$	$\begin{bmatrix} 15.76 \\ 16.89 \end{bmatrix}$

Table 3.10: Case 3: Model parameters of VAR(3) when monthly mean and variance are used in the transformation to remove the periodic patterns

Φ_1	Φ_2	Φ_3
$\begin{bmatrix} 1.9359 & -0.0125 \\ -0.0163 & 2.0305 \end{bmatrix}$	$\begin{bmatrix} -1.1888 & 0.0256 \\ 0.0286 & -1.3646 \end{bmatrix}$	$\begin{bmatrix} 0.2371 & -0.0132 \\ -0.0041 & 0.3163 \end{bmatrix}$
$\Theta_0 * 10^4$	μ_{sim}	σ_{sim}^2
$\begin{bmatrix} 0.1540 \\ -0.0856 \end{bmatrix}$	$\begin{bmatrix} 8.69 \\ 9.64 \end{bmatrix}$	$\begin{bmatrix} 15.99 \\ 17.36 \end{bmatrix}$

Table 3.11: Case 4: Model parameters of VAR(3) when monthly mean and variance are used in the transformation to remove the periodic patterns

Φ_1	Φ_2	Φ_3
$\begin{bmatrix} 2.0104 & -0.0106 \\ -0.0039 & 2.1171 \end{bmatrix}$	$\begin{bmatrix} -1.3277 & 0.0119 \\ 0.0196 & -1.5561 \end{bmatrix}$	$\begin{bmatrix} 0.30051 & -0.0007 \\ -0.0095 & 0.4232 \end{bmatrix}$
$\Theta_0 * 10^4$	μ_{sim}	σ_{sim}^2
$\begin{bmatrix} 0.4445 \\ 0.4530 \end{bmatrix}$	$\begin{bmatrix} 8.19 \\ 8.26 \end{bmatrix}$	$\begin{bmatrix} 13.75 \\ 13.66 \end{bmatrix}$

correlated hourly average wind speed time series in the North Sea and the Baltic Sea area.

3.5 Chapter summary

In this chapter, the summary the wind speed modelling from Paper I and Paper II is presented. The main result in Paper I is the introduction of frequency decomposition in the modified ARMA based modelling procedure. Based on the investigation made using the modified modelling procedure, it is proved that the procedure can be used to model 10 minute average wind speed data where temporal correlation, probability distribution and periodic characteristics of the time series wind speed data are captured in the model. The main result from Paper II is the proposed modified VARMA based modelling procedure. Based on the investigations made by using the procedure, it is quantified that VAR(6) (Vector Auto Regressive model of order 6) can be used as a model structure to model spatially and temporally correlated wind speed in the North Sea and the Baltic Sea area.

Chapter 4

Economic analysis of HVDC transmission expansion using pre-defined exchange

In this chapter, optimum sizing of VSC HVDC transmission system expansion using pre-defined time series exchange power, which could represent a market data of economic power exchange, is investigated. First, a generic optimization model, that can use the time series, is developed. By using the model, optimum sizing of VSC HVDC inter-connectors between electricity markets is investigated. In addition, the effect of integrating a WPP into an inter-connector, designed for power exchange, is analysed and the possibilities for system reinforcement is indicated.

4.1 Background on electricity markets

As discussed in Section 1.2, the future meshed HVDC grid is expected to be built in step by interconnecting two or more existing systems through transmission links. The resulting transmission grid increases the amount of power that can be traded securely and the number of generators and consumers that can take part in the electricity market.

However, expanding transmission networks through the construction of new lines or upgrading of existing facilities are costly and should be undertaken only if they can be justified economically. In order to deliver maximum economic welfare to the society, the generation cost saving resulting from the expansion needs to be balanced with the investment to ensure long term least cost development [68].

In this section, an optimization model, that can be used in building the grid stepwise, is presented. The model is developed based on a predefined exchange power data and can be used to quantify the economic value of the electricity trade over the transmission line. The possible relation between the pre-defined exchange power data and a market structure is indicated in this section.

4.1.1 Types of electricity markets

In a de-regulated electricity market, different utilities operate in a coordinated manner to minimize the pool or the over all cost of the utilities by transmitting power from areas with lower cost to the ones with higher cost. Power pools are classified into three based on the role of the pool operator and the way the power transactions are set-up. In this section, two types of power pools, which are relevant to the studies in this work, are presented. These are *Economic exchange of energy* and *Energy brokerage* market structure [69], [70].

Economic exchange of energy:- is a simple arrangement between utilities having significant difference in their marginal cost. The utility with higher marginal cost buys power from the utility with lower marginal cost. For this kind of arrangement to succeed, the savings from the system production cost resulting from the cooperation should be higher than the transmission line fee.

Energy brokerage:- is an arrangement where several utilities join to form a pool with a central broker coordinating the pool. In an energy brokerage system, the individual utilities carry out their own generation scheduling and formulate their purchase and sell decisions. The decisions are submitted to the broker in the form of bids, specifying the quantity available for purchase and /or sell with the corresponding prices. The energy broker determines the interchange schedule based on the bids, using certain criterion such as maximizing the social benefit.

Economic exchange of energy is a fully decentralized electricity market structure where decisions are made by individual utilities making the exchange. In this type of market structure, the trading parties agree on how much to sell/buy and submit their plan to the system operator. The role of the system operator, in this type of market structure, is not to monitor the economic efficiency of the market, but to maintain a safe operation of the power system. In contrast to the *economic exchange of energy*, *energy brokerage* market structure is operated in a centralized way. In this type of market model, the broker can observe all purchase and sell offers simultaneously to allocate the transactions and achieve better economy of operation.

One of the objectives of this chapter and Chapter 5 is to develop an optimization model that can be used to size system components in a stepwise building of a VSC HVDC transmission system. In this chapter, the optimization model is developed based on a pre-defined exchange power data. The pre-defined exchange power data is assumed to represent a kind of expected power exchange agreement between utilities to be connected by the transmission system. The expected exchange agreement, which in this case is defined as pre-defined exchange power, can be considered similar to the *Economic exchange of energy* market structure. In Chapter 5, the optimization model is developed based on *energy brokerage* market structure.

4.2 Optimization model based on pre-defined exchange

Consider that N number of utilities are connected through a transmission grid and assume that each utility has a pre-defined export schedule of $P_{t,i}^{Ex0}$. Apart from the export schedule, the benefit resulting from the power exchange is not known in this case. However, what can be known is that the benefit cannot be lower than a transmission tariff, the fee paid the transmission system operator/owner.

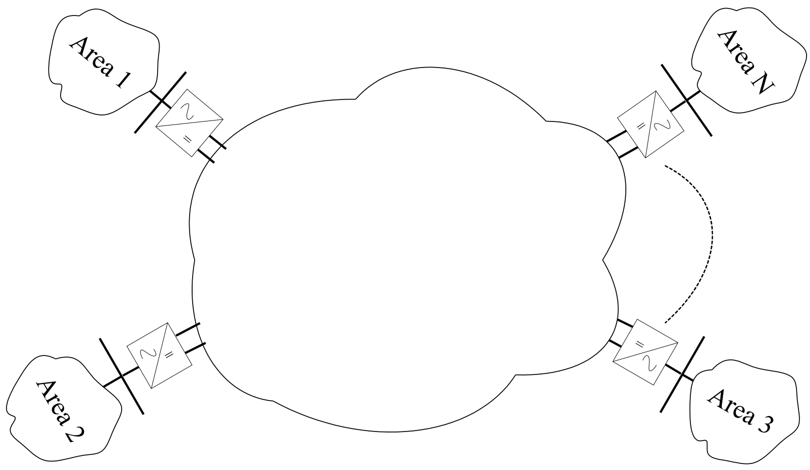

Figure 4.1: VSC HVDC transmission link connecting two electricity market area

From the perspective of the utilities connected to the network in Figure 4.1, their benefit is maximized if the pre-defined exchange, $P_{t,i}^{Ex0}$ goes through the network without limitation. However, from an investment point of view, it could be costly to build the system to avoid the limitation. As a result, the cost of limiting the pre-defined exchange power and the investment cost of the transmission system need to be balanced.

Assume that α is a unit transmission tariff and C^{bloss} a is minimum loss in benefit (which can be referred to as loss in benefit) due to limitation of the pre-defined exchange. The loss in benefit can then be formulated as

$$C^{bloss} = \alpha \sum_{t=1}^{T} \sum_{i=1}^{N} \left(P_{t,i}^{Ex0} - P_{t,i}^{Ex} \right) \tag{4.1}$$

where C^{bloss} is total loss in benefit during a time interval T where T is the length of the time series exchange data used; $P_{t,i}^{Ex}$ is the allowable export and N is the number of terminals in the system. From an operational point of view, the objective would be to minimize the C^{bloss} in (4.1) while system constraints are observed.

The loss in benefit in (4.1) is a starting point if upgrading the system via reinforcement or building a new transmission link in the grid is needed. If the magnitude of C^{bloss} is too high, it is highly likely that upgrading the system may minimize the loss in the benefit. Hence, an objective of an optimization model, that can be used in upgrading the system can be formulated as

$$C^{total} = PV \left[C^{bloss} + C^{ploss} \right] + C^{inv} \tag{4.2}$$

where C^{total} is the total cost, and the objective is to be minimized; PV is a constant used to calculate present value which is formulated as

$$PV = \frac{1}{r}\left[1 - \frac{1}{(1+r)^n}\right] \tag{4.3}$$

where r is a discount rate and n is a life time of the investment. Through out this study the values of r and n are assumed to be 5% and 30 years respectively; which are reasonable values according to the industry partners in the reference group of this project. C^{ploss} in (4.2) is an cost of power loss in the system which is formulated as

$$C^{ploss} = 0.5\gamma \sum_{t=1}^{T}\sum_{i=1}^{N}\sum_{j=1}^{N}\left(U_{t,i} - U_{t,j}\right)^2 y_{i,j} \tag{4.4}$$

where γ is a unit price of energy which is about 50€/MWh in average in major European markets [71]; $U_{t,i}$ is a terminal voltage and $y_{i,j}$ is a conductance of the cable connecting terminal i and j. C^{inv} in (4.2) is an investment cost which is formulated as

$$C^{inv} = C^{cbl} + C^{inst} + C^{vsc} \tag{4.5}$$

where C^{cbl} is cost of cable; C^{inst} is cost of installation and C^{vsc} is cost of VSC converter.

Note that the values $y_{i,j}$ in (4.4) and; C^{cbl}, C^{inst} and C^{vsc} in (4.5) depend on the specific cable used. In Paper III, the parameters are discretely described as a function of cable types from a manufacturer. In this model, the parameters are defined as a continuous function of cable thickness, as discussed in Section 2.3. Based on the discussion in Section (2.3), the parameters are defined as

$$C^{cbl} = 0.5\sum_{i=1}^{N}\sum_{j=1}^{N}\left(a_0^{cbl} + b_0^{cbl} A_{i,j}^{a_0^P}\right) L_{i,j} \tag{4.6}$$

$$C^{inst} = 0.5\sum_{i=1}^{N}\sum_{j=1}^{N}\left(a_0^{ins} + b_0^{ins} A_{i,j}^{a_0^P}\right) L_{i,j} \tag{4.7}$$

$$C^{vsc} = \sum_{i=1}^{N}\left(a_0^{vsc} + b_0^{vsc}\sum_{j=1}^{N}\left(2U^R c_0^P A_{i,j}^{a_0^P}\right)\right) \tag{4.8}$$

where $A_{i,j}$ is cross-sectional area of the cable connecting bus i and j with a length of $L_{i,j}$ km; U^R is rated bus voltage which is the same as the base voltage of the system. The constants a_0 and b_0 are presented in subsection 2.3.4.

Observe that the objective of minimizing the total cost in (4.2) is solved while the following constraints are satisfied

$$\begin{aligned}
&P_{t,i}^{Ex} = \sum_{i=1}^{N}\sum_{j=1}^{N} U_{t,i}\left(U_{t,i} - U_{t,j}\right) y_{i,j} \\
&U_i^{Min} \le U_{t,i} \le U_i^{Max} \\
&A_{i,j} \ge 0 \\
&A^{Min} \le A_{i,j} \le A^{Max} \\
&\left(U_{t,i} - U_{t,j}\right) y_{i,j} \le c_0^I A_{i,j}^{a_0^I} \\
&\left(U_{t,i} - U_{t,j}\right) y_{i,j} \ge -c_0^I A_{i,j}^{a_0^I}
\end{aligned} \tag{4.9}$$

where the relation in the first line represents power flow balance at a terminal where $\pm 5\%$ margin is considered in this study; the second line is bus voltage limits; the third and the fourth line specifies that the cross-sectional area is non-negative and is bound between a minimum and a maximum value; the fifth and the sixth line specify that the branch current at any time should be within the rated current value of the cable.

In the remaining part of the chapter, the optimization model defined through equation (4.2) to (4.9) is used in the investigation of the stepwise building of HVDC transmission systems.

4.2.1 Pre-defined time series exchange power

A pre-defined time series exchange power data is an important input data to the optimization model in (4.2). Figure 4.2 shows normalized values of pre-defined time series exchange power in the NordPool market during 2015 [72]. Figure 4.2(a) shows the time series data and Figure 4.2(b) shows annual duration curves of the data. Note from Figure 4.2(b) that the average of the absolute value of the normalized exchange data varies from market to market which affect the optimum sizing of cables.

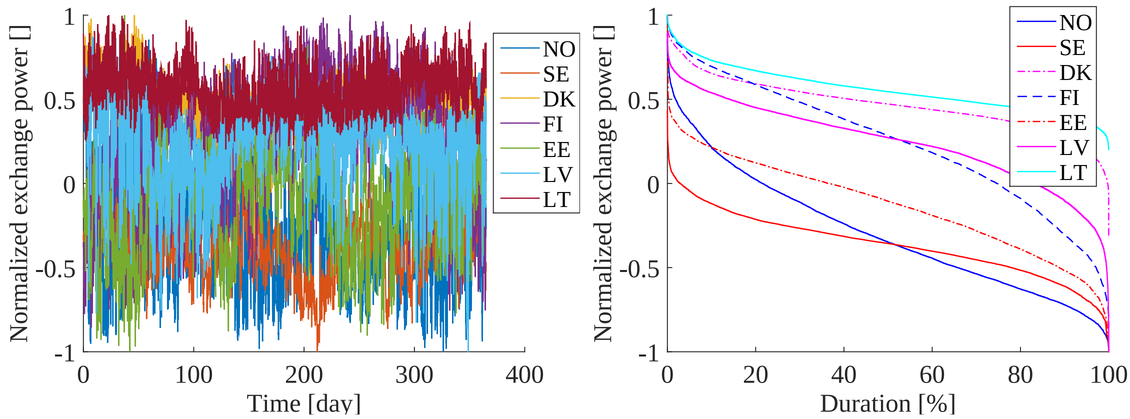

(a) (b)

Figure 4.2: Hourly average time series exchange power in different electricity markets in the NordPool during 2015 (a) time series data (b) annual duration curves, where NO, SE, DK, FI, EE, LV and LT stands for Norway, Sweden, Denmark, Finland, Estonia, Latvia and Lithuania respectively.

4.3 Optimum sizing of a two terminal system for power exchange

In this section, optimum sizing of building a new transmission line between two electricity markets is investigated. Figure 4.3 shows a transmission line connecting two markets. The optimum sizes of cables connecting the two areas in the figure is determined by using the optimization model in (4.2) that minimizes the total cost of the system.

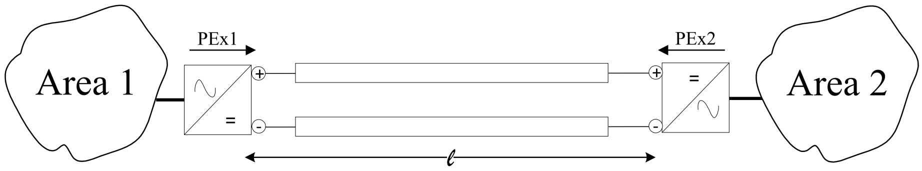

Figure 4.3: A two terminal VSC HVDC transmission system used for power exchange

In the initial part of the simulation, a unit transmission tariff (α) and unit energy cost (γ) of 20 €/MWh and 50 €/MWh, respectively, are assumed. And later the sensitivity of the results to the assumptions are analysed where the assumptions are based on Ref. [73], [71]. As mentioned before, an interest rate or discount rate of 5% and project life time of 30 years are used in calculating PV constant.

Figure 4.4 shows the optimum cable size as a function of maximum exchange capacity and cable length. The pre-defined time series exchange, used as input in the simulation,

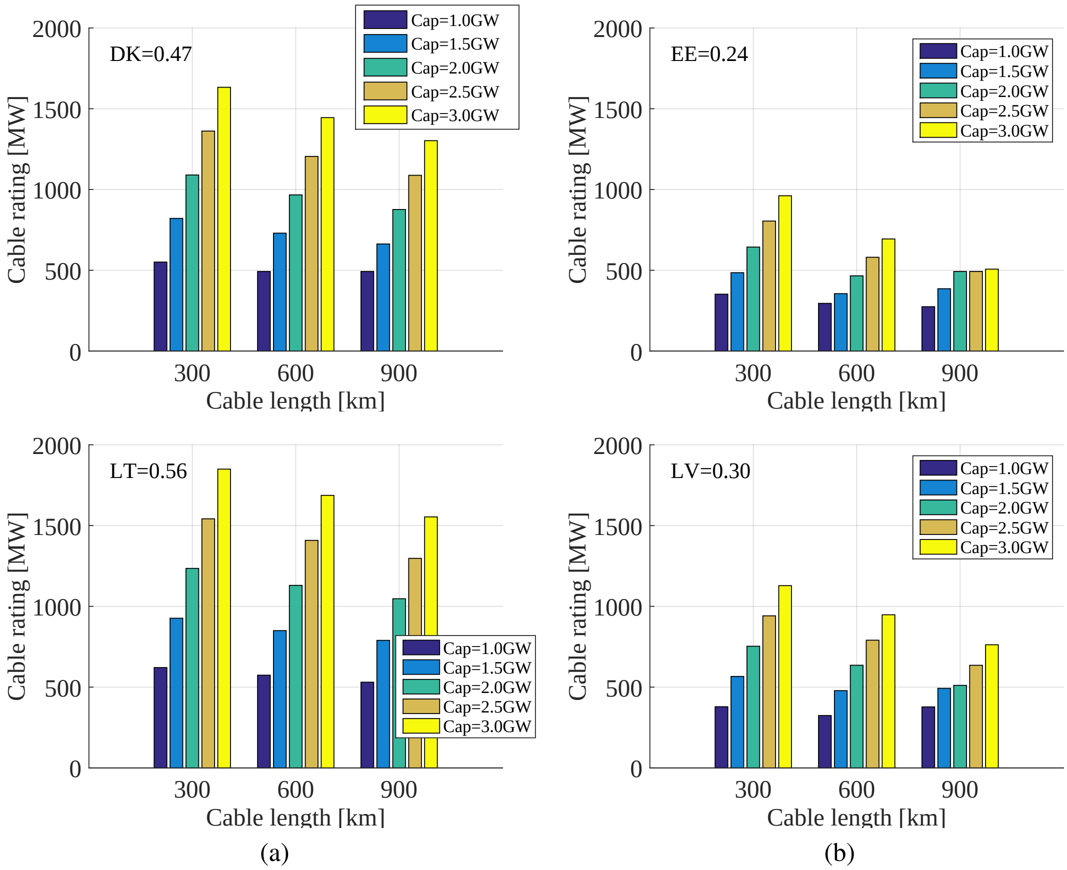

Figure 4.4: Optimum cable size as a function of maximum exchange capacity and cable length (a) for DK and LT exchange type (b) for EE and LV type where DK, LT, LV and EE stands for Denmark, Lithuania, Estonia and Latvia receptively

is calculated by multiplying the desired exchange type in Figure 4.2 with the maximum exchange. The results in Figure 4.4 also show the effect of using different exchange profile type on the choice of the optimum cable size. It is observed that the optimum cable size is dependent on the mean of the absolute value of the normalized exchange profile types presented in Figure 4.2. From the figure, it is calculated that the mean of the absolute value of the normalized data of NO, SE, DK, FI, EE, LV and LT are 0.40, 0.37, 0.47, 0.38, 0.24, 0.3 and 0.56 respectively. From these, the largest values are that of LT and DK (0.56 and 0.47). Similarly, the smallest ones are that of EE and LV (0.24 and 0.3). Figure 4.4(a) shows optimum cables sizes when the exchange type DK and LT and Figure 4.4(b) shows the optimum cable sizes for exchange types of EE and LV. Note that the higher the absolute mean value, the thicker the cable. Note also that when the absolute mean value is reduced by about 50%, the optimum cable size is reduced by about 35%.

It can also be observe from the results in Figure 4.4 that the optimum cable size vary with the cable length and maximum exchange capacity. The later is obvious since price elasticity is not included in the optimization model. It would be interesting to normalize the results in the figure to generate a more generic presentation of the results. Figure 4.5 shows the

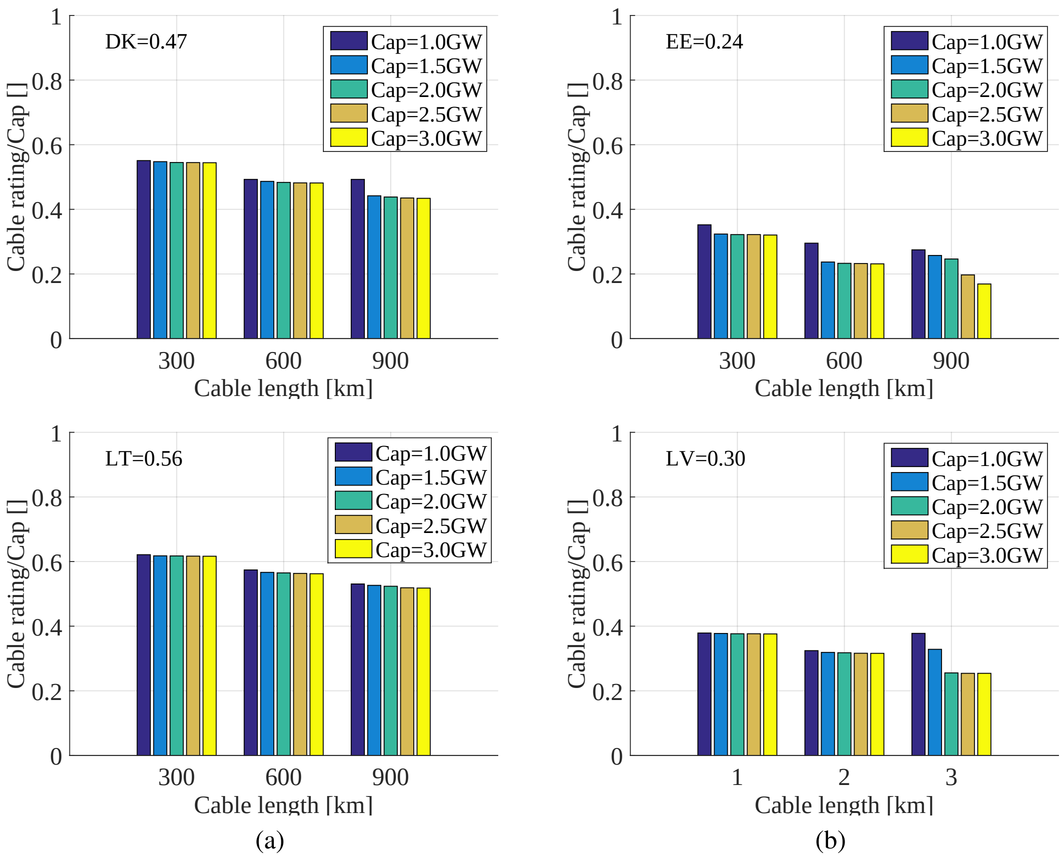

Figure 4.5: Ratio of optimum cable size and maximum exchange capacity as a function of maximum exchange capacity and cable length (a) for DK and LT exchange type (b) for EE and LV type

results when the optimum cable sizes in Figure 4.4 are divided by their respective maximum exchange capacity. Figure 4.5(a) shows the ratio of optimum cable sizes and exchange capacity for the DK and LT exchange types. Note that for a given length, the ratio is almost independent of the maximum exchange capacity. The results show that, for the given exchange type, the optimum cable size is less than 60% of the maximum exchange.

Note also that, the ratio is close to the absolute mean of the normalized exchange data, which conforms an initial thought that to dimension the cable according to the absolute mean of the exchange is a good idea.

Accordingly, the conclusion based on the results in Figure 4.5 is that it is possible to have a good estimate of an optimum cable size for a given exchange data without running the optimization model. In addition to determining the optimum cable size, it would also be interesting to estimate the investment cost of the optimum solution in a simple way.

4.3.1 LRMC and SRMC

Figure 4.6 presents the investment cost of the system as an investment made on every MWh during the life time of the project. The term is called, LRMC (Long Run Marginal

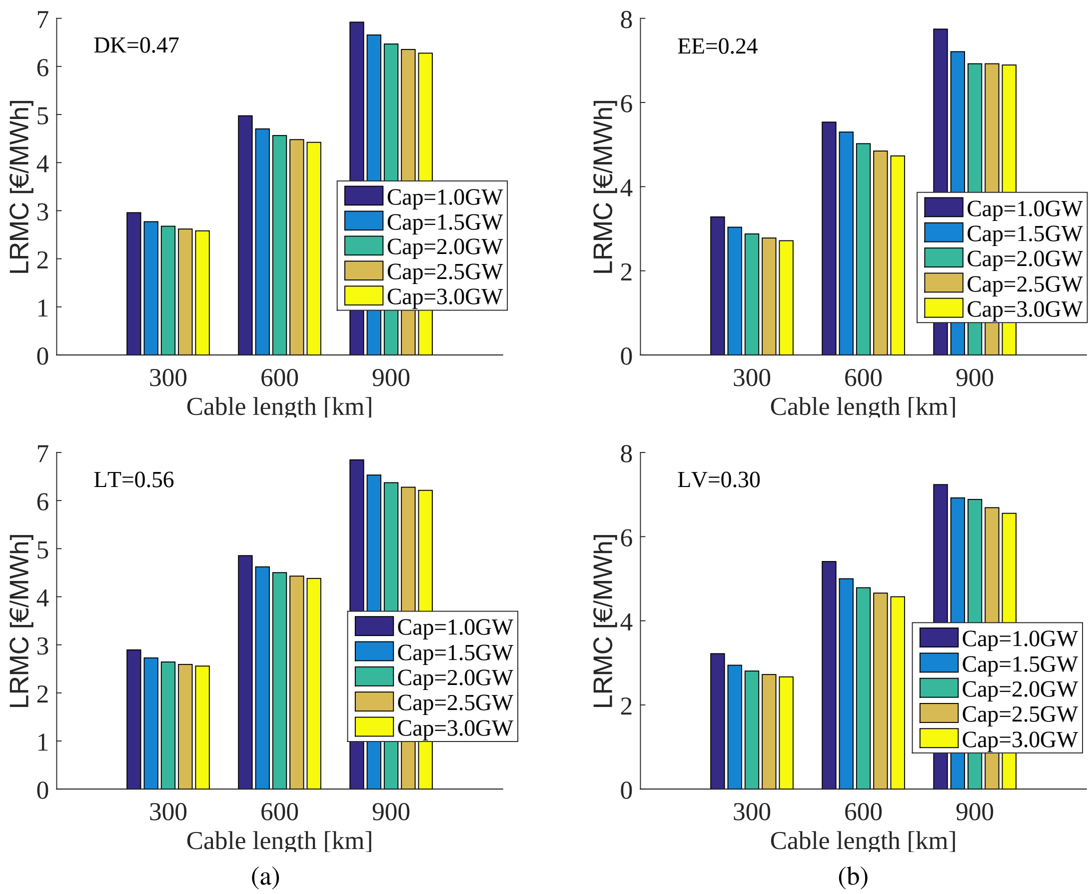

Figure 4.6: Ratio of optimum cable size and maximum exchange capacity as a function of maximum exchange capacity and cable length (a) for DK and LT exchange type (b) for EE and LV type

Cost). It is calculated by dividing the investment cost by the product of optimum cable size in MW, 30 years life time, 12 months in a year, 30 days in a month and 24 hours in a day (C^{inv}/([CableRating[MW]]x[Number of hours in 30 years])). The results in the figure show that, for a given cable length, the LRMC values do not vary with exchange capacity and types. The results in the figure also show that, for a cable length of 300 km, the LRMC value is about 3 €/MWh. For every 300 km increase in cable length, the LRMC increases by about 2 €/MWh. Based on the standardized LRMC values, one can easily calculate the investment cost of a transmission cable with a specific optimum cable size.

Observe that the results in Figure 4.6 are generic for a VSC HVDC transmission system. In addition, the results in the figure are extremely important to determine if an investment on a given optimum design is economically feasible or not. For the given design to be feasible for the investor, the SRMC (Short Run Marginal Cost) should be greater than the LRMC. The SRMC is closely related with the unit transmission tariff (α), defined in (4.1). Similar to the LRMC, the SRMC is calculated by dividing the PV of transmission tariff by the product of the optimum cable size and the number of hours in 30 years (SRMC=TTariff/([CableRating[MW]] x [Number of hours in 30 years]).

Note that, for a given value of unit transmission tariff (α), the PV of transmission tariff, $C^{ttariff}$, can be calculated as

$$C^{ttariff} = PV\left[0.5\alpha\sum_{t=1}^{T}\sum_{i=1}^{N}\sum_{j=1}^{N}|F_{t,i,j}|\right] \tag{4.10}$$

where PV is a present value calculation constant defined in (4.3) and $F_{t,i,j}$ is a power flow between terminal i and j at time t. From $C^{ttariff}$, the SRMC can be calculated. Figure 4.7 shows the SRMC of optimum system design for LT and EE exchange profile types. Figure 4.7(a) SRMC of the optimum system design when LT exchange profile type is used. The results in the figure show that the SRMC is close to 10€/MWh for all cable length. Note that the SRMC is greater than the LRMC all the time in this case. This means that it is profitable to invest on the designs. Note also that at 300 km cable length, the difference between the LRMC and the SRMC is the largest; which means that the investors profit should also follow a similar trend.

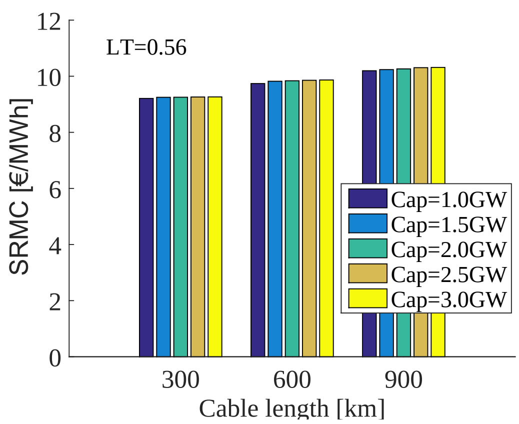

(a)

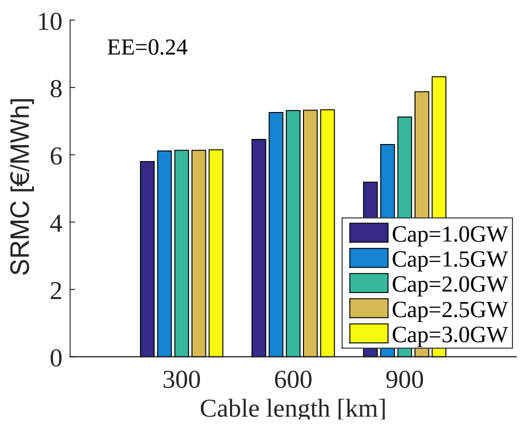

(b)

Figure 4.7: SRMC (Short Run Marginal Cost) as a function of maximum exchange capacity and cable length (a) for LT exchange type (b) for EE exchange type

Figure 4.7(b) shows the SRMC of the optimum system designs when EE exchange profile type is used. Similar to the results in Figure 4.7(a), it is economically feasible to invest in 300 km and 600 km system designs, although the difference between the LRMC and the SRMC is smaller in this case, which lowers the profit margin. In contrast to the results in Figure 4.7(a), for 900 km cable length, the SRMC is less than the LRMC for the lower level of maximum export. This verifies the fact that if th SRMC is less than the LRMC in any system design, then it is no longer economical to invest on the system.

4.3.2 LRMC, SRMC and Investor's profit

Figure 4.8 shows the investor's profits of different optimum system designs. Note that the profits are presented as percentages. The percentage profits are calculated as

$$Investor\_\Pr ofit = \frac{\left(C^{ttariff} - C^{inv}\right)}{C^{inv}} * 100 \tag{4.11}$$

where $Investor\_\Pr ofit$ is the PV of the investor's profit in percentage of a given design; $C^{ttariff}$ is the PV of the transmission tariff defined in (4.10) and C^{inv} is the investment cost of the design which is formulated in (4.5). Figure 4.8(a) shows the PV of the investor's profit in percentage for exchange profile type of LT. The results show that the investor's profit during the life time of the system varies from 50$\%$ to 250$\%$ depending on the length of the transmission cable. Observe that the profit is the highest at the shortest cable length; which is consistent with the observation made in Figure 4.7(a).

Figure 4.8(b) shows the investor's profit for the exchange type of EE. For the same length, the profit in this figure is lower than half of the profit in Figure 4.8(a). Note also that for a cable length of 900 km and export capacity of 1 GW and 1.5 GW, the designs are not economically feasible. For the same cable length and exchange capacity greater than 2 GW, the profit is closer to zero. Based on the results in Figure 4.8(b), it not profitable to invest on systems having a cable length higher than 600 km.

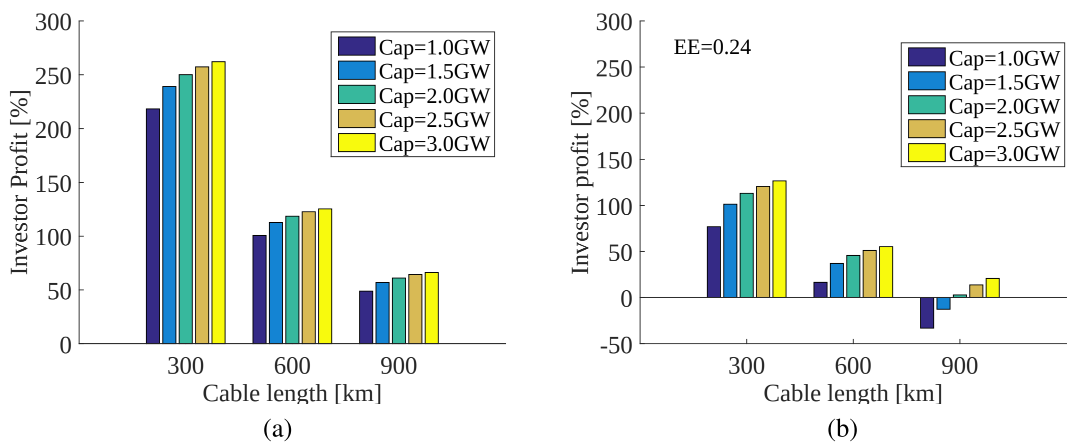

Figure 4.8: Percentage investor profit as a function of maximum exchange capacity and cable length (a) for LT exchange type (b) for EE exchange type

Figure 4.9 shows the payback period of the investment. For the exchange type of LT in Figure 4.9(a), the pay back time of all the projects lie in the range of 5 to 15 years depending on the lengths of the cables. Note from the results in Figure 4.9(b) that when the payback period is greater than 30 years, it means that the investment cannot be recovered during the life time of the project with the assumed interest rate, which is 5% in this case. All the results in this figure are also consistent with the results in the preceding figures.

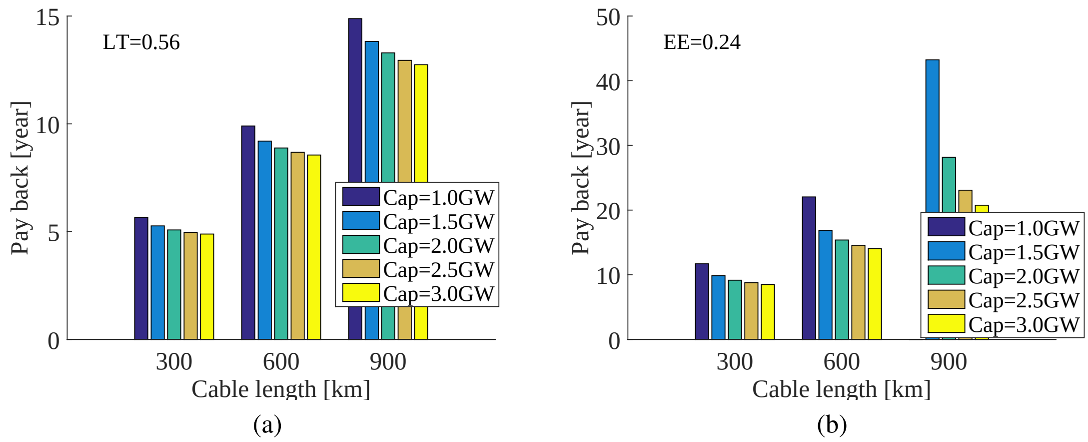

Figure 4.9: Pay back period as a function of maximum exchange capacity and cable length (a) for LT exchange type (b) for EE exchange type; for a 30 year life time and a 5% interest rate

4.3.3 Sensitivity of the results on unit transmission tariff, α

The results in Figure 4.10 shows the sensitivity of the LRMC on the change in unit transmission tariff. Figure 4.10(a) and Figure 4.10(b) show LRMC when the values α are 15€/MWh

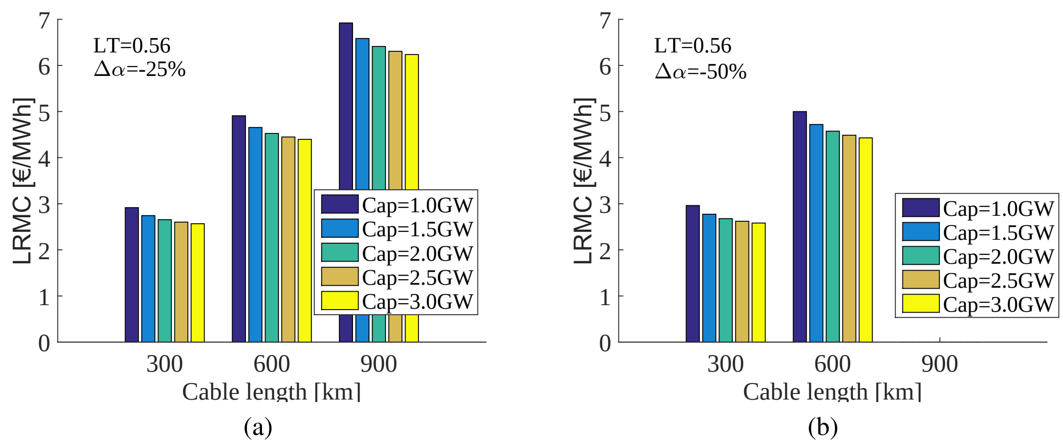

Figure 4.10: Ratio of optimum cable size and maximum exchange capacity as a function of maximum exchange capacity and cable length for exchange profile type of LT when α is equal to (a) 15 €/MWh and (b) 10 €/MWh

and 10€/MWh respectively which is 25% and 50% reduction in α. The results in the figures show that LRMC is not affected by the change in α from the 20 €/MWh initially used.

Figure 4.11 shows the effect of a change in unit transmission tariff on the investment profit. Figure 4.11(a) and Figure 4.11(b) shows the effect of a 25% and 50% reduction in α value. Based on the results in the figure, it can be quantified that every 1% reduction in α leads to about a 3% loss in the investor's profit.

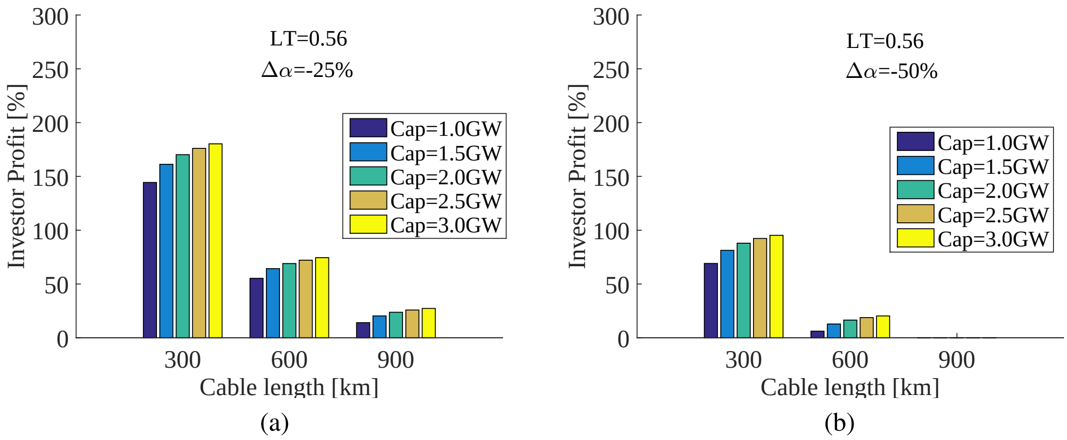

Figure 4.11: Percentage investor profit as a function of maximum exchange capacity and cable length for LT exchange when α is equal to (a) 15 €/MWh and (b) 10 €/MWh

4.4 Expanding a two terminal into a three terminal system

So far, different aspects of the optimum dimension of building a new transmission system is discussed. Figure 4.12 shows a network diagram of a three terminal VSC HVDC transmission system with a WPP. In this section, an investigation of integrating a WPP into a

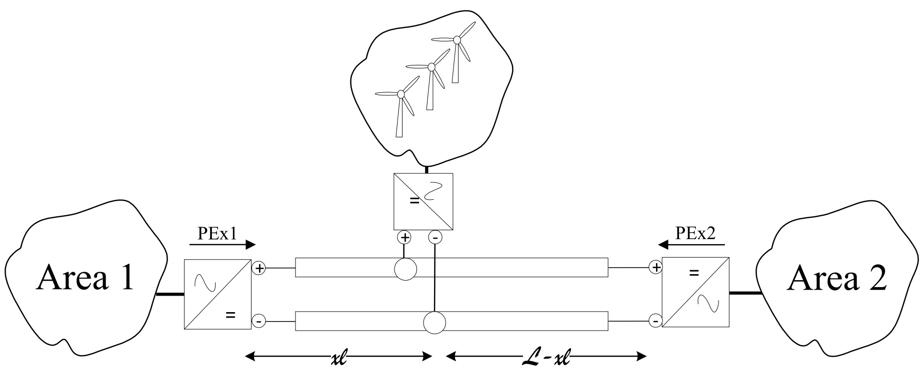

Figure 4.12: A three terminal HVDC transmission system formed by integrating a WPP to a transmission link designed for power exchange

two terminal system presented. It is assumed that the expansion is made by integrating a WPP into a system originally designed for power exchange.

In the analysis of the system in Figure 4.12, two specific scenarios are considered. In both scenarios, the maximum pre-defined exchange power in the original system (without the WPP) is assumed to be 3000 MW. In addition, the length of the cable connecting terminal 1 and 2 is assumed to be 600 km, in both scenarios. A transmission tariff of 20 €/MWh is also assumed for both scenarios. Furthermore, a WPP with a capacity factor of 50% and turbine heights of 100 m is considered in the simulation.

In the first scenario, the exchange profile type is assumed to be that of LT, shown in Figure 4.2. Observe that for this kind of exchange power profile, one terminal is exporting or importing power all the time, as can be seen from the duration curves in the figure. For the assumed maximum exchange and cable length and by using the objective function in (4.2), the optimum cable size of the original system is determined to 1670MW and the corresponding PV of cost of power loss for the optimum design is determined to be 102 M€.

In the second scenario, the exchange profile type is assumed to be that of NO in Figure 4.2. Note that for this profile type, the exchange power flows in both directions at different times. For the assumed maximum exchange power and cable length and by using the objective function in (4.2), the optimum cable size and the present value of cost of power loss in this scenario is 1232 MW and 64 M€ respectively.

4.4.1 Effect of WPP integration on cost of power loss

Figure 4.13 shows the effect of WPP integration on the change in the PV of the cost of power loss. Note that the change is calculated by subtracting the cost of power loss in the original system from the system power loss with different WPP capacities. Hence, a

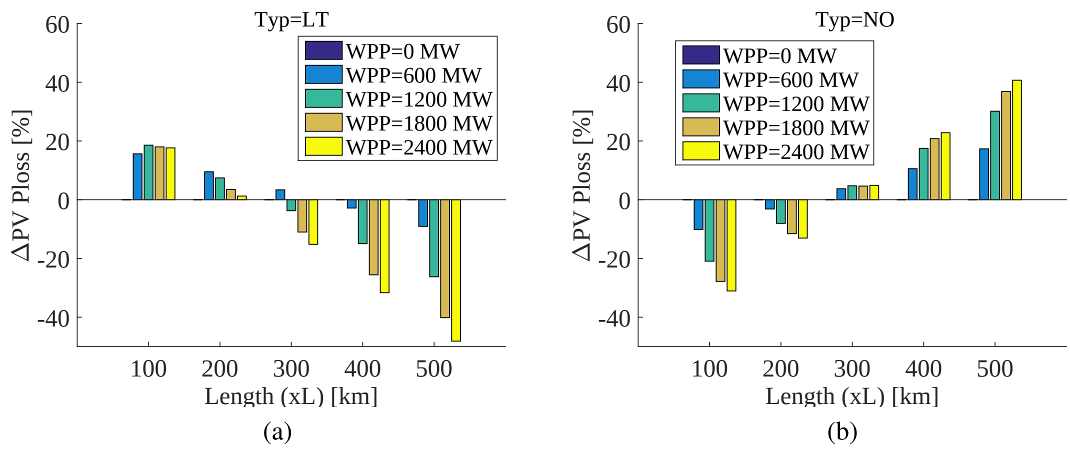

Figure 4.13: Effect of WPP integration on the change in the PV cost of power as a function of WPP capacity and length of the WPP from Area 1 for exchange profile type of (a) LT (b) NO

positive value means an increase in cost of power loss and vice versa. Figure 4.13(a) shows the results when the exchange profile type of LT is used in the simulation. Observe from the results in the figure that when the WPP is closer to Area 1, the cost of loss is the highest. As the distance the WPP gets farther from Area 1 and closer to Area 2, the cost of power loss decreases since Area 2 is importing power all the time.

Figure 4.13(b) shows the percentage change in PV of the cost of power loss for the NO exchange type. The results in the figure show that the cost of power loss is the lowest when the WPP is closest to Area 1. This is because, Area 1 is importing power most of the time, according to the profile type used. From this, it can concluded that the change in cost of power loss resulting from the integration WPP into an existing system depends on the distance of the WPP from the area importing power most of the time. The closer the WPP is to the importing area, the higher the reduction in the cost of power loss.

4.4.2 WPP integration and benefit of system reinforcement

Note that, the results in Figure 4.13 are determined without considering system reinforcement. However, reinforcing parts of the integrated system could result in added advantages for the system. One of the advantages could be reduced total system cost which consists of investment cost, cost of curtailment and cost of power loss in the system.

Figure 4.14 shows the required level of system reinforcement as a function of WPP capacity and length of the WPP from Area 1. The results in the figure indicate that reinforcing the cable between the WPP and Area 1 can result in a reduction in the total system cost. It is observed from simulations that there is no need to reinforce the branch cable between Area 2 and the WPP.

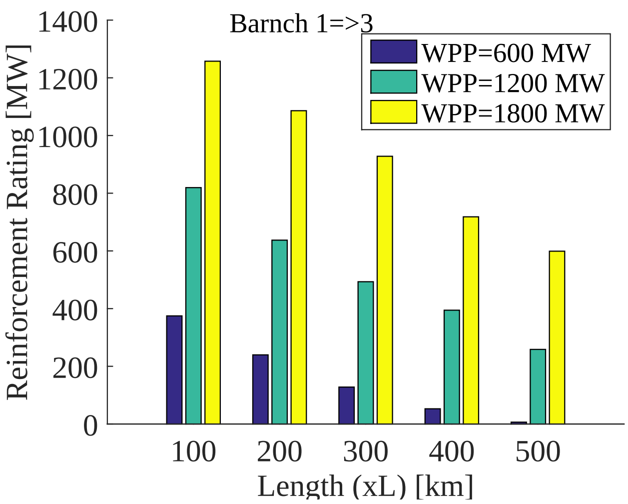

Figure 4.14: Need for system reinforcement as a function distance of the WPP from Area 1 and WPP capacity, branch 1 => 3

4.5 Summary and conclusion

In this chapter, optimum sizing of a VSC HVDC transmission system connecting two markets with a pre-defined time series exchange power is investigated. From the investigated cases, it is verified that the optimum size of inter-connector can be closely approximated to the absolute mean of the exchange power through it.

Based on the investigated cases, it is found that the LRMC of a VSC HVDC transmission system is case independent. For a 300 km cable length, the LRMC is determined to be 3 €/MWh and increases by 2 €/MWh for every 300 km increase in cable length.

In addition, it is verified that for an investment in a given optimum design to be profitable, the SRMC should be higher than the LRMC for a given cable length. When a unit transmission fee of α=20€/MWh is used for a system with a normalized absolute mean of 0.56, the SRMC is determined to be 10€/MWh, irrespective of the length of the transmission cable. For the given stated absolute mean value, it is shown that it always profitable to invest on the designs with cable lengths from 300 km to 900 km; and maximum exchange ranging from 1 GW to 3 GW. From an investment point of view, the same designs can yield a profit ranging from 50% to 250% of the investment cost depending on the length of the cable in the specified range. It is also shown that the higher the SRMC, the higher the profit to the investor. Based on the studied cases, it is quantified that every 1% decrease in the unit transmission tariff, α, leads to 3% loss in the investor's profit.

Moreover, based on the investigation made on a system with a normalized mean absolute value of 0.25 or less, it is concluded that it is not profitable to invest in the optimum designs with cable lengths greater than 600 km.

Furthermore, from the investigation made on the integration of a WPP into a system, initially designed for exchange; it is conclude that the closer the WPP is to the area that often imports power, the more the reduction in system power loss, which is as expected. It is also shown that placing the WPP closer to the area that often export power results in increased power loss in the system.

Chapter 5

Economic analysis of HVDC transmission expansion using a market structure

In this chapter, economic analysis of a step wise building of HVDC transmission system is conducted by using the energy brokerage market structure. First, a generic optimization tool is developed based on the market structure. The tool is then used to design and analyse different cases of VSC HVDC transmission expansions. Furthermore, an economic analysis of integrating WPP into a transmission system, initially built for electricity trade, is also investigated. And finally, the effect of integrating two sub systems, originally built to transport power from WPPs to the main grids, is investigated.

5.1 Energy brokerage market model

As discussed in Chapter 4, Section 4.1, an energy brokerage system is a type of market structure in a deregulated electricity market. As described in Section 4.1, the market structure is operated by a central broker on a regular basis. In this market structure, individual utilities carry out their own generation scheduling and formulate their purchase and sell decisions. The decisions are submitted to the broker in the form of bids, specifying the quantity available for purchase and /or sell with the corresponding prices. The energy broker determines the interchange schedule based on the bids, using certain criterion such as maximizing the social benefit. The savings achieved from the transaction are then divided among the participating utilities.

5.1.1 Bidding in an energy brokerage market structure

Figure 5.1 shows examples of bidding curves in an energy brokerage system. In Figure 5.1(a), the buying bid curve is arranged in a decreasing order of price and the selling bid curve is arranged in an increasing order of price. Note from the figure that the buy bid price varies with quantity, which is often referred to as elastic demand. If there is no transmission constraints between the buying and the selling area, the market is cleared at $(BQ2, BP2)$ where $BQ2$ and $BP2$ are the quantity and the corresponding price at the market clearing.

However, if there is a transmission constraint between the buying and the selling markets, the markets are cleared with different prices $(BQ1, BP1)$ and $(BQ1, BP3)$, as can be seen from Figure 5.1(a). Today, in principle, loads are inelastic to change in prices, but this is expected to change in the future. Figure 5.1(b) shows the bidding curves of the buyer and the seller. Note that the buyer's bid is vertical, which means that the buyer is willing to pay any price for the required quantity.

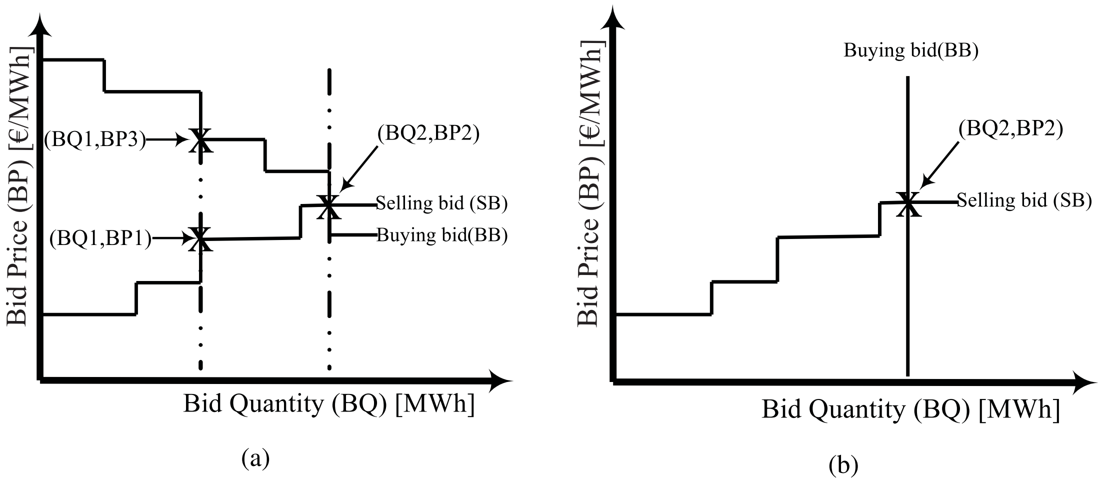

Figure 5.1: Buying and selling bid curves for (a) elastic load (b) inelastic load

5.1.2 Objective of energy brokerage market structure

In this market model, the main objective of the broker is, to determine the market clearing price that maximize Social Welfare (SW). Based on Figure 5.1(a), the SW is calculated by subtracting the area under the selling bid curve from the area under the buying bid curve which is formulated as

$$SW = \sum_{i=1}^{N} \sum_{j=1}^{N} (BB_j - SB_i)\, F_{i,j} \tag{5.1}$$

where BB_j is a unit buy price at market j, SB_i is a unit sell price at market i and $F_{i,j}$ is power exchange from market i to market j during certain time interval [69], [70].

Note that (5.1) is developed for an elastic load in Figure 5.1(a). However, for the inelastic load in Figure 5.1(b), the buy bid (BB_j) does not affect the objective in (5.1) and hence can be removed. The objective to be maximized, for inelastic load, is reformulated as

$$J_1 = -\sum_{k=1}^{N} SB_k \left[\sum_{m=1}^{N} F_{k,m} \right] \tag{5.2}$$

Note that the term in the bracket is a net power injected at terminal k, $P_k - D_k$. Hence, (5.2) can be reformulated as

$$J_1 = -\sum_{k=1}^{N} SB_k \left(P_k - D_k\right) \tag{5.3}$$

Since demand (D_k) is inelastic, it does not affect the objective and can be ignored from (5.3) and the equation can be reformulated as

$$J_2 = -\left[\sum_{k=1}^{N} SB_k P_k\right] \tag{5.4}$$

At this point, a new term, SC (Social Cost), is introduced. This term is defined to be opposite to J_2. From (5.4), SC can be defined as

$$SC = -J_2 = \left[\sum_{k=1}^{N} SB_k P_k\right] \tag{5.5}$$

Note that maximizing the SW in (5.4) is proportional to minimizing the SC in (5.5). Note also that, the term in bracket in (5.5) is the total generation cost in the market at a given time which is formulated as

$$gCost = \sum_{k=1}^{N} SB_k P_k \tag{5.6}$$

This means that, in the short term operation of the system, SC is equivalent to the total generation cost in the system. Hence, the objective of minimizing the SC can be achieved by minimizing the total generation cost provided that the desired set of constraints are satisfied.

5.2 Application of the market model for transmission expansion

The objective of minimizing the SC in (5.5) can be used to operate the system optimally and on an hourly bases. The model in (5.5) can be applied for long term transmission expansion planning provided appropriate changes are made to the equation.

Expanding transmission systems, through the construction of new lines or an upgrade of the existing facilities, increases the amount of power that can be traded securely and the number of generators and consumers that can take part in the electricity market. On the other hand, investments in new transmission equipments are costly and should be undertaken only if they can be justified economically. In order to deliver maximum economic welfare to the society, the generation cost saving resulting from the expansion needs to be balanced with the investment to ensure long term least cost development. In this case, this means that to undertake transmission expansion, the objective of minimizing the SC in the long term has to be achieved.

In order to apply (5.5) for long term transmission expansion planning, the cost of generation in (5.6) over longer time, need to be considered which can be formulated as

$$C^{gen} = \sum_{t=1}^{T} \sum_{k=1}^{N} C_k^{Sell} P_{t,k} \tag{5.7}$$

where T is the total number of, say hours, in a year. The sell bid (SB_k^{Sell}), often referred to as the Marginal Cost of production (MC), is expressed as ($SB_k^{Sell} = a_k + b_k P_k$). From now on, the MC is considered to be equivalent to SB_k^{Sell} and is defined as the cost of producing an extra MW of power in an hour. By using the MC, C^{gen} in (5.7) is reformulated to

$$C^{gen} = \sum_{t=1}^{T} \sum_{k=1}^{N} \left(a_k P_{t,k} + 0.5 b_k P_{t,k}^2\right) \tag{5.8}$$

In addition to the cost of generation, the SC in the long term also consists of cost of power loss and investment cost. Hence, the SC in the long term, that can be used for transmission expansion planing, can be formulated as

$$SC = PV \left[C^{gen} + C^{ploss}\right] + C^{inv} \tag{5.9}$$

where C^{gen} and C^{ploss} are annual costs of generation and power loss respectively and C^{inv} is an investment cost which consists of cost of cables, cost of installation and cost of VSC as formulated in (4.5) and PV is a constant used to calculate Present Value of C^{gen} and C^{ploss} during the life time of the project where the formulation is given in (4.3). The same assumption that was made in Chapter 4, an interest rate of 5$\%$ and a life time of 30 years, is also used in the investigated cases in this chapter, unless specified.

Note that C^{ploss} in (5.9) is the cost of power loss, defined in (4.4). Note also that, in addition to the bus voltage and line current constraints defined in (4.9), the objective in (5.9) is also constrained by bus power balance which is formulated as

$$P_{t,k} - D_{t,k} = \sum_{i=1}^{N} y_{ki} U_{t,k} \left(U_{t,k} - U_{t,j}\right) \tag{5.10}$$

where $P_{t,k}$ power generation and $D_{t,k}$ is demand at time t and bus k; y_{ki} is cable conductance and $U_{t,k}$ is a bus voltage at time t. Note that, from now on, when SW and SC are used, they refer to the long term value, unless specified.

5.3 Case set up and simulation input data

5.3.1 Time series demand

Time series demand is an important input data to the optimization model in (5.9). Recall that, in the optimization model, demand is considered to be inelastic; i.e. it does not change due to price. Figure 5.2 shows time series plots and duration curves of hourly average annual load demand profiles during 2015 in different electricity market areas in the

NordPool [72]. Figure 5.2(a) shows normalized time series plots of the loads. Figure 5.2(b) shows the annual duration curves of the loads. The curves show that the load profiles are fairly similar with slight differences. Note also that the zero demand presented in the figure could be due either an error in the measurement or an interruption of the load for a short duration.

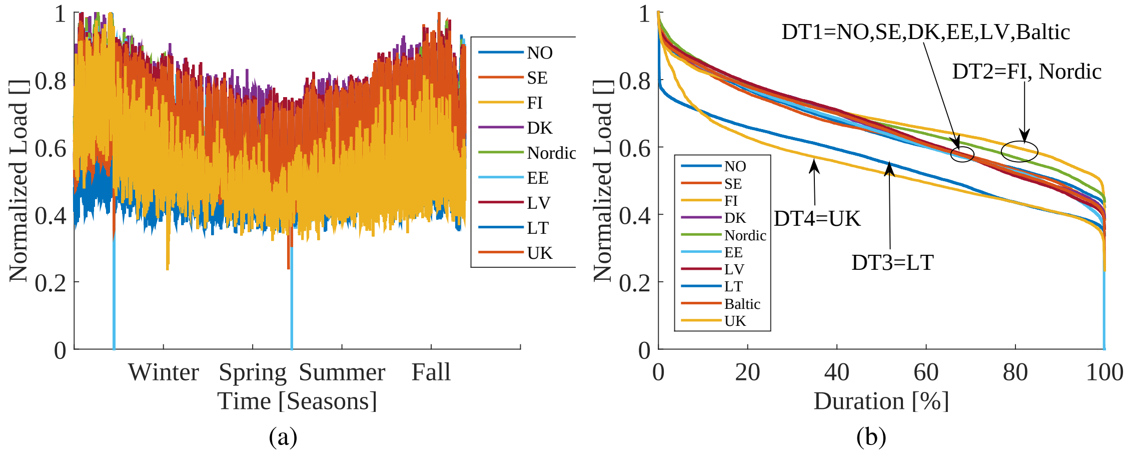

Figure 5.2: Normalized values of electric power demand profiles of different different electric power markets (a) time series demand profiles (b) load duration curves, where NO, SE, DK, FI, EE, LV, LT and UK stands for Norway, Sweden, Denmark, Finland, Estonia, Latvia, Lithuania and United Kingdom respectively.

The optimum sizing of an inter-connector can be affected by the distribution of the time series demand around the average value. Table 5.1 shows the variance, the average, the minimum and maximum values of the time series demand profile types presented in Figure 5.2. Note that the LT demand type has the largest variance whereas EE demand type has the smallest variance.

Table 5.1: Characteristics of time series demand in the NordPool markets during 2015

	NO	SE	FI	DK	Nordic	EE	LV	LT	Baltic	UK
Var	0.016	0.016	0.010	0.018	0.014	0.019	0.019	0.012	0.018	0.014
Avg	0.651	0.649	0.688	0.656	0.679	0.649	0.659	0.554	0.655	0.540
Max	1	1	1	1	1	1	1	1	1	1

5.3.2 Electricity price and Marginal Cost (MC)

Marginal cost (MC) data is another crucial input to the optimization model. In a perfectly competitive electricity market, the price of energy in the market reflects the true marginal cost of production. Figure 5.3 shows the prices of electricity in different markets during 2015 in the NordPool [72]. Assuming that each market is perfectly competitive, the marginal cost of generation in each market can be equated to the system prices. Note from

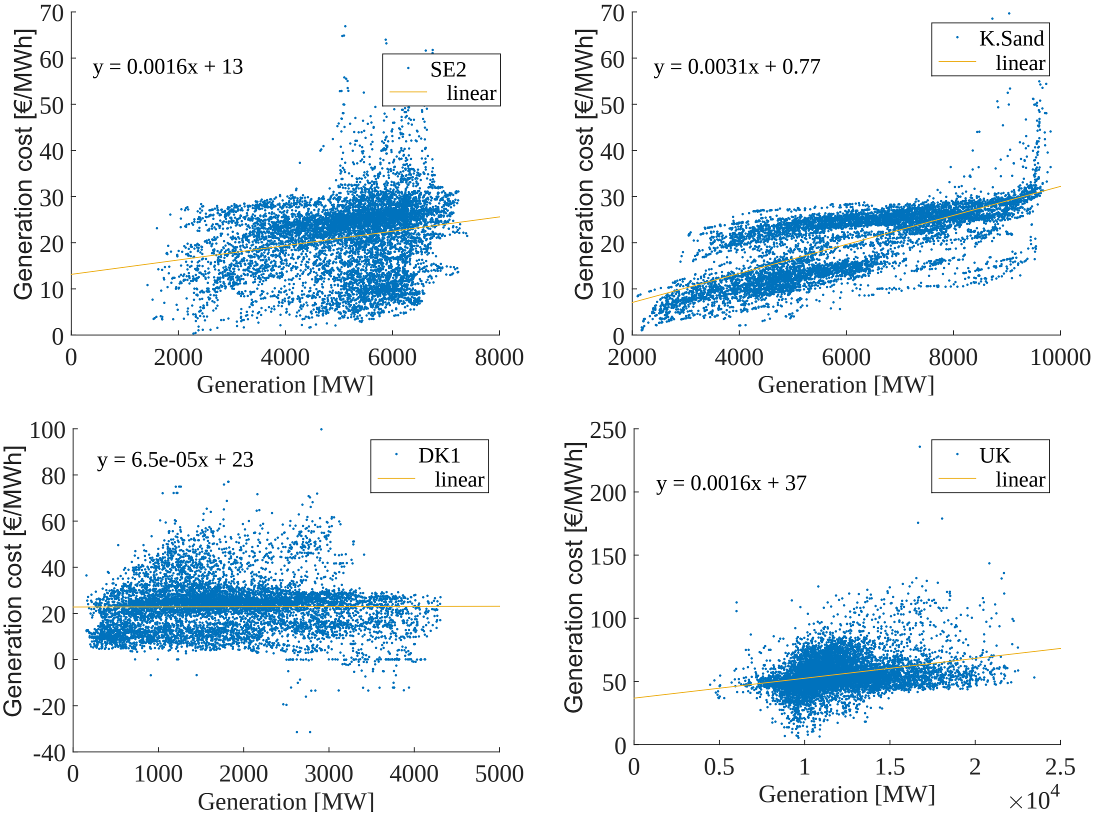

(a) (b)

Figure 5.3: Market prices and the corresponding estimated marginal generation cost function for different electricity markets during 2015, where SE2, DK1, Kr.Sand and UK stands for electricity market areas in Sweden, Denmark, Norway and United Kingdom respectively.

Figure 5.3 that the system costs, and hence the marginal generation costs, in each market is estimated by using a linear fit. Figure 5.3(a) shows the marginal costs in SE2 of Sweden and DK1 of Denmark where SE2 and DK1 are electricity market areas in Sweden and Denmark respectively. Similarly, Figure 5.3(b) shows the marginal generation costs in K.Sand and UK where K.Sand(Kristiansand) and UK stands for electricity market areas in Norway and the UK. Note that the coefficients of the marginal costs ($MC = a + bP$) varies depending on minimum and maximum demands and the dominant generation types in a specific system. For example, the coefficient a in K.Sand market is small compared with the others which means that the cost of generation in the area, at low demand is very low, due to the large amount of hydro generation in the area.

5.3.3 Optimum sizing of inter-connectors using real data

For an inter-connection of two electricity markets to make an economic sense, the marginal cost of generation in one market has to differ sufficiently toward that of the other. In this case, based on the price difference between the markets and the amount of expected power exchange, the optimum size of the inter-connector between the markets can be determined.

Figure 5.4 shows the plots of the MCs of three fictitious markets in Figure 5.3 over power generation ranging from 1 GW to 30 GW. Note from the results in the figure that power at the SE2 market varies in the range of 2GW and 8 GW; while the power in the Kr.Sand market is in the range of 2 GW to 10 GW. Similarly, the power in the UK market varies in the range of 5 GW to 24 GW.

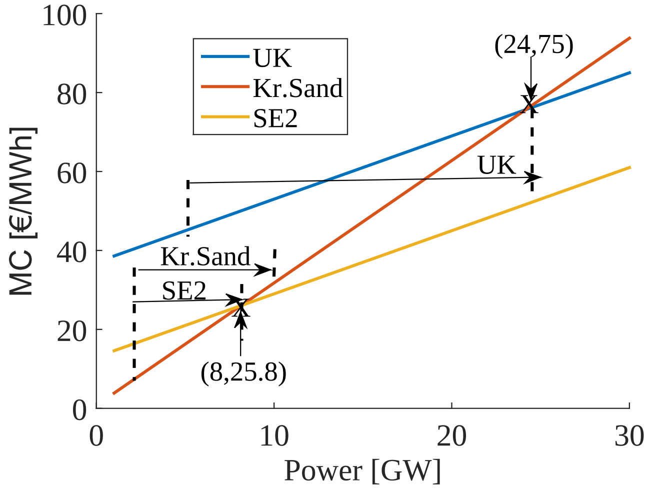

Figure 5.4: Plots of MCs of three fictitious electricity markets over a wide range of power

Accordingly, the used investigated cases in this chapter are inspired from the MCs of the SE2, Kr,Sand and UK markets, but not identical. Consider the interconnection of the Kr.Sand market and the UK market. From Figure 5.4, it can be seen that the MCs of the two markets cross at 24 GW. When power is greater than 24 GW, the MC in UK is lower than that in Kr.Sand. However, since the maximum power in Kr.Sand market is 10 GW, which is way below 24 GW, there is a zero chance for the UK market to export power to the Kr.Sand market. On the other hand, when the power is less than 24 GW, the MC in Kr.Sand is lower than that in UK. In this case, the Kr.Sand market can export power to the UK market.

Assuming a VSC HVDC transmission cable length of 600 km as an inter-connector between the two market, the optimum size of the inter-connector between the market, that minimize the SC in (5.9), is found to be 5.9 GW. Figure 5.5 shows export power through the inter-connector and the marginal costs in the two countries. Similar result is expected if the SE2 and UK markets are connected where exchange power always flows from the SE2 to the UK market. Accordingly, cases with difference in MC, for the whole operating region, is thus straight forward to calculate and in the synthetic cases considered in the following section in this chapter; the focus is put on the uncertain cases where the MCs of the markets are close to one another.

Observe from the plots in Figure 5.4 that, connecting SE2 and Kr.Sand markets could be uneconomical. This is because most of the demand in both markets are in the range below the crossing point. When demand is lower than the crossing point, the market in Kr.Sand supplies its own demand first before power is exported to the SE2 market. This makes the economical interconnection of the two markets less likely.

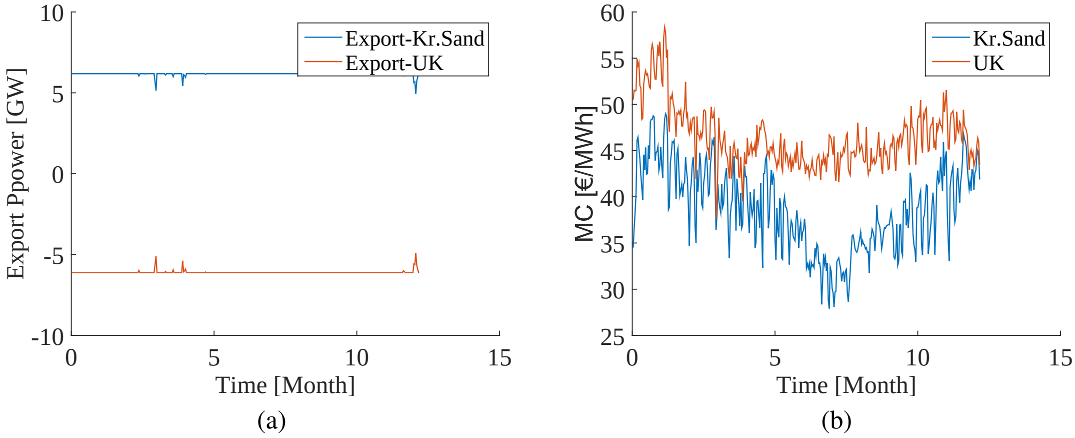

Figure 5.5: Power exchange between the Kr.Sand and UK markets (a) and MCs of the markets (b) for the optimum cable size between the markets

5.3.4 Optimum sizing of inter-connector using synthetic market data

As noted in the preceding section, if there is a clear difference in MCs between markets, it is straight forward to determine the need for an inter-connector to enhance the economic efficiency of the markets. However, the possible future scenario is that the markets are expected to operate at average marginal costs close to one another. And hence, the net exchange power between the interconnected markets are expected to be close to one another. This is reasonable because the future interconnected electricity markets are expected to have a significant share of renewable energy sources such wind, solar and wave energy over a wide area. The interconnection makes it possible for energy harvested in one are to be used in another area.

In all the upcoming sections in this chapter, different cases of electricity markets are investigated by using the synthesized data that could represent the future markets. Through out the investigations, the underlying assumption is that the average MCs and average power exchange between the markets are close to one another. In order to simulate these kind of cases, markets having the same or similar types of loads are considered in the investigations.

Figure 5.6 shows the MCs of two markets crossing each other at PX. Note from the figure that the demands in the two markets are the same. Note that in the upcoming investigation, markets having demands with different distribution are considered. The effect of the variations of the MCs in the markets is analysed by determining angle θ between the MCs, which is proportional to the difference between the slopes of the MCs of the markets. Suppose the $MC_1 = a_1 + b_1P_1$ and $MC_2 = a_2 + b_2P_2$; the angle θ can be defined as $\theta = tan^{-1}(b_1) - tan^{-1}(b_2)$. However, in most of the realistic cases investigated in this chapter, the values of b are less than 0.01. For a value of b less than 0.01, $tan^{-1}(b)$ is the same as b itself. Hence, in all of the following studies; θ is represented as $\theta = b_1 - b_2$. In addition, in all the upcoming investigation, the value of the crossing point, PX, is assumed to be the same as the average demand in the first market.

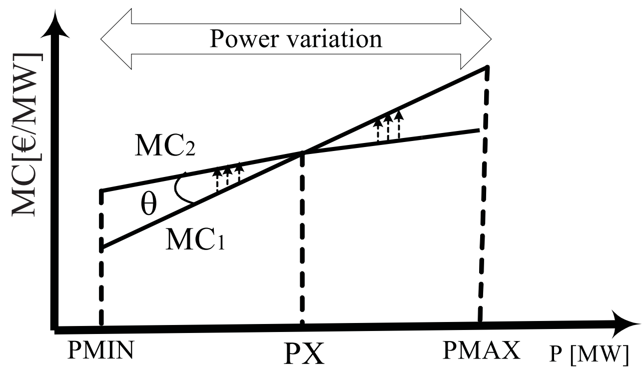

Figure 5.6: MCs of two electricity markets with the possibility of bi-directional power exchange

Note from Figure 5.6 that, when the total demand in the system is below the crossing point, PX; the first market (the market at terminal 1) exports power to market 2 since it is cheaper to produce electricity in market 1. Similarly, when the total demand in the system is greater than PX, market 2 exports power since it has lower marginal cost of generation. The same approach is used throughout the investigations made in the upcoming sections.

5.4 Optimum sizing of a two terminal system

In this section, optimum sizing of a two terminal system ,that can be used link two electricity markets, is investigated.

5.4.1 Design using daily average time series demand over a year

Figure 5.7 shows an HVDC transmission used to connect two fully competitive electricity markets. In this section, optimum sizing of the cable connecting the two markets as a function of the angle difference between the MCs and cable length are investigated. The

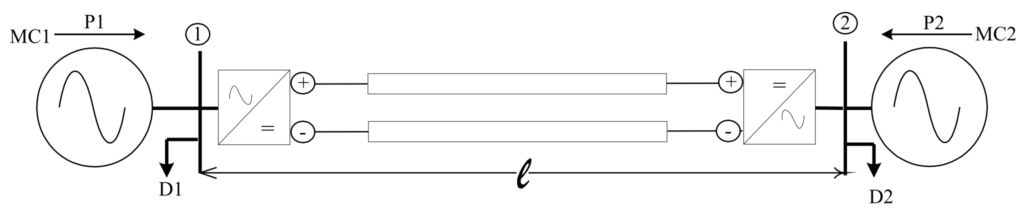

Figure 5.7: Bi-polar VSC HVDC transmission system used to connect two fully competitive electricity markets.

minimum angle difference between the markets that leads to a feasible solution is also analysed. The effect of the distribution or the variance of the time series demand is also analysed. Finally, the short comings of using the daily average time series demand in the model in achieving the future market condition is indicated.

Throughout this investigation, the same time series demands are considered in both markets. In addition, the crossing point, PX assumed to be the same as the average demand at terminal 1. Furthermore, the value of the marginal cost at PX is assumed to be 50 €/MWh, which is the average cost of electrical energy in Northern Europe [71].

Optimum cable rating as a function θ

In order to quantify the effect of angle θ on the selection of the optimum cable size, the distance between the markets in Figure 5.7 is assumed to be 600 km. In addition, both markets are assumed to have a demand type of NO in Figure 5.2a. The maximum demand in the markets is assumed to be 25 GW. Observe that, for the given maximum demand and demand distribution or profile type, the minimum and the average (hence PX) values can be calculated by using the data in Table 5.1. In this case, 11 GW and 16 GW are calculated as the minimum and average demand (PX) respectively.

For this system, the minimum value of θ is found to be close to 0.005. For this value of θ, the corresponding value of the optimum cable size is determined to be 505 MW. Similar analysis is made for the system with the same cable length and demand distribution and maximum demand of 20 GW and 15 GW.

Figure 5.8 shows the relation between the angle θ, system size and optimum cable ratings. Note from the results in the figure that as θ increases, so does the optimum cable size, which is obvious. Note also that, the change in θ has different effect depending on the size of the system. For a given change in θ, the corresponding change in cable size is bigger for a bigger system.

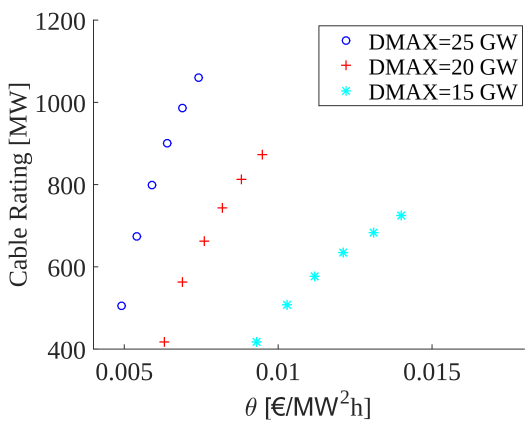

Figure 5.8: Optimum cable size as a function of the angle between MCs and maximum demand

Limiting values of the angle θ

Observe, from the results in Figure 5.8, that if the value of θ is reduced further from the smallest values in the figure; an optimum solution, with cable sizes having a thickness greater than 95 mm^2 (corresponds to 215 MW bipolar cable rating), ceases to exist. Note that this lower bound of cable thickness is based on the lower bound of cable thickness in the optimization model. Hence, in order to get a feasible optimum solution in any given case, there is a minimum angle requirement to be maintained, as shown in Figure 5.9.

Figure 5.9 shows the minimum possible value of θ and the corresponding minimum cable thickness as a function of cable length and DMAX (maximum demand). Figure 5.9(a) shows the minimum angle θ as a function of DMAX and cable length. The results in the figure shows that the minimum angle decays exponentially as DMAX increases. In addition, for a given DMAX, a higher value of minimum angle is required to yield a feasible optimum solution; which means that for a given scenario, there is no economic case the θ value of markets is less than θ_{min}. Figure 5.9(b) shows the optimum cable sizes that correspond to the minimum angle θ as a function of DMAX and cable length. The results in the figure show that the optimum cable size increases linearly with DMAX. For a given DMAX, higher cable rating is favoured for a longer cable, as can be seen from the figure.

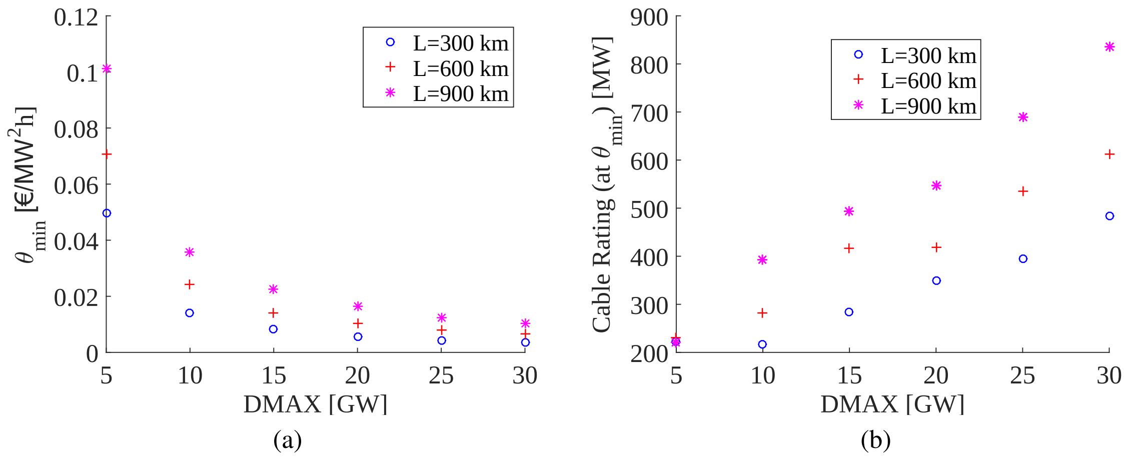

Figure 5.9: Minimum value of θ(a) and the corresponding value of optimum cable size (b) as a function of DMAX and cable length

Limitation of using daily average time series demand over a year

Recall that the design procedure discussed in this chapter is to be used in the optimum sizing of inter-connectors of the future electricity market where the net exchange power in the markets are expected to be closer to one another compared with today's scenario. In order to see if the desired objective is achieved by using the daily average data; it would be interesting to analyse the relevant simulation parameters resulting from the design procedure.

Figure 5.10 shows simulation results of key system parameters for one of the optimum system design shown in Figure 5.8 where DMAX=25 GW, $\theta = 0.0074$ and optimum cable rating is 1060 MW. Figure 5.10(a) shows system demand and generation during the whole year. Note that the demands at both terminals are the same, as described in the assumptions above. Note also that, during winter season, terminal 2 generates more since it is cheaper to generate at the terminal at high demand. During Spring and Summer, terminal 1 generates more since it is cheaper to generate at the terminal at low demand.

Furthermore, what is interesting to look at is the results in Figure 5.10(b) which show the power exchange between the two markets and the MCs at each markets. The power exchange in Figure 5.10(b) shows that the exchange flows from terminal 1 to 2 during the first three months since the demand at terminal 1 is higher than the crossing point (PX) during this time and the MC at terminal 2 is lower than that at 1 when the demand is higher than PX. And then from month 3 to 9 it flows from terminal 1 to 2 since the demand at terminal 1 is lower than PX and the MC at terminal 1 is lower than that at terminal 2. In general, the generator at terminal 1 can export power to terminal 2 as long as the total power it produces is less than PX and vice versa. Similar process continues between month 9 to 12, where the power flows from terminal 2 to 1. Note that the results in Figure 5.10 are

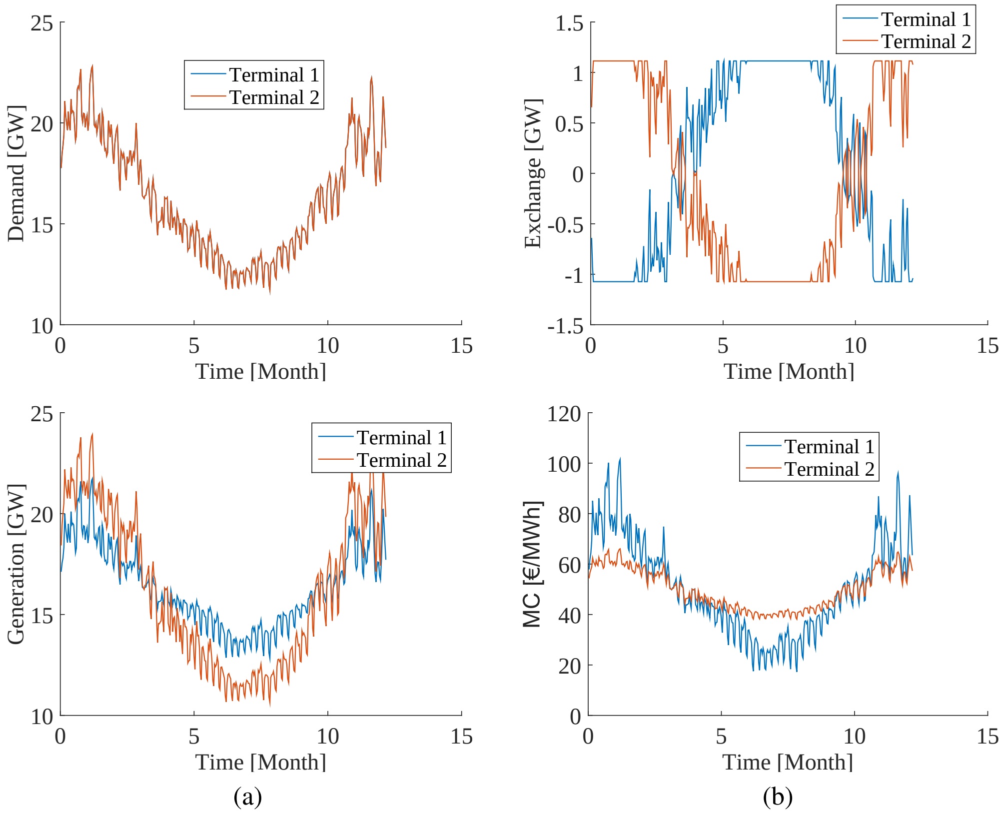

Figure 5.10: System demand and power generation over a year (a) Power exchange and system MCs over a year (b)

generated by using a time series demand over a year as an input to the model. The crossing point (PX) of the MCs is determined from the time series demand, which in this case is the average value of the demand at terminal 1. Note that with this crossing point and the input time series demand, only the seasonal variation of the load can be seen by the MCs and hence the results in the figure. So far, the design procedure has used long term time series demand to capture the seasonal variation of power exchange between the markets. The next step is to develop a procedure that can capture variations in the shorter term such as diurnal variation of exchange power, which thus will be the topic in the following subsection.

5.4.2 Design and operation with hourly average time series demand

In this section, a design procedure, that can capture the variation of electricity markets on hourly basis is presented. In the future interconnected systems, different markets connected to the grid are expected to operate with the marginal costs close to one another. This could open opportunities for intra-day, multi-directional power exchange. The design and analysis made in the following sections are based on the use of short term time series demand to make sure that the MCs can see the daily variation of demands in the systems.

Figure 5.11 shows hourly average normalized time series demand from different markets in the NordPool during 2015. All of the upcoming investigations use the time series demand data presented in this figure. Table 5.2 presents the main characteristics of the time series

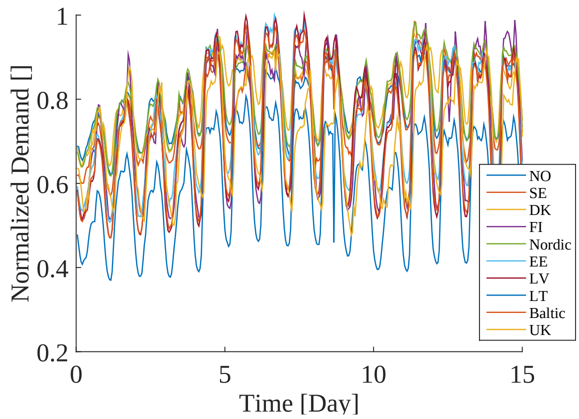

Figure 5.11: Hourly average normalized time series demand during the first 15 days of the year in 2015 in the NordSpot market, where NO, SE, DK, FI, EE, LV, LT and UK stands for Norway, Sweden, Denmark, Finland, Estonia, Latvia, Lithuania and United Kingdom respectively.

data. Note from the data in the table that LV has the largest variance compared with the rest.

Table 5.2: Main characteristics of the hourly average time series demand

	NO	SE	FI	DK	Nordic	EE	LV	LT	Baltic	UK
Var	0.006	0.009	0.007	0.020	0.008	0.018	0.023	0.016	0.021	0.014
Avg	0.796	0.781	0.818	0.740	0.815	0.761	0.739	0.591	0.732	0.712
Max	0.926	0.985	0.965	0.988	0.982	1.000	1.000	0.807	0.975	0.926
Min	0.620	0.573	0.639	0.515	0.618	0.508	0.471	0.370	0.471	0.477

In order to quantify optimum size of the a transmission cable as a function of angle θ; a 600 km cable length of the system in Figure 5.7 is considered. In addition, demand distribution type NO is used in the simulation where different values of DMAX (Maximum Demand) is considered.

Optimum cable size as a function of θ

Figure 5.12 shows optimum cable size as a function of the angle θ and different values of DMAX. The results in the figure show that optimum cable rating increases exponentially as θ increase, for the short term case as well. Similar to the results obtained using the long term time series data, the results in the figure also show that, for a given angle θ, thicker cables are favoured for system with higher DMAX.

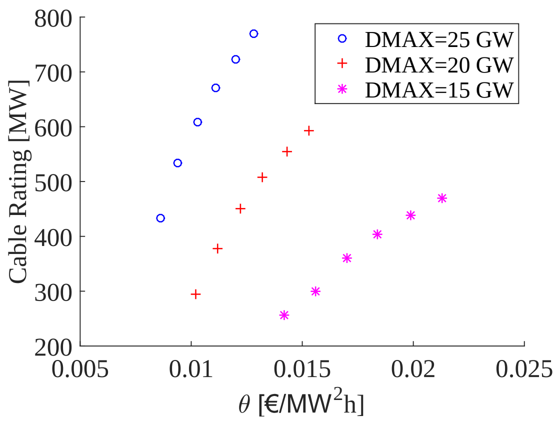

Figure 5.12: Optimum cable size as a function of the angle between MCs and maximum demand for short term time series demand

Simulation results of key system parameters

Consider the optimum cable size in Figure 5.12 for a system size of 25 GW and $\theta = 0.01$. The optimum cable size of the inter-connector for this system is about 600 MW. Figure 5.13 shows the simulation results of relevant parameters of the system. The results in Figure 5.13(a) show an hourly average time series demand (top) and power generation (bottom) in the system. As can be seen from the results in the figure, some times the generation at terminal 1 is higher than that at terminal 2 and vice versa depending on the MC and load level at each terminal. Note also that the value of PX (the crossing point of the MCs), which in this case is 16 GW, crosses the daily load variations almost every where; as can be seen from Figure 5.13(a).

Figure 5.13(b) shows the power exchange between the two terminals. As can be seen from the results, the desired exchange power flow of the future is achieved by using the short term modelling approach. Recall that the size of the optimum cable size is about 600 MW. The power exchange, presented in in Figure 5.13(b) (top), shows that power flow constraints are maintained. Figure 5.13(b) also shows the variation of the MCs as a function of the time series demand in the system. Observe that this coupled variation is MCs is the key for the frequent bidirectional power exchange.

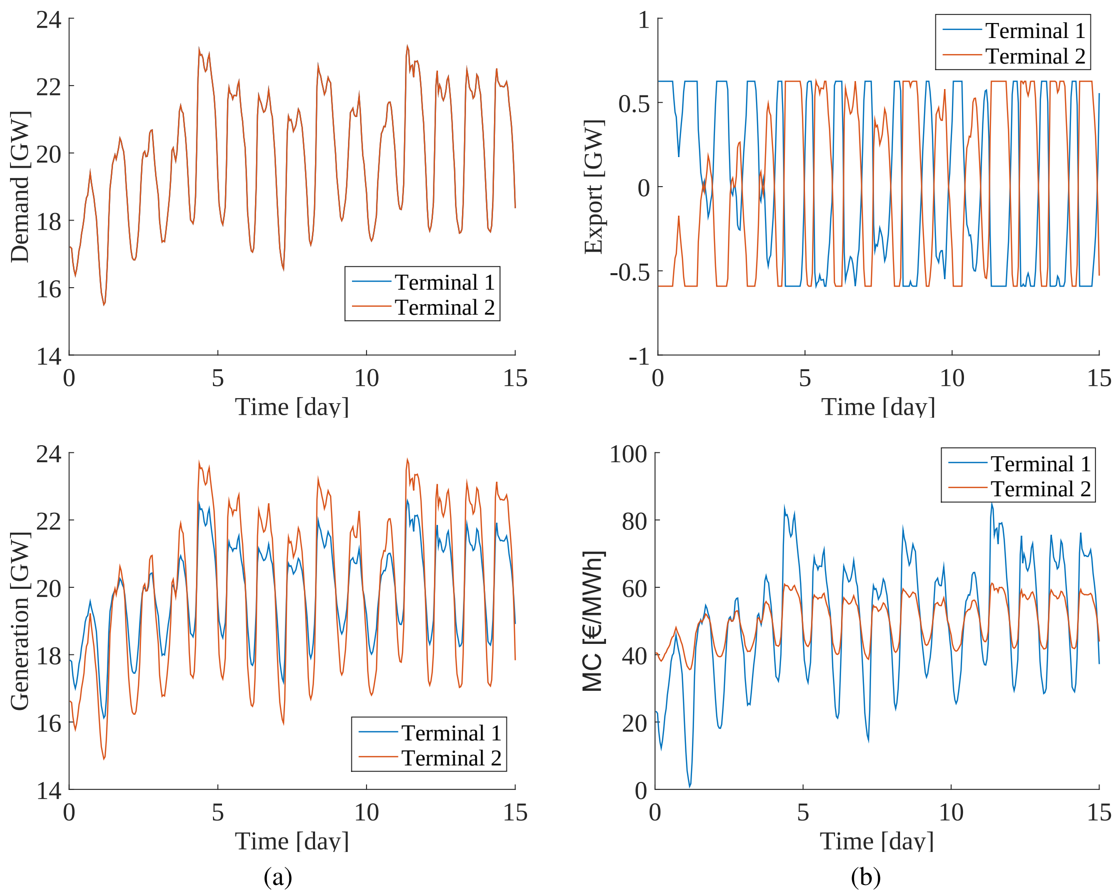

Figure 5.13: System demand and power generation 15 days (a) Power exchange and system MCs over 15 days (b)

Limiting value of θ as a function of system size and cable length

Observe from the results in Figure 5.12 that, as the size of the system increase; i.e. as the value of DMAX increases, the lowest value of θ, that results in a feasible solution, decreases. If the value θ in the figure is lowered further, one enters into a region of θ where there exist no feasible optimum solution. Hence, for every system size and type, there is a lowest value of θ below which there is no feasible optimum solution.

Figure 5.14 shows the minimum values of θ below which there is no optimum solution when the hourly average time series demand type of NO is used as an input in the optimization model. The figure presents θ_{min} as function of DMAX and cable length. The results in the figure show that θ_{min} decays exponentially as the size of the system increases. In addition, the results also show that for a given system size, higher value of θ_{min} is required for longer cables.

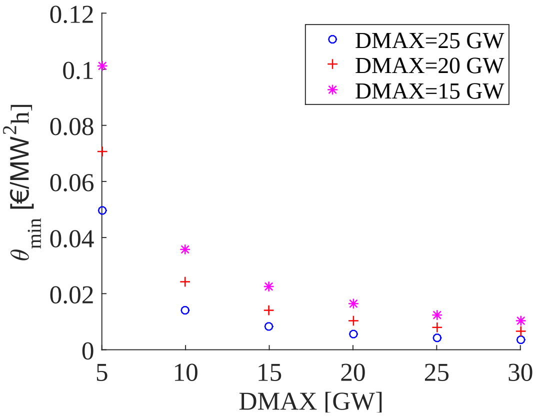

Figure 5.14: Minimum angle θ as a function of system size and cable length

Effect of time series demand distribution

Note that the results in Figure 5.12 and Figure 5.14 are simulated by using the time series demand type NO. As can be seen in Table 5.2, the demand profile type NO has the lowest variance compared with the other types. Figure 5.15 shows the effect of using different time series demand types on the required minimum angle θ. The results in the figure are

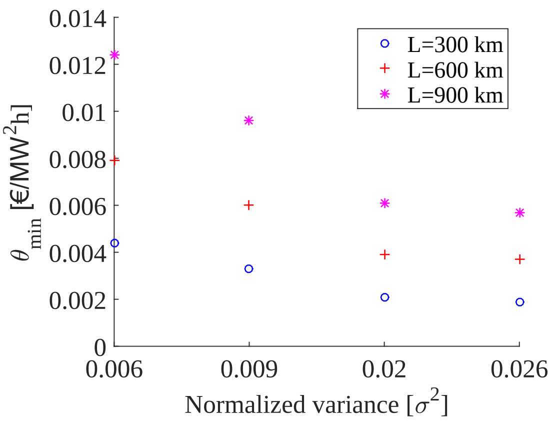

Figure 5.15: Effect of using different time series demand types having different variance values on minimum angle θ

simulated for a system size of $DMAX = 25GW$. As can be seen from the results in the figure, as the variance of the time series demand gets higher, the required minimum angle θ, gets lower.

Figure 5.16 shows optimum cable rating of systems with 25 GW and 30 GW capacities where time series demand profile type LV is used. As expected, according to Table 5.2, the LV profile has the highest variance in the list that lead to the thickest optimum cable possible that can be used in the upcoming investigations. Figure 5.16(a) shows optimum cable rating as a function of angle θ and cable length for the system size of 25 GW. Figure 5.16(b) shows optimum cable sizes as a function of angle θ and the cable size for the system size of 30 GW. As can be seen from the results in the figure, the minimum cable size increases with the cable length and system capacity.

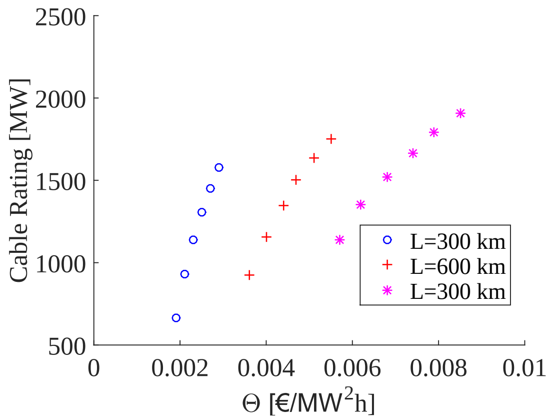

(a)

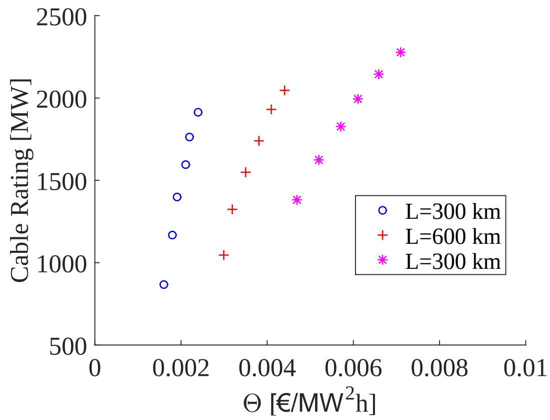

(b)

Figure 5.16: Optimum cable size as a function cable size and θ for for system capacities of (a) 25 GW and (b) 30 GW

Effect of the position of PX other than the average value

Observe also that in the simulations presented above, the crossing point (PX) is assumed to be at the average value of the demand at terminal 1. If PX is shifted to the left of the average value, terminal 1 is expected to import more power from terminal 2. Similarly, if PX is shifted to the right from the average, terminal 1 is expected to export more to terminal 1 since the MC at terminal 1 is lower than that at terminal 2 most of the time.

Effect of different system sizes at the terminals

Observe that the simulations made in the preceding sections assume that the average demands at both terminals are the same. In cases where the average demand at terminal 1 is higher than that at terminal 2, it is expected that the exchange power between the two terminals will decrease. This could lead to a scenario where it is no longer feasible to have a connector between the markets. If the average demand at terminal 2 is higher than that of terminal 1, it is not expected that the results obtained so far changes that much. This is because it is the generation at terminal 1 that determines export at lower demand and the higher the average demand at terminal 2 is, the higher the minimum demand becomes and there is a lower possibility of importing power from terminal 1. As the average demand at terminal 2 gets higher, it is less likely that the generation at terminal 1 exports more power to terminal 2.

5.5 Impact of WPP integration on electricity markets

In this section, the effect of integrating a WPP in to a competitive electricity market is investigated. Figure 5.17 shows a transmission link connecting a WPP to a main grid. If no curtailment of WPP power is considered, the size of the cable can be chosen to be the same as the capacity of the WPP. If the loss in the transmission line is ignored, the power

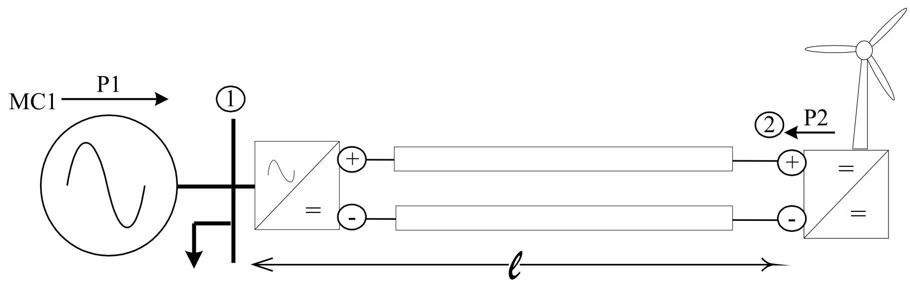

Figure 5.17: HVDC transmission system connecting a WPP to a competitive electricity markets

from the WPP, the demand at terminal 1 and the power generated at terminal 1 at any time t can be expressed as

$$P_{1,t} = D_{1,t} - P_{2,t} \tag{5.11}$$

where $P_{1,t}$ and $P_{2,t}$ are power generated at terminal 1 and power from the WPP at terminal 2 at a given time t respectively. The MC of the WPP is zero or a constant. Which means that the MC of the WPP does not depend on the amount of power produced. However, the MC at terminal 1 is a function of power generated at the terminal, which is expressed as $MC_1 = a_1 + b_1 P_1$. Hence, by using the relation in (5.11), the MC at terminal 1 at any time can be calculated as

$$MC_{1,t} = a_1 + b_1 P_{1,t} = a_1 + b_1 \left(D_{1,t} - P_{2,t}\right) \tag{5.12}$$

If one has a time series data from the WPP at terminal 2 and load and generation at terminal 1, the corresponding time series MC ($MC_{1,t}$ in this case) can be calculated. From the time series MC, an average MC can be calculated.

Figure 5.18 shows average MC in the Nordic and the UK electricity markets as a function of WPP capacity where hourly average time series data is used in the calculation. In each market, WPP capacities ranging from 0 GW up to the maximum demand in the respective markets are considered. According to the 2015 data from NordPool [72], the maximum demand in the Nordic and the UK markets are about 60 GW and 25 GW respectively. Hence, in the Nordic market, WPP capacities ranging from 0 GW to 60 GW is considered and in the UK market, WPP capacities ranging from 0 GW to 25 GW are considered. As expected, the average MCs in each market decreases as the WPP capacity increases. As can be seen from Figure 5.18(a) the MC in the Nordic market decreases by 0.3 €/MWh for every GW increases in WPP capacity. Similarly, Figure 5.18(b) shows that the MC in the UK market decrease by 0.6 €/MWh for every GW increases in WPP capacity.

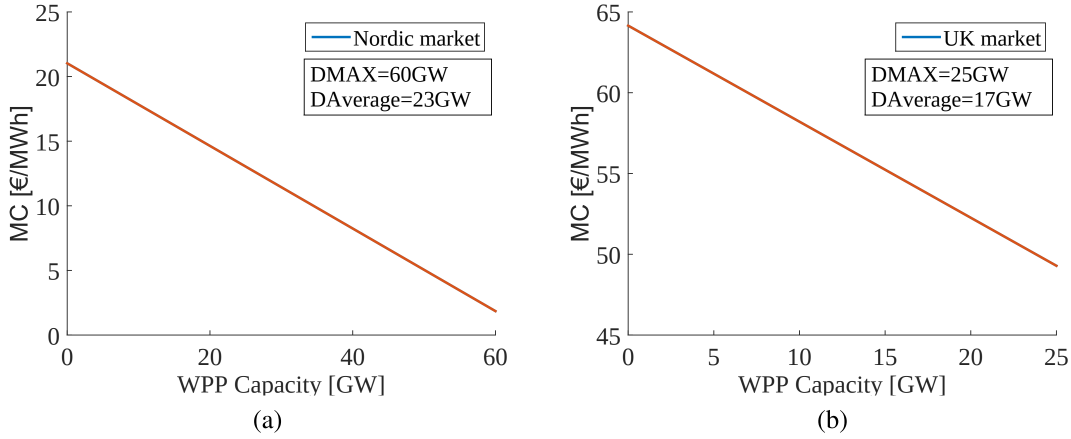

Figure 5.18: Marginal Cost of power generation at (a) terminal 1 (b) terminal 1 and 2

5.6 Integrating a WPP into a two terminal system

In this section, the effect of WPP integration into a system originally designed for power exchange is investigated. In addition, the need, if there is any, of system reinforcement due to the WPP integration is also analysed. Furthermore, the maximum capacity of a WPP that can be connected to this system, from an economical point of view, is investigated.

Figure 5.19 shows a WPP connected in between two markets. Before analysing the effect of WPP integration on the original system design and the markets using time series data; it is better to analytically relate relevant parameters for a single time to understand the results better. Assume that, at a given time, F amount of power flows from terminal 1 to terminal

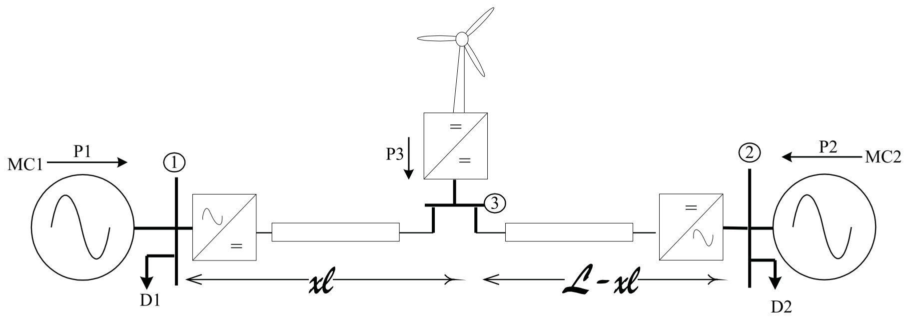

Figure 5.19: Integrating a WPP into a bi-polar VSC HVDC transmission system connecting electricity markets

2 since the MC at terminal 1 is lower than that at terminal 2. Hence, the power generated at terminal 2 is formulated as $P_2 = D_2 - F$ where D_2 is the demand at the terminal irrespective of the WPP power. This implies that $MC_2 = a_2 + b_2 P_2$ remains constant. When there is wind power at terminal 3, its optimal tendency is to go where the MC is the highest, i.e. terminal 2 in this case. If the power from the WPP is less than F, all of it goes to 2 and the remaining part of F comes from terminal 1. If the power from the WPP is equal to F, all goes to terminal 2 and terminal 1 does not contribute to F. If the power from the WPP is

greater than F, F amount goes to terminal 2 and the rest goes to terminal 1 to supply part or all of D_1 at terminal 1. To sum up, this can be expressed analytically as

$$\begin{aligned}
&P_2 = D_2 - F\\
&MC_2 = a_2 + b_2 P_2 = a_2 + b_2 (D_2 - F)\\
&P_{13} = F - P_3\\
&P_1 = D_1 + P_{13} = D_1 + F - P_3\\
&MC_1 = a_1 + b_1 P_1 = a_1 + b_1 (D_1 + F - P_3)
\end{aligned} \tag{5.13}$$

where P_{13} is the power flowing from terminal 1 to 3. Depending on the magnitude of the power from the WPP, it can be positive (where $P_3 < F$) or negative (when $P_3 > F$). Note that, for a given or fixed value F, P_2 and hence MC_2 remains constant irrespective of the variable power (P_3) from the WPP. This implies that the amount P_3 from the WPP displaces the generation from P_1 which reduces the MC at terminal 1. Similar result is expected for a longer term time series analysis except that the power flow F, wind power generation and demands in the system varies from time to time.

5.6.1 Simulation case set up

In order to simulate the effect of WPP integration on a system, initially designed to link two electricity markets, the following assumptions are made. Is assumed that, the markets at terminal 1 and 2 in Figure 5.19 have the same load with a maximum demand of 30 GW each and demand profile type of LV. The length of the cable connecting terminal 1 and 2 is 600 km. In addition, the difference in slopes of the MCs of the markets at the terminals is assumed to be $\theta = 0.0044$. Based on the assumptions, the optimum size of the cable is determined to be 2 GW. In addition, the capacity factor of the WPP is assumed to be 50% and a turbine tower height of 100 m is assumed. Figure 5.20 shows the time series demand (Figure 5.20(a)) and the MC data (Figure 5.20(b)) used in the simulation.

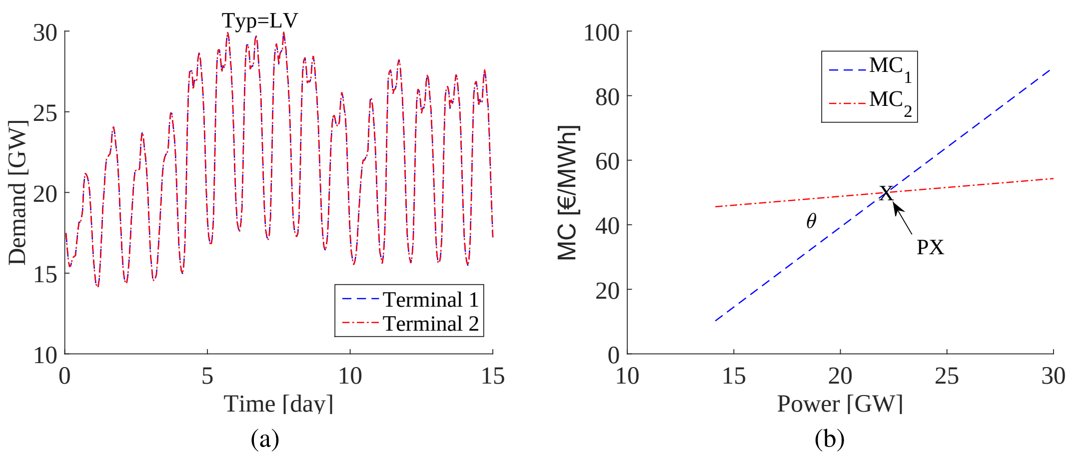

Figure 5.20: Time series demand of type LV (a) and MC data (b) assumed as input for the simulations

5.6.2 Effect of WPP integration on exchange power

Obviously, the integration WPP into the initial system, designed to link electricity markets, affects the patters of the initial power flow between the markets. Figure 5.21 shows the effect of different capacities of WPP integration on power export in each markets where the WPP is located 10 km from terminal 1 in this case. Note that positive values in the plots means that the terminal is exporting power, if negative, the terminal is importing. Figure 5.21(a) show the simulation results when the capacity of the WPP are 0 MW and 1000 MW. Note that, when the capacity of the WPP is 0 MW, the average export power at each terminal is close to zero. When the capacity of the WPP is 1000 MW, terminal 1 exports less and terminal 2 imports more since the MC of the WPP is zero. This is consistent with the analytical relations presented above.

Figure 5.21(b) shows the results when the capacity of the WPP is 3000MW and 4000MW. The results in the figure show that, when the WPP capacity is 3000 MW, terminal 1 also starts to import more. The exchange between terminal 1 and 2 gets less. When the capacity of the WPP is 4000MW, the cable is almost always used to transport power from the WPP to the loads in the different markets. As the capacity of the WPP gets more, the exchange power between the two terminals gets less.

5.6.3 Effect of WPP integration on SC

The change in pattern of the power flow, shown in Figure 5.21, has implications on the SC (SOcial Cost) of the system. Recall that, the SC, defined in (5.9), is a function of C^{gen}, C^{ploss} and C^{inv}. For a fixed network, where C^{inv} is a constant, the integration of the WPP affects C^{gen} and C^{loss}. The SC of the initial system, where WPP capacity is zero, is determined to be 122 M€; out of which 119 B€is the PV of cost of generation, 0.119 B€is the PV of cost of power loss and 2.64 B€is investment cost where an interest rate of 5% and life time of 30 years used to calculate the PV.

Figure 5.22 shows the percentage change in SC for different levels of WPP integration. The percentage change in SC calculated by subtracting the SC in the initial system from the SC at a given WPP capacity and length from terminal 1 and then dividing the difference by the initial SC. Note from the results in the figure that the integration of the WPP results in the reduction in the SC, which is a benefit to the society. The reduction in SC ranges from 5% to 15% depending on the level of WPP integration. Note also that, the reduction in SC is not sensitive to the location of the WPP.

5.6.4 Effect of WPP integration on MC

Obviously, the integration of WPP into the system affects the price of electricity in each market, as indicated in Figure 5.18. As more and more WPP is integrated into the system, the marginal cost of generation at each terminal decreases as the effective loads supplied by the generators in the markets decreases. Figure 5.23 shows the effect of different levels

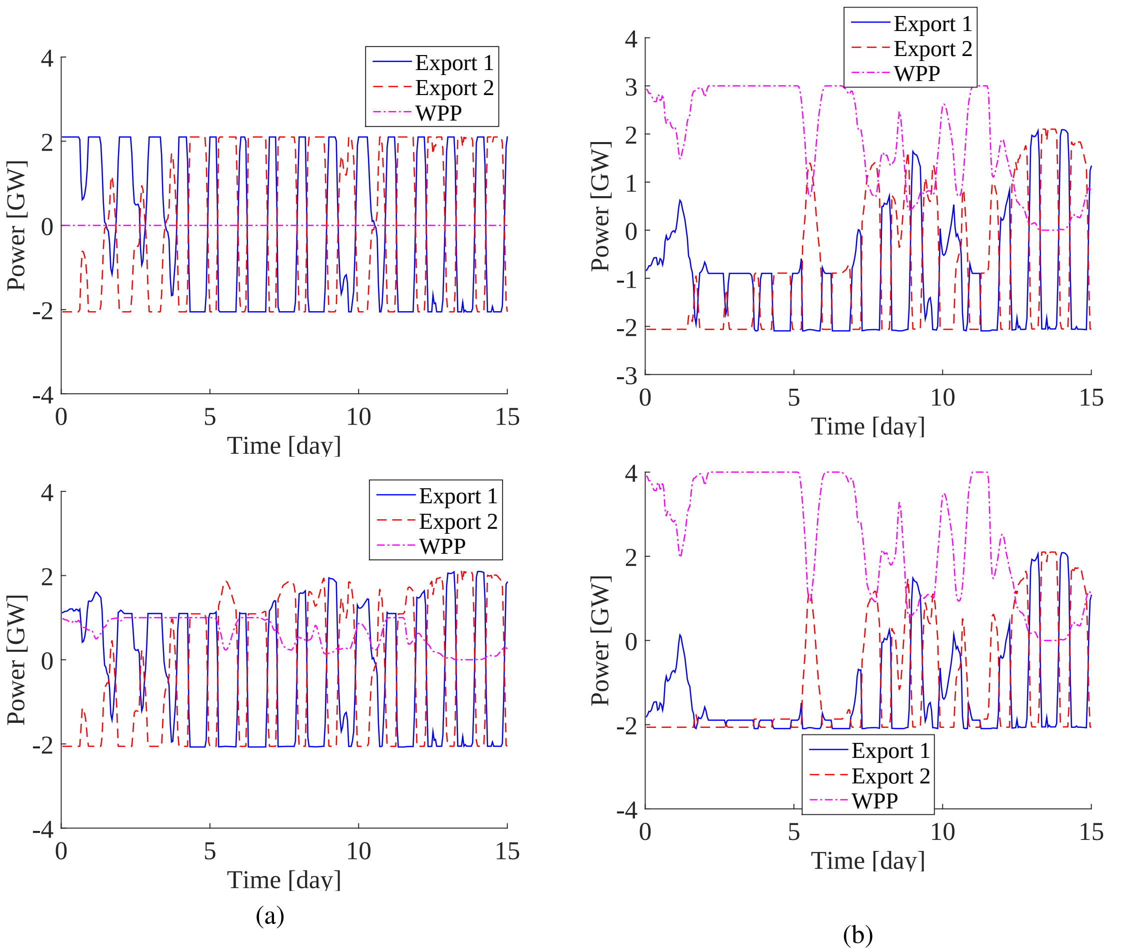

Figure 5.21: Effect of WPP integration on export power in the system for WPP capacity of (a) 0 GW and 1 GW (b) 3 GW and 4 GW when the slope difference, θ is 0.0044

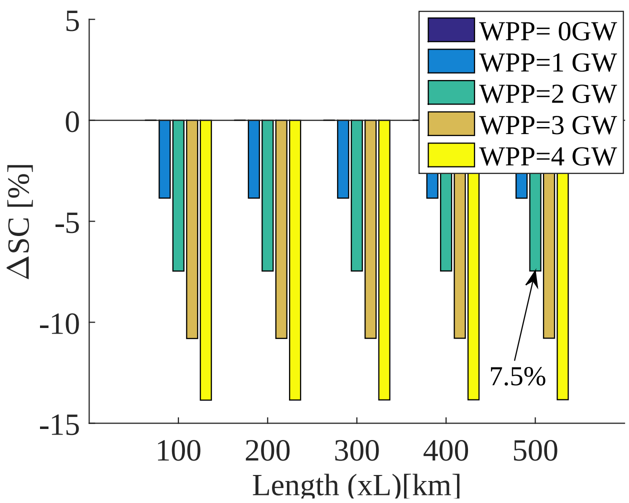

Figure 5.22: Effect of WPP integration on SC as a function WPP capacity and distance of the WPP from terminal 1.

of WPP integration on the MC in each market.

Figure 5.23(a) show the MCs in the markets when the WPP capacity is 0 GW. Note that as the WPP capacity increases, the difference between the MCs increases. Figure 5.23(b) shows the effect of 4 GW WPP on the MCs in the markets. Observe that, as the WPP

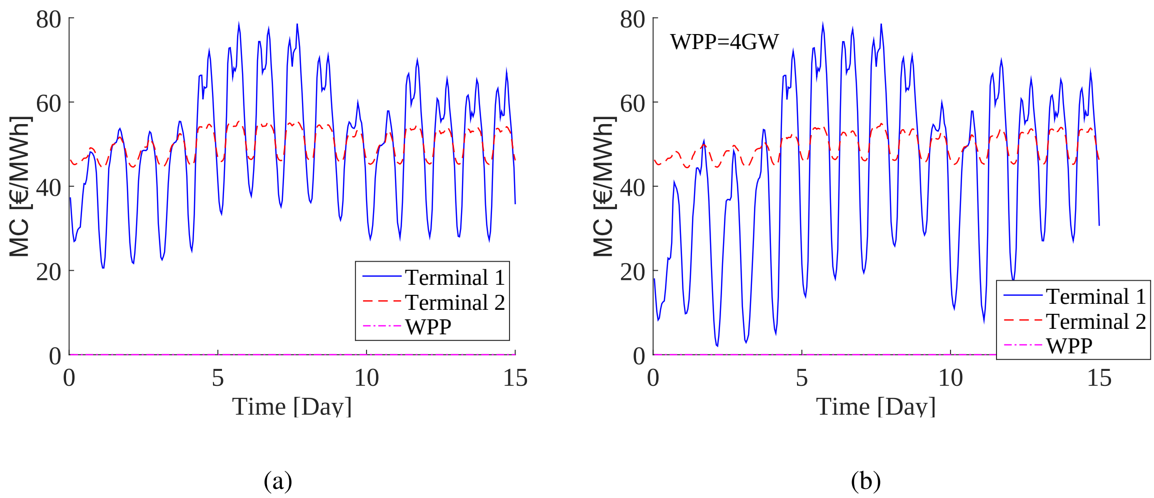

Figure 5.23: Effect of different levels of WPP integration on MCs of the markets (a) 0 GW WPP capacity (b) 4 GW WPP capacity.

capacity increases, the MC at terminal 1 gets closer to zero. If the WPP is increased further, it is possible that the MC at terminal 1 could become negative. This means that the WPP owner has to pay to supply loads at terminal 1, a scenario .which should be avoided. In order to avoid this scenario, one option could be to limit the level of WPP integration into the the system such that the minimum MC in the system is greater or equal to zero. This issue is further addressed Section (5.6.6).

5.6.5 Benefit of system reinforcement

It is expected that the integration of WPP affects the power flow in the system and hence efficiency of cable utilization in the system. Figure 5.24 shows the effect of different levels of WPP integration on system upgrade or reinforcement. The results in the figure are calculated by subtracting the optimum cable size the initial system where there is no WPP from the optimum cable size when different level of WPP is integrated into the system. Hence, a positive value in the figure indicate the indicated branch cable requires reinforcement by the amount shown. A negative value in the figure means that the branch cable is underutilized by the amount shown.

Figure 5.24(a) and Figure 5.24(b) show the optimum design of cables in branch $1- > 3$ and $2- > 3$, respectively, as a function of WPP capacity and length of the WPP from terminal 1, xl. Note from the results in Figure 5.24(a) that when the WPP is closer to terminal 1 it could be possible to reinforce the cable in branch $1 => 3$ with the indicated cable size.

However, as the WPP location becomes further away from the terminal 1, the utilization of the cable in the branch becomes less and less.

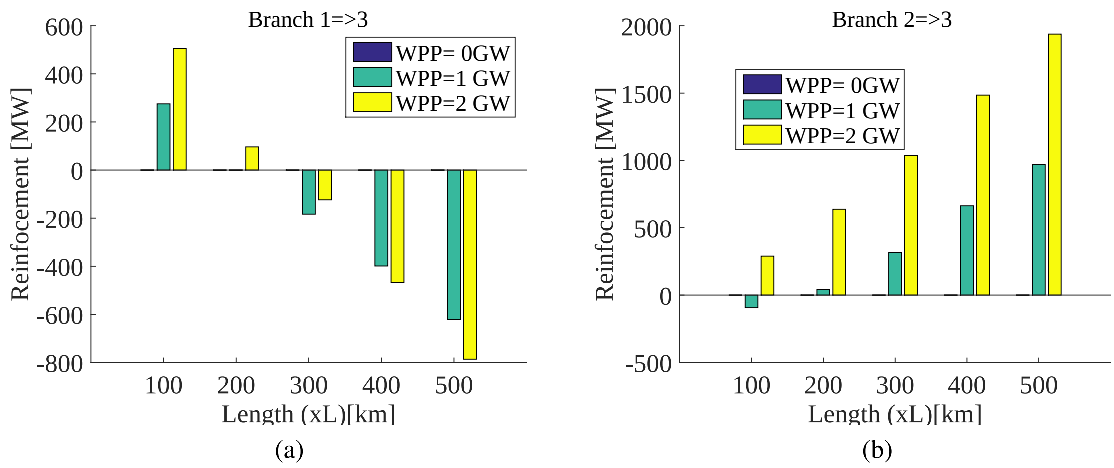

Figure 5.24: Effect WPP integration on branch cable utilization (a) branch $1->3$ (b) branch $2->3$

Figure 5.24(b) shows the needed reinforcement on branch cable $2 => 3$. As can be seen from the results in the figure, as the WPP location becomes closer to terminal 2, the need fot the requirement becomes much higher. As can be seen from the results in the figure, the utilization of the cable connecting the WPP to terminal 2 is slightly affected when the location of the WPP is farthest away from terminal 2.

Effect of reinforcement on SC

As shown in the results in Figure 5.24, depending on the location and level of WPP integration, the system need to reinforced accordingly to improve economic efficiency of the system. Through system reinforcement, both the transport of power the WPP and electricity trade over the transmission cable can be maintained. However, system reinforcement should not introduce an extra cost to the society. The benefit coming from the reinforcement has to be able to recover the cost of reinforcement during its life time. Figure 5.25 shows the effect of reinforcing cable in branch $2 => 3$ on the percentage change in SC. Note that the results in Figure 5.25 are calculated by subtracting the SC without reinforcement from the SC with reinforcement. As can be seen from the figure; apart from recovering the investment cost, a small reduction in SC can be achieved by reinforcing the system.

5.6.6 Limit of WPP capacity that can be integrated to the system

Recall that the MC at terminal 1 is formulated as $MC_1 = a_1 + b_1 P_1$. If the minimum allowed MC at this terminal is zero, the corresponding value of minimum power generation at this terminal can be formulated as $P_1^{MIN} = -a_1/b_1$. Recall also that for a given crossing

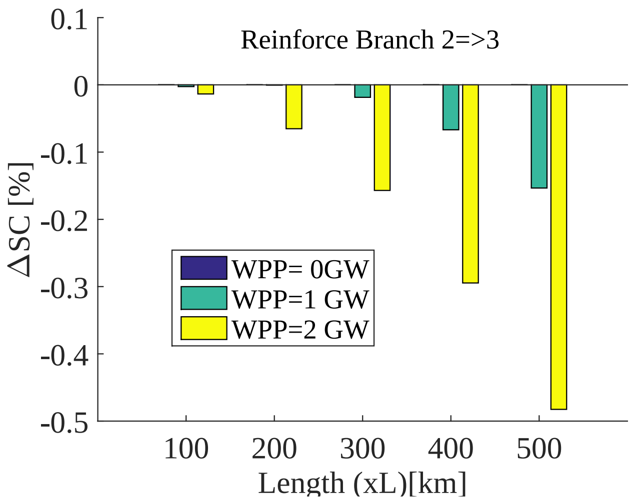

Figure 5.25: Effect of system reinforcement on the change in SC as a function of WPP capacity and length of the WPP from terminal 1.

point, PX, and the corresponding MC (MC_{PX}), a_1 can be formulated as $a_1 = MC_{PX} - b_1 PX$. From the two relations, the minimum generation at terminal 1 can be formulated as $P_1^{MIN} = -a_1/b_1 = -(MC_{PX} - b_1 PX)/b_1$. If the minimum demand at terminal 1 is D_1^{MIN}, the maximum amount of power that can be injected in to terminal 1 is $D_1^{MIN} - P_1^{MIN}$ where the difference should be greater than zero to avoid a negative MC at terminal 1. Assuming that the amount of power that can be injected into terminal 2 is equal to the rating of the cable, the maximum capacity of the WPP that can be integrated into this system to maintain the minimum MC at terminal 1 at zero can be formulated as

$$WPP^{MAX} = PbrR + D_1^{MIN} - P_1^{MIN} \tag{5.14}$$

where $PbrR$ is the rated power of the cable connecting the two markets. The relation in (5.14) indicates that the maximum WPP capacity that can be connected to the system and keep the MC at terminal 1 above zero depends on the market (related to the value of b_1) and the minimum demand at terminal 1. Figure 5.26 shows the relationship between maximum WPP capacity, electricity market and system size. Note from the results in the figure that for a given system capacity, the maximum WPP capacity that can be integrated into the system decreases as the value of b increases. Note also that for a given value of b, smaller systems can support more WPP capacity than larger systems. Observe that, in this case, the cable connecting the two markets has 2GW capacity and hence the maximum WPP is limited to 4GW.

5.7 Building a four terminal system from two terminal systems with WPP

In this section, an investigation of an economical interconnection of two subsystems, initially designed to transport power from WPPs to the main grids, is investigated. The main

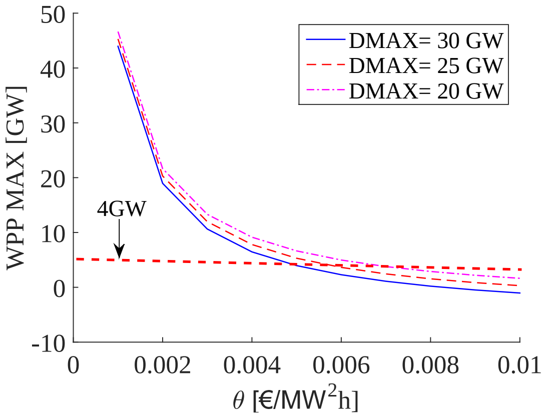

Figure 5.26: Relationship between maximum WPP capacity, electricity market and system size

objective in this investigation is to explore the possibilities using the initial systems, not only to transport WPP power, but also for electricity trading such that a better states of economic efficiency is achieved via the interconnection. Figure 5.27 shows the two subsystems intended to be interconnected through a cable with length l and between terminal 3 and 4.

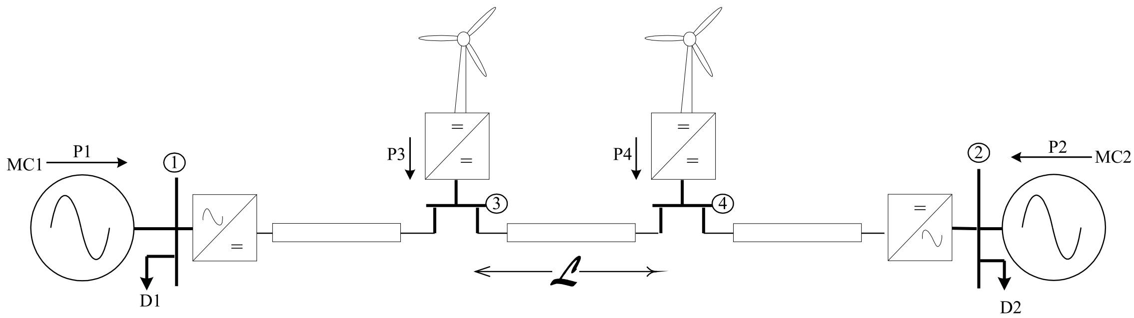

Figure 5.27: Building a four terminal VSC HVDC transmission system from two subsystems through a variable cable length l.

5.7.1 Simulation case set up

In order to make the simulation of the system in Figure 5.27, the lengths of the cables connecting terminal $1-3$ and $2-4$ are assumed to be fixed to 100 km. The WPPs are assumed to have a maximum capacity of 2000 MW and hence the rating of the cables connecting the WPPs to the main grid ($1-3$ and $2-4$) are assumed to be 2000 MW each. In addition, WPPs are are assumed to have capacity factor of 50$\%$ where the turbine heights in the WPPs are 100 m. Furthermore, it is assumed that the demand profiles at terminal 1 and 2 are of type LV and have maximum demand of 30 GW. Initially, the slope difference of the MCs of the two markets is assumed to be $\theta = 0.0052$.

Figure 5.28 shows the time series demand, time series WPP power and the MCs curves of the two market. Note from the plots in Figure 5.28(a) the time series demand is same at both terminals. Note also that the time series demand varies around the crossing point PX, as can be seen from Figure 5.28(b).

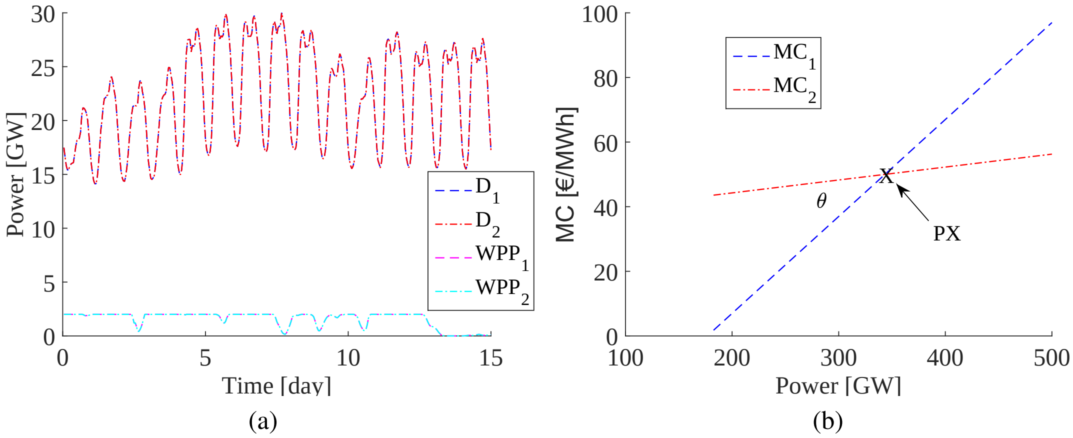

Figure 5.28: Time series demand of type LV (a) and MC data of the markets where initial slope difference $\theta = 0.0052$ (b) assumed for the simulation.

5.7.2 Optimum sizing of the inter-connector

For the assumed value of $\theta = 0.0052$ and other system parameter is, the optimum size of the inter-connector, having a length of 100 km, is 1212 MW. The optimum size of the inter-connector varies as the length of the inter-connector and the value of θ varies provided that the other parameters are constant. Figure 5.29 shows the variation of the optimum cable size as a function of the length of the inter-connector and θ. As can be seen from the results in the figure, the optimum size of the inter-connector decreases as the length increase, which is expected. In addition, the results in the figure show that for a given inter-connector length, the optimum cable size reduces for a reduced value of θ. Note from the results in the figure that it is not economical to interconnect the two subsystems when the θ is less than or equal to 0.0012.

Benefit of interconnection on cable utilization

Obviously, the inter-connector is expected to increase the utilization of the cables connecting terminal $1- > 3$ and $2 - 4$ since the cables in the interconnected system are used not only to transport power from the WPPs, but also for power exchange between the markets. Recall that, initially, the utilization of the cables, connecting the WPPs to terminal 1 and 2, were 60% each. Figure 5.30 shows the percentage change in the utilization of the cables after interconnection. Figure 5.30(a) shows the change in percentage utilization of the cable connecting terminal 1 and 3. As expected, the inter-connector resulted in an increased utilization up to 25%. Figure 5.30(b) shows the percentage increase in the utilization of the cable connecting terminals 2 and 4. In this case, the increase in utilization is even higher,

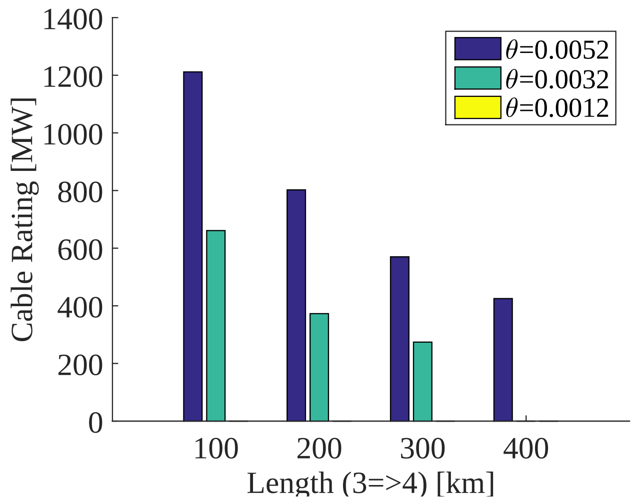

Figure 5.29: Optimum size of the inter-connector connecting terminal 3 and 4 as a function of its length and different values of θ

where the highest is close to 30%. This is mainly because of the fact that the marginal cost of generation at terminal 2 is higher at lower demand and hence a lot of power from the wind goes to this terminal which increases the utilization factor.

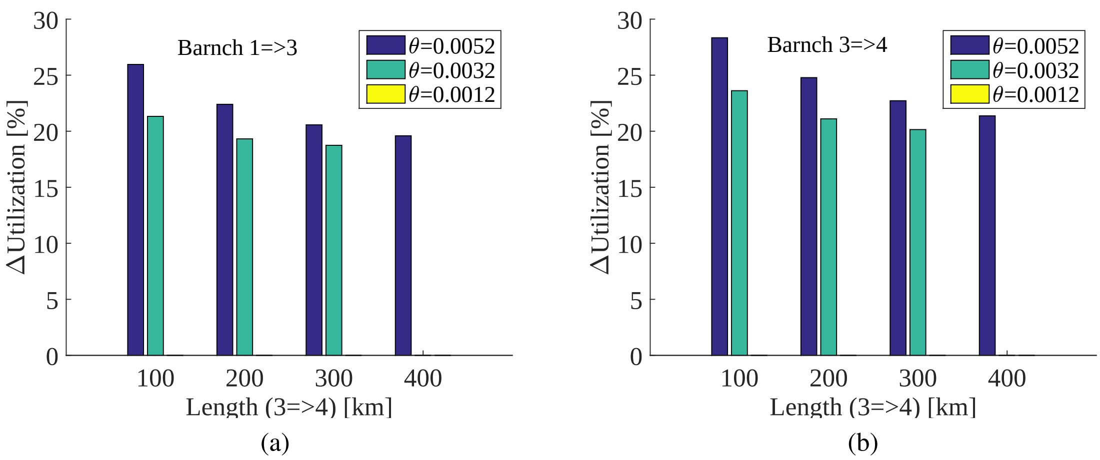

Figure 5.30: Change in the percentage utilization of branch (a) $1->3$ and (b) $2->4$ as a function θ and inter-connector length

Figure 5.31 shows the system demand and generation when the optimum size of the inter-connector at a length of 100 km is used. Figure 5.31(a) shows the system demand and Figure 5.31(b) the generation in the system. As can be seen from the results in the figure, when demand is high terminal 2 exports power since the genration at the terminal is higher than its load. Similarly, when low and/or WPP output is low, terminal 1 exports power.

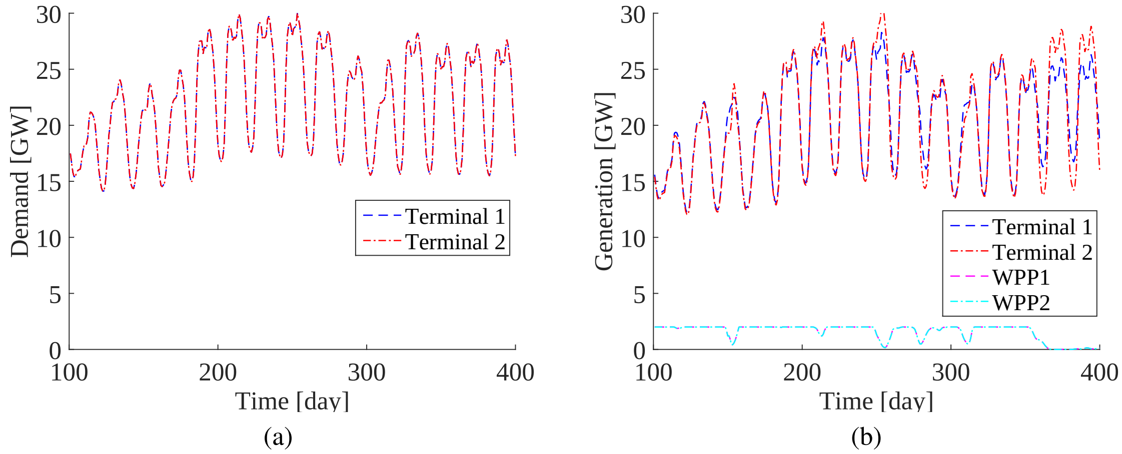

Figure 5.31: Demand (a) and generation (b) in the system for the optimum inter-connector at 100km

5.8 Chapter summary

In this chapter, optimum sizing VSC HVDC transmission system expansion has been investigated. Based on the investigated cases, it is verified that the economically optimum interconnection of two electricity markets depends on the slope difference of the MCs of the markets, which is represented as angle θ. Furthermore, it is determined that θ decays exponentially as the system size increases. In addition, the minimum angle requirement, θ_{min}, for economical interconnection of different markets is established. For example, for two markets with $DMAX$=20 GW each; θ_{min} for a cable length of 300 km is determined to be 0.006. For a 100% increase in cable length; θ_{min} increases 100%. It is also determined that a 100% increase in the variance of the time series demand reduces θ_{min} by 50%.

Furthermore, the integration of a WPP to a system initially built for electricity trade is investigated. Based on the investigation, it determined that the integration can reduce the SC (Social Cost) by about 5% to 15% depending on the WPP capacity and its location with respect to the markets. It is also verified that reinforcing the integrated system can enhance the economic efficiency of the system depending on WPP capacity and its location with respect to the markets.

In addition, the interconnection of two subsystems, which are initially built to transport power from WPPs to the main grids, studied. The results from the study show that the economically optimum interconnection can increase the utilization of the system by about 20% to 30%.

Chapter 6

Conclusions and future work

6.1 Conclusions

In this thesis, the modelling and analysis of a stepwise building of VSC HVDC transmission systems, are presented. Based on the investigated cases, it is verified that the optimum size of a VSC HVDC transmission cable, used to connect two electricity markets with a pre-defined exchange power, is approximately equal to the absolute mean of the exchange power.

Based on the investigated cases using pre-defined exchange data, it is found that the LRMC of a VSC HVDC transmission system is independent of system size and profile type used. For a 300 km cable length, the LRMC is determined to be 3 €/MWh and increases by 2 €/MWh for every 300 km increase in cable length. In addition, it is verified that for an investment in a given optimum design to be profitable, the SRMC should be higher than the LRMC for a given cable length.

When a unit transmission fee of α=20 €/MWh is used for a system with a normalized absolute mean of 0.56, the SRMC is determined to be 10 €/MWh, irrespective of the length of the transmission cable. For the stated absolute mean value, it is shown that it is always profitable to invest on the designs with cable lengths from 300 km to 900 km; and maximum exchange ranging from 1 GW to 3 GW. From an investment point of view, the same designs can yield profits ranging from 50$\%$ to 250$\%$ of the investment cost depending on the length of cable in the specified range. It is also shown that the higher the SRMC, the higher the profit to the investor. Based on the studied cases, it is quantified that every 1$\%$ decrease in the unit transmission tariff, α, leads to a 3$\%$ loss in the investor's profit.

Moreover, based on the investigation made on a system with a normalized mean absolute value of 0.25 or less, it is concluded that it is not profitable to invest in the designs with cable lengths greater than 600 km.

Furthermore, from the investigation made on the integration of a WPP into a system, initially designed for exchange; it is conclude that the closer the WPP is to the area that often imports power, the more the reduction in system power loss. It is also shown that placing the WPP closer to the area that often export power, results in increased power loss in the system.

Based on the cases studied using the market model, it is verified that the economically optimum interconnection of two electricity markets depends on an the angle θ where θ is the angle formed between the MC curves of the market at the crossing point. Furthermore, it is determined that the minimum required θ decays exponentially as the system size increases. In addition, the minimum angle requirement, θ_{min}, for economical interconnection of different markets is established. For example, for two markets with $DMAX$=20 GW each; θ_{min} for a cable length of 300 km is determined to be 0.006. For a 100$\%$ increase in cable length; θ_{min} increases 100$\%$. It is also determined that a 100$\%$ increase in the variance of the time series demand reduces θ_{min} by 50$\%$.

Furthermore, by using the modified ARMA based modelling procedure, it is quantified that ARMA(6,0) and ARMA(0,6) can be used to model the HF and LF components of the wind speed time series respectively, provided that the required transformations are made on the given time series data where necessary. Similarly, by using the modified VARMA based modelling procedure, it is also quantified that a six order vector AR model structure (VAR(6)) can be used to model spatially and temporally correlated wind speed time series in the North Sea and the Baltic Sea region.

6.2 Future Work

In this thesis, only a limited level of system complexity is considered in the investigations of the stepwise building of an HVDC grid. The investigation of similar studies with more system complexity could be considered in future work. Furthermore, the full potential of spatial and temporal correlation of wind power modelling is not fully utilized in the investigation of system studies, which could be considered in future studies.

In addition, reliability and contingency analysis are not considered in this study. Hence, it would be interesting to see how the optimum results are affected when reliability is considered in the optimization model.

In addition, it is of great importance to study the step wise expansion of the meshed HVDC grid from control and protection point view. Establishing a grid code requirement for connection and operation of the meshed HVDC grid is an interesting topics to be considered in future works.

References

[1] E. Roadmap, "2050: a practical guide to a prosperous, low carbon europe," *Communication from the Commission to the European Parliament, the Council, the European Economic and Social Committee and the Committee of the Regions, Brussels*, 2011.

[2] L. Stankeviciute and P. Criqui, "Energy and climate policies to 2020: the impacts of the european 20/20/20 approach," *International Journal of Energy Sector Management*, vol. 2, no. 2, pp. 252–273, Jun. 2008.

[3] A. Ho, A. Mbistrova, G. Corbetta, I. Pineda, and K. Ruby, "The european offshore wind industry-key trends and statistics 2015," *Report. Brussels: European Wind Energy Association*, 2015.

[4] E. W. E. Association, *Pure Power - wind energy targets for 2020 and 2030*. EWEA, 2011.

[5] J. De Decker, P. Kreutzkamp, S. Cowdroy, L. Warland, J. Völker, J. Tambke *et al.*, "Offshore electricity grid infrastructure in europe," *OffshoreGrid Final Report*, 2011.

[6] I. M. de AlegrÃa, J. L. MartÃn, I. Kortabarria, J. Andreu, and P. I. Ereno, "Transmission alternatives for offshore electrical power," *Renewable and Sustainable Energy Reviews*, vol. 13, no. 5, pp. 1027–1038, Jun. 2009.

[7] A. Woyte, J. De Decker, and V. Van Thong, *A North Sea Electricity Grid [r] evolution: Electricity Output of Interconnected Offshore Wind Power: a Vision of Offshore Wind Power Integration*. Greenpeace, 2008.

[8] H. Holttinen, P. Meibom, A. Orths, B. Lange, M. O'Malley, J. O. Tande, A. Estanqueiro, E. Gomez, L. Söder, G. Strbac, J. C. Smith, and F. van Hulle, "Impacts of large amounts of wind power on design and operation of power systems, results of IEA collaboration," *Wind Energy*, vol. 14, no. 2, pp. 179–192, Mar. 2011.

[9] E. W. E. Association *et al.*, *Large Scale Integration of Wind Energy in the European Power Supply: Analysis, Issues and Recommendations: a Report*. European Wind Energy Association, 2005.

[10] S. Gordon, "Supergrid to the rescue," *Power Engineer*, vol. 20, no. 5, pp. 30–33, Oct. 2006.

[11] N. S. C. G. Initiative, "Final report-grid configuration," NSCOGI, Tech-

nical Report, November 2012.[Online]. Availabl e: http://www. benelux. int/NSCOGI/NSCOGI_WG1_OffshoreGridReport. p df, Tech. Rep., 2012.

[12] J. Blau, “Europe plans a north sea grid,” *IEEE Spectrum*, vol. 47, no. 3, pp. 12–13, Mar. 2010.

[13] T. Vrana, R. Torres-Olguin, B. Liu, and T. Haileselassie, “The north sea super grid - a technical perspective,” in *9th IET International Conference on AC and DC Power Transmission, 2010. ACDC*, Oct. 2010, pp. 1–5.

[14] N. Kirby, M. J. Luckett, L. Xu, and W. Siepmann, “HVDC transmission for large offshore windfarms,” in *AC-DC Power Transmission, 2001. Seventh International Conference on (Conf. Publ. No. 485)*, Nov. 2001, pp. 162–168.

[15] B. Van Eeckhout, D. Van Hertem, M. Reza, K. Srivastava, and R. Belmans, “Economic comparison of VSC HVDC and HVAC as transmission system for a 300 MW offshore wind farm,” *European Transactions on Electrical Power*, vol. 20, no. 5, pp. 661–671, Jul. 2010.

[16] ENTSO-E, “Offshore transmission technology report - entso-e,” Tech. Rep., Nov. 2011.

[17] P. Haugland, “It is time to connect: Technical description of hvdc light® technology,” *ABB Techincal Report*, 2008.

[18] “BorWin1 | References | ABB.” [Online]. Available: http://new.abb.com/systems/hvdc/references/borwin1

[19] E. W. E. Association *et al.*, “Oceans of opportunity,” *Harnessing Europes largest domestic energy resource. European Wind Energy Association*, 2009.

[20] C. B.-. W. Group *et al.*, “Hvdc grid feasibility study,” Melbourne: International Council on Large Electric Systems, Tech. Rep., 2011.

[21] V. Akhmatov, M. Callavik, C. Franck, S. Rye, T. Ahndorf, M. Bucher, H. Müller, F. Schettler, and R. Wiget, “Technical guidelines and prestandardization work for first hvdc grids,” *IEEE Transactions on Power Delivery*, vol. 29, no. 1, pp. 327–335, 2014.

[22] A. A. van der Meer, R. T. Pinto, M. Gibescu, P. Bauer, J. T. Pierik, F. D. Nieuwenhout, R. L. Hendriks, W. L. Kling, and G. A. van Kuik, “Offshore transnational grids in europe: the north sea transnational grid research project in relation to other research initiatives,” in *Proceedings of 9th International Workshop on Large-Scale Integration of Wind Power*, 2010, pp. 1–8.

[23] T. K. Vrana and O. B. Fosso, “Technical aspects of the north sea super grid,” *CIGRE Electra, November*, 2011.

[24] D. Van Hertem and M. Ghandhari, “Multi-terminal VSC HVDC for the european supergrid: Obstacles,” *Renewable and Sustainable Energy Reviews*, vol. 14, no. 9, pp. 3156–3163, Dec. 2010.

[25] K. Rudion, A. Orths, P. Eriksen, and Z. Styczynski, "Toward a benchmark test system for the offshore grid in the north sea," in *2010 IEEE Power and Energy Society General Meeting*, Jul. 2010, pp. 1–8.

[26] S. Henry, A. Denis, and P. Panciatici, "Feasibility study of off-shore HVDC grids," in *2010 IEEE Power and Energy Society General Meeting*, Jul. 2010, pp. 1–5.

[27] C. Stijn, "Steady-state and dynamic modelling of vsc hvdc systems for power system simulation," Ph.D. dissertation, PhD dissertation, Katholieke University Leuven, Belgium, 2010.

[28] R. Teixeira Pinto and J. A. Ferreira, "Multi-terminal DC networks: System integration, dynamics and control," Ph.D. dissertation, CPI Koninklijke WÃ¶hrmann, Mar. 2014.

[29] T. M. Haileselassie, "Control, dynamics and operation of multi-terminal VSC-HVDC transmission systems," dissertation, Norwegian University of Science and Technology, 2012.

[30] W. Long and S. Nilsson, "HVDC transmission: yesterday and today," *IEEE Power and Energy Magazine*, vol. 5, no. 2, pp. 22–31, Mar. 2007.

[31] N. Flourentzou, V. Agelidis, and G. Demetriades, "VSC-Based HVDC power transmission systems: An overview," *IEEE Transactions on Power Electronics*, vol. 24, no. 3, pp. 592–602, Mar. 2009.

[32] J.-E. Skog, K. Koreman, B. Pääjärvi, T. Worzyk, and T. Andersröd, "The norned hvdc cable link–a power transmission highway between norway and the netherlands," *Proceedings of Energex 2006*, 2006.

[33] C. Veal, "European offshore supergrid proposal: Vision and executive summary," Airtricity, Tech. Rep, Tech. Rep., 2006.

[34] P. Kundur, N. J. Balu, and M. G. Lauby, *Power system stability and control*. McGraw-hill New York, 1994, vol. 7.

[35] J. DESCLOUX, P. RAULT, S. NGUEFEU, J.-B. CURIS, X. GUILLAUD, F. COLAS, and B. RAISON, "HVDC meshed grid: Control and protection of a multi-terminal HVDC system," in *CIGRE 2012*, France, 2012.

[36] J. Beerten, D. Van Hertem, and R. Belmans, "VSC MTDC systems with a distributed DC voltage control - a power flow approach," in *PowerTech, 2011 IEEE Trondheim*, Jun. 2011, pp. 1–6.

[37] A. LAbbate and G. Migliavacca, "Review of costs of transmission infrastructures, including cross border connections," *REALISEGRID Deliverable D*, vol. 3, 2011.

[38] G. Stamatiou, K. Srivastava, M. Reza, and P. Zanchetta, "Economics of dc wind collection grid as affected by cost of key components," *Volume 15 Wind Energy Applications*, p. 4177, 2011.

[39] S. Lundberg, “Performance comparison of wind park configurations,” Chalmers University of Technology, Tech. Rep., 2003.

[40] A. L Abbate and G. Migliavacca, “Review of costs of transmission infrastructures, including cross border connections,” *REALISEGRID Deliverable D*, vol. 3.

[41] R. Billinton, H. Chen, and R. Ghajar, “Time-series models for reliability evaluation of power systems including wind energy,” *Microelectronics Reliability*, vol. 36, no. 9, pp. 1253–1261, Sep. 1996.

[42] R. Billinton and W. Wangdee, “Reliability-based transmission reinforcement planning associated with large-scale wind farms,” *IEEE Transactions on Power Systems*, vol. 22, no. 1, pp. 34–41, 2007.

[43] P. Chen, T. Pedersen, B. Bak-Jensen, and Z. Chen, “ARIMA-Based time series model of stochastic wind power generation,” *IEEE Transactions on Power Systems*, vol. 25, no. 2, pp. 667–676, 2010.

[44] J. McLean and G. Hassan, “Wp2. 6 equivalent wind power curves,” *TradeWind Deliverable*, vol. 2, pp. 1–14, 2008.

[45] A. Shamshad, M. A. Bawadi, W. M. A. Wan Hussin, T. A. Majid, and S. A. M. Sanusi, “First and second order markov chain models for synthetic generation of wind speed time series,” *Energy*, vol. 30, no. 5, pp. 693–708, Apr. 2005.

[46] F. Castro Sayas and R. Allan, “Generation availability assessment of wind farms,” *Generation, Transmission and Distribution, IEE Proceedings-*, vol. 143, no. 5, pp. 507–518, Sep. 1996.

[47] N. B. Negra, O. HolmstrÃ¸m, B. Bak-Jensen, and P. SÃ¸rensen, “Model of a synthetic wind speed time series generator,” *Wind Energy*, vol. 11, no. 2, pp. 193–209, Mar. 2008.

[48] B. G. Brown, R. W. Katz, and A. H. Murphy, “Time series models to simulate and forecast wind speed and wind power,” *Journal of Climate and Applied Meteorology*, vol. 23, pp. 1184–1195, Aug. 1984.

[49] W. Wangdee and R. Billinton, “Considering load-carrying capability and wind speed correlation of WECS in generation adequacy assessment,” *IEEE Transactions on Energy Conversion*, vol. 21, no. 3, pp. 734–741, Sep. 2006.

[50] S. Soman, H. Zareipour, O. Malik, and P. Mandal, “A review of wind power and wind speed forecasting methods with different time horizons,” in *North American Power Symposium (NAPS), 2010*, Sep. 2010, pp. 1–8.

[51] M. Lei, L. Shiyan, J. Chuanwen, L. Hongling, and Z. Yan, “A review on the forecasting of wind speed and generated power,” *Renewable and Sustainable Energy Reviews*, vol. 13, no. 4, pp. 915–920, May 2009.

[52] I. Colak, S. Sagiroglu, and M. Yesilbudak, “Data mining and wind power prediction: A literature review,” *Renewable Energy*, vol. 46, pp. 241–247, Oct. 2012.

[53] G. E. P. Box, G. M. Jenkins, and G. C. Reinsel, *Time Series Analysis: Forecasting and Control*. John Wiley & Sons, May 2013.

[54] A. Chuang, "Time series analysis: Univariate and multivariate methods," *Technometrics*, vol. 33, no. 1, pp. 108–109, Feb. 1991.

[55] K. Yunus, "Steady state analysis of hvdc grid in the north sea with offshore wind power plants," 2014.

[56] K. Yunus, T. Thiringer, and P. Chen, "Arima-based frequency-decomposed modeling of wind speed time series," *IEEE Transactions on Power Systems*, vol. 31, no. 4, pp. 2546–2556, 2016.

[57] I. Van der Hoven, "POWER SPECTRUM OF HORIZONTAL WIND SPEED IN THE FREQUENCY RANGE FROM 0.0007 TO 900 CYCLES PER HOUR," *Journal of Meteorology*, vol. 14, no. 2, pp. 160–164, Apr. 1957.

[58] W. G. Ruesink, "Introduction to sampling theory," in *Sampling Methods in Soybean Entomology*, ser. Springer Series in Experimental Entomology, M. Kogan and D. C. Herzog, Eds. Springer New York, Jan. 1980, pp. 61–78.

[59] L. Fawcett and D. Walshaw, "Markov chain models for extreme wind speeds," *Environmetrics*, vol. 17, no. 8, pp. 795–809, Dec. 2006.

[60] C. Gavriluta, S. Spataru, I. Mosincat, C. Citro, I. Candela, and P. Rodriguez, "Complete methodology on generating realistic wind speed profiles based on measurements," in *International Conference on Renewable Energies and Power Quality*, 2012, pp. 828–829.

[61] winddata.com. [Online]. Available: www.winddata.com

[62] D. D. Le, G. Gross, and A. Berizzi, "Probabilistic modeling of multisite wind farm production for scenario-based applications," *Sustainable Energy, IEEE Transactions on*, vol. 6, no. 3, pp. 748–758, 2015.

[63] K. Yunus, P. Chen, and T. Thiringer, "Modelling spatially and temporally correlated wind speed time series over a large geographical area using varma," *IET Renewable Power Generation*, 2016.

[64] "4c Offshore Overview - 4c Offshore." [Online]. Available: http://www.4coffshore.com/

[65] "The European Wind Energy Associationl EWEA." [Online]. Available: http://www.ewea.org//

[66] NASA, "NASA (National aeronautics and space administration)," http://disc.sci.gsfc.nasa.gov/daac-bin/FTPSubset.pl, 2015.

[67] "Wind profile power law." [Online]. Available: https://en.wikipedia.org/

[68] D. S. Kirschen and G. Strbac, *Fundamentals of power system economics*. John Wiley

& Sons, 2004.

[69] K. Bhattacharya, M. Bollen, and J. E. Daalder, *Operation of restructured power systems*. Springer Science & Business Media, 2012.

[70] T. A.Le, *Power market management*, Chalmers University of Technology.

[71] EUROPEAN COMMISSION, "Energy prices and costs report," Brussels, Tech. Rep. SWD(2014) 20 final/2, Mar. 2014.

[72] N. P. Spot, "Elspot prices," *Website, December*, 2015.

[73] ENTSO-E, "ENTSO-E overview of transmission tariffs in europe: Synthesis 2011," Tech. Rep., Jun. 2012.

Appendix A

The Per Unit System

In power system analysis, it is usually easier to use per unit system to normalize system variables. Compared to the use of physical units (amperes, volts, ohms, henry, etc...), the per unit system offers computational simplicity by eliminating units and expressing system quantities as a dimensionless rations. A well chosen per unit system can minimize computational effort, simplify evaluation, and facilitate understanding of system quantities [34].

The per unit system is defined as

$$\text{quantity is per unit} = \frac{\text{actual quantity}}{\text{base value of the quantity}} \tag{A.1}$$

An important aspect of the per unit system is the base value of the quantity. Some base quantities may be chosen independently, while others follow the fundamental relationship between the system variables. Normally, the base values are often chosen so that the principal variables will be equal to one per unit under rated condition. If base voltage (U_{base}) and base power (S_{base}) are chosen, the other system quantities such as base current, base impedance are determined as

$$I_{base} = \frac{S_{base}}{U_{base}} \tag{A.2}$$

$$Z_{base} = \frac{U_{base}^2}{S_{base}} \tag{A.3}$$

Once the base quantities are determined, the corresponding per unit quantities can be calculated using (A.1).

Appendix B

DC power flow equation and Newton-Raphson method

B.1 DC power flow equation

A power flow model of an HVDC grid can be developed by using the same procedure as that for AC [34], [27]. In a study presented in [28], a DC power flow equation is developed but the procedure followed was less clear compare with the conventional procedures. In this section a step by step generic AC power flow equation is derived from which a DC power flow equation can be determined.

Consider Figure B.1 which shows a single line diagram of a power system. The buses in the system are numbered from 1 to 4, where each bus is connected to shunt element(s) and to one or more buses with transmission line(s). All branches are denoted with their admittance values y_ij for a branch connecting bus i to bus j and y_i for a shunt element at bus i. Current injection at a bus i is denoted by I_i. A current injection can be either positive (into the bus) or negative (out of the bus).

Kirchoff's Current Law (KCL) states that current injection at a bus is equal to the sum of the currents flowing out of the bus. Combining this with Ohms law ($I = U/z = Vy$), the current injected into bus 1 can be written as

$$I_1 = (U_1 - U_2)y_{12} + (U_1 - U_3)y_{13} + (U_1 - U_4)y_{14} + U_1y_1 \tag{B.1}$$

Note that the current contribution of the term containing y_{14} is zero since y_{14} is zero (no connection between bus 1 and 4). Re-arranging (B.1), the current injected at bus 1 can be expressed as

$$I_1 = U_1(y_1 + y_{12} + y_{13} + y_{14}) + U_2(- y_{12}) + U_3(- y_{13}) + U_4(- y_{14}) \tag{B.2}$$

The current injections at bus 2, 3 and 4 can be represented in a similar way. The equation

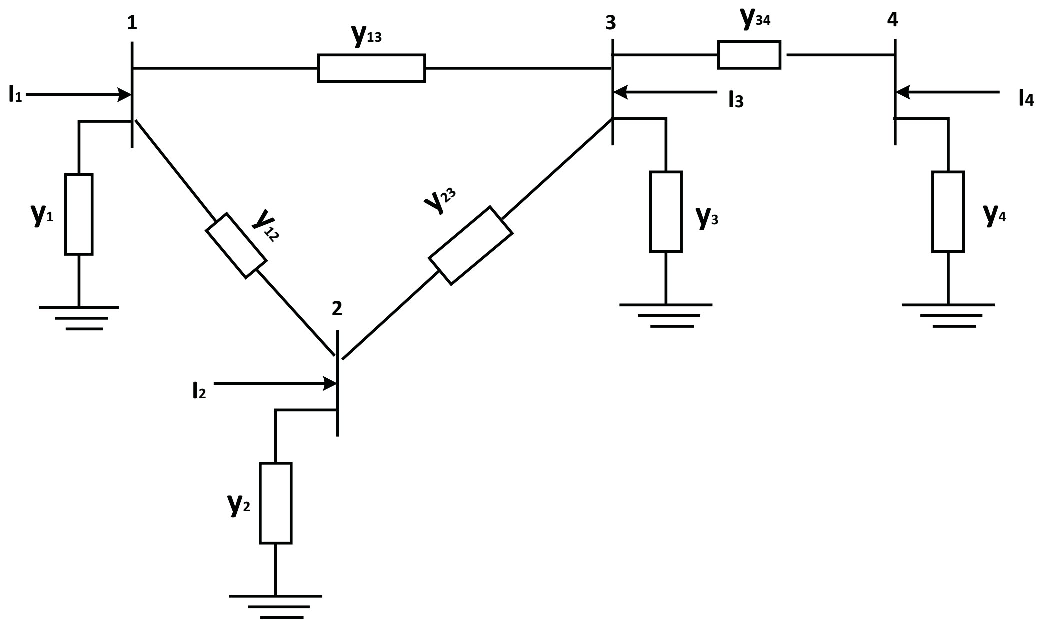

Figure B.1: Typical power system topology

containing all the nodal quantities is expressed as

$$\begin{bmatrix} I_1 \\ I_2 \\ I_3 \\ I_4 \end{bmatrix} = \begin{bmatrix} y_1 + y_{12} + y_{13} + y_{14} & -y_{12} & -y_{13} & -y_{14} \\ -y_{21} & y_2 + y_{21} + y_{23} + y_{24} & -y_{23} & -y_{24} \\ -y_{31} & -y_{32} & y_3 + y_{31} + y_{32} + y_{34} & -y_{34} \\ -y_{41} & -y_{42} & -y_{43} & y_4 + y_{41} + y_{42} + y_{43} \end{bmatrix} \cdots$$
$$\cdots \begin{bmatrix} U_1 \\ U_2 \\ U_3 \\ U_4 \end{bmatrix} \tag{B.3}$$

Note that the admittance from bus i to bus j is the same as the admittance from bus j to bus i. The matrix containing the network admittances in (B.3) is called the admittance matrix, also known as the Y-bus matrix, and is denoted as

$$[Y] = \begin{bmatrix} Y_{11} & Y_{12} & Y_{13} & Y_{14} \\ Y_{21} & Y_{22} & Y_{23} & Y_{24} \\ Y_{31} & Y_{32} & Y_{33} & Y_{34} \\ Y_{41} & Y_{42} & Y_{43} & Y_{44} \end{bmatrix} \tag{B.4}$$

where Y_{ij} is an element of the admittance matrix in row i and column j, as can be seen in (B.3).

Combining (B.3) and (B.4),(B.3) can be re-written as

$$\begin{bmatrix} I_1 \\ I_2 \\ I_3 \\ I_4 \end{bmatrix} = \begin{bmatrix} Y_{11} & Y_{12} & Y_{13} & Y_{14} \\ Y_{21} & Y_{22} & Y_{23} & Y_{24} \\ Y_{31} & Y_{32} & Y_{33} & Y_{34} \\ Y_{41} & Y_{42} & Y_{43} & Y_{44} \end{bmatrix} \begin{bmatrix} U_1 \\ U_2 \\ U_3 \\ U_4 \end{bmatrix} \tag{B.5}$$

Equation (B.5) can be applied to a system with any number of buses. The general relationship between the nodal quantities (voltage and current in this case) for any system with 'n' number of buses can be written as

$$\begin{bmatrix} I_1 \\ I_2 \\ . \\ . \\ . \\ I_n \end{bmatrix} = \begin{bmatrix} Y_{11} & Y_{12} & . & . & . & Y_{1n} \\ Y_{21} & Y_{22} & . & . & . & Y_{2n} \\ . & . & . & . & . & . \\ . & . & . & . & . & . \\ . & . & . & . & . & . \\ Y_{n1} & Y_{n2} & . & . & . & Y_{nn} \end{bmatrix} \begin{bmatrix} U_1 \\ U_2 \\ . \\ . \\ . \\ U_n \end{bmatrix} \Rightarrow \ [I] = \ [Y]\ [U] \tag{B.6}$$

An important property of the admittance matrix is that it is symmetrical along the diagonal elements (i.e.; Y_{ij}=Y_{ji}); the diagonal element Y_{ii} is obtained as the sum of the admittances of all the branches connected to bus i, including the shunt element (i.e,; $Y_{ii} = y_i + \sum\limits_{k=1,k\neq i}^{N} y_{ik}$); the off-diagonal elements are the negative sum of the admittances connecting bus i and j (i.e.; $Y_{ij} = -y_{ij}$).

In power flow problems, usually the power injected at the buses are given instead of the injected current. Hence, the fundamental apparent power (S_k) injected at bus k can be expressed as

$$S_k = P_k + jQ_k = U_k I_k^* \tag{B.7}$$

where U_k and I_k are the nodal voltage and current at bus k respectively, S_k is the apparent power and P_k, Q_k active and fundamental reactive power respectively.

From (B.6), the current injected at bus k can be calculated as

$$I_k = \sum_{j=1}^{N} Y_{kj} V_j \tag{B.8}$$

where N is the total number of buses in the system.

Combining (B.7) and (B.8), the power injected at a bus k can be calculated as

$$S_k = U_k \left(\sum_{j=1}^{N} Y_{kj} U_j \right)^* = U_k \sum_{j=1}^{N} Y_{kj}^* U_j^* \tag{B.9}$$

where S_k, P_k, Q_k are the fundamental apparent, active and fundamental reactive power injected at bus k; U_k is the voltage at bus k and Y_{kj} is the admittance of the line from bus k to bus j.

Observe that in the DC side of the system, the voltage at a bus U_k is a DC quantity, hence $U_k = |U_k| \angle 0 = |U_k|$. The admittance Y_{kj} is generally a complex quantity, and is defined in terms of the conductance G_{kj} and susceptance B_{kj} as a real and imaginary parts of the admittance matrix element Y_{kj}, respectively, so that $Y_{kj} = G_{kj} + jB_{kj}$. However, in a steady state DC system, the impact of on the susceptance B_{kj} can be neglected and hence the fundamental reactive power is zero. Hence, a model of DC power flow equation consists of only active power which can be formulated as

$$P_k = \sum_{j=1}^{N} |U_k| \, |U_j| \, G_{kj} \tag{B.10}$$

B.2 Newton-Raphson method

Consider a function $f(U) = P$, where U is the unknown variable and let $U^{[0]}$ be the initial estimate of the roots of the function f(U) and $\Delta U^{[0]}$ be a small deviation from the actual solution. The function f(U) around the estimated root can be written as $f(U^{[0]} + \Delta U^{[0]}) = P$. This function can be expressed using the Taylor-serious expansion as

$$f(U^{[0]} + \Delta U^{[0]}) = f(U^{[0]}) + \left(\frac{df}{dU}\right) \Delta U^{[0]} + \frac{1}{2!} \left(\frac{d^2 f}{dU^2}\right) \left(\Delta U^{[0]}\right)^2 ... = P \tag{B.11}$$

For a small value of the deviation in the root, $\Delta U^{[0]}$, (B.11) can approximated as

$$\begin{aligned} & f(U^{[0]} + \Delta U^{[0]}) \approx f(U^{[0]}) + \left(\frac{df}{dU}\right) \Delta U^{[0]} = P \\ & \Rightarrow P - f(U^{[0]}) = \Delta P^{[0]} = \left(\frac{df}{dU}\right) \Delta U^{[0]} \end{aligned} \tag{B.12}$$

The deviation $\Delta U^{[0]}$ can be calculated from (B.12) and it is used to update the new approximation of the solution as

$$U^{[1]} = U^{[0]} + \Delta U^{[0]} \tag{B.13}$$

The second and third approximation can be iterated and calculated in a similar way. Hence, (B.13) can be generalized to calculate the n^{th} approximation of the variable as

$$U^{[n+1]} = U^{[n]} + \Delta U^{[n]} \tag{B.14}$$

This iteration continues until convergence condition is met, namely $\Delta U^{[n]} < \varepsilon$, where ε is the error in the solution which can be tolerated.

Equation (B.14) is used to solve a non-linear equation with one variable. A similar procedure can be used to solve non-linear equations involving a number of variables. The deviation of the variables in the system of non-linear equations involving N variables is calculated as

$$\begin{bmatrix} \Delta U_1 \\ \Delta U_2 \\ . \\ . \\ . \\ \Delta U_N \end{bmatrix}^{[n]} = \begin{bmatrix} \frac{\partial f_1}{\partial U_1} & \frac{\partial f_1}{\partial U_2} & . & . & . & \frac{\partial f_1}{\partial U_N} \\ \frac{\partial f_2}{\partial U_1} & \frac{\partial f_2}{\partial U_2} & . & . & . & \frac{\partial f_2}{\partial U_N} \\ . & . & . & . & . & . \\ . & . & . & . & . & . \\ . & . & . & . & . & . \\ \frac{\partial f_N}{\partial U_1} & \frac{\partial f_N}{\partial U_2} & . & . & . & \frac{\partial f_N}{\partial U_N} \end{bmatrix}^{-1} \begin{bmatrix} \Delta P_1 \\ \Delta P_2 \\ . \\ . \\ . \\ \Delta P_N \end{bmatrix}^{[n]} \Rightarrow [\Delta U]^{[n]} = [J]^{-1} [\Delta P]^{[n]} \tag{B.15}$$

where $\Delta U^{[n]}$ is the deviation in the solution of the variable U at the n^{nth} iteration, J is the Jacobian matrix which is a function of the partial derivatives of the function f and $\Delta P^{[n]}$ which is defined as

$$[\Delta P]^{[n]} = [P]^{[n]} - \left[f(U^{[n]})\right] \tag{B.16}$$

Using the deviation in the variable, $\Delta U^{[n]}$, the solution of the variable U can be updated using the relation

$$[U]^{[n+1]} = [U]^{[n]} + [\Delta U]^{[n]} \tag{B.17}$$